

OPTIMAL OBSERVATION SELECTION IN MAGNETIC RESONANCE SPECTROSCOPIC  
IMAGING

Yun Gao

Certificate of Approval:

---

Thomas S. Denney, Jr.  
Associate Professor  
Electrical and Computer Engineering

---

Stanley J. Reeves, Chair  
Associate Professor  
Electrical and Computer Engineering

---

Jitendra K. Tugnait  
Professor  
Electrical and Computer Engineering

---

Amnon J. Meir  
Associate Professor  
Mathematics Department

---

John F. Pritchett  
Dean  
Graduate School

OPTIMAL OBSERVATION SELECTION IN MAGNETIC RESONANCE SPECTROSCOPIC  
IMAGING

Yun Gao

A Dissertation  
Submitted to  
the Graduate Faculty of  
Auburn University  
in Partial Fulfillment of the  
Requirements for the  
Degree of  
Doctor of Philosophy

Auburn, Alabama

August 14, 2000

## VITA

Yun Gao, daughter of Xin Gao and Shuhua Song, was born in Henan province, P. R. China on December 2, 1965. She received her Bachelor degree and Master degree in Powering Engineering from Wuhan University of Hydraulic and Electric Engineering in July, 1985, and July, 1988, respectively. She worked in China Institute of Water Resources and Hydropower Research from July 1988 to August 1996. She entered the Ph.D. program in the Department of Electrical and Computer Engineering in September 1996. Her research interests are in the areas of digital signal/image processing, medical imaging, optimal acquisition/image compression, image reconstruction, and multiband digital signal reception.

DISSERTATION ABSTRACT

OPTIMAL OBSERVATION SELECTION IN MAGNETIC RESONANCE SPECTROSCOPIC  
IMAGING

Yun Gao

Doctor of Philosophy, August 14, 2000

(M.S., Wuhan University of Hydrolic and Electric Engineering, P. R. China, July 1988)

(B.S., Wuhan University of Hydrolic and Electric Engineering, P. R. China, July 1985)

133 Typed Pages

Directed by Stanley J. Reeves

Magnetic resonance spectroscopic imaging (MRSI) is a completely non-invasive method for obtaining quantitative information regarding biochemical parameters [1]. It shows great promise for use in basic physiological research and for clinical imaging of metabolic function [2, 3]. The information obtained with MRSI can be used to assess regional metabolic abnormalities in various pathologies. However, MRSI requires a great deal of time to gather the data necessary to achieve satisfactory resolution. When prior information about the image is available, it may be possible to reconstruct the image from a subset of k-space samples. Therefore, we desire to choose the best possible combination of a small number of k-space samples to guarantee the quality of the reconstructed image by using the available prior knowledge. In this thesis, we assume prior knowledge only of the region of support (ROS) of the spatial-domain image.

Sequential forward selection (SFS) is appealing as an optimization method because the previously selected sample can be observed while the next sample is selected. We develop an efficient computational strategy for this algorithm that allows SFS to be

applied to this problem when the image region has a known region of support (ROS). The combined algorithm efficiently selects a reduced set of k-space samples from which the ROS can be reconstructed with minimal noise amplification. Furthermore, if there is no noise, the minimum density can be reached with this algorithm.

Hexagonal sampling gives a 13.4% sampling density reduction compared to rectangular sampling for images with a circular ROS. However, nonuniform sampling patterns are more efficient than hexagonal sampling for the same ROS. To reduce selection time and achieve higher resolution, we develop a sequential backward selection (SBS) algorithm from samples on a hexagonal grid. Simulation results show that more efficiency and reduced selection time can be achieved with the proposed method in comparison with SBS on a rectangular grid.

We develop two efficient algorithms for optimizing the dithering pattern so that an image can be reconstructed as reliably as possible from a periodic nonuniform set of samples, which can be obtained from a dithered rectangular-grid array.

One algorithm is SBS of sample arrays. Taking into account the ROS of the image, we sequentially eliminate the least informative array recursively until the minimal number of arrays remain. In this scheme, we provide an efficient update formula for the criterion based on convolution kernels rather than large, non-sparse matrices, an efficient update formula for the convolution kernels based on the deleted array, and an efficient reconstruction method based on convolutions. The proposed method dramatically reduces storage and computational complexity.

The other algorithm is SFS of sample arrays. Based on the ROS image, we sequentially select the array that minimizes the noise amplification recursively until the desired

number of arrays are selected. To avoid the singularity of the criterion when extending the selection procedure to more samples than unknowns, we propose a modified criterion for the case when the number of unknowns is more than the number of selected samples and the complementary case. We also propose an efficient method to update the criterion based only on the deleted array in the previous step to greatly reduce computational time and avoid the inversion of a huge matrix. This method has great practical potential because it can finish the selection process within half a minute for practical sizes.

The proposed schemes in this dissertation efficiently optimize the MRSI observation in different ways. In general, they will reduce observation time and overcome the problems in various available optimization methods.

## ACKNOWLEDGMENTS

I would like to especially thank my research advisor, Dr. Stanley J. Reeves, for his generous guidance during my Ph.D. study. I would not have finished this dissertation without his valuable ideas on research topics and generous help in real life. I would also like to especially thank Dr. Kai-Hsiung Chang for his generous help during my graduate studies. I would like to thank Dr. Thomas S. Denney for being my committee member and giving me opportunities to use his machine. I would like to thank Dr. Jitendra K. Tugnait and Dr. Amnon J. Meir for being members of my committee. I would like to thank Dr. Donald B. Twieg and Dr. Brad Newcomer at the University of Alabama at Birmingham for providing me real MR data. I would like to thank Charles W. Hayes for sketching a preliminary version of the proof in appendix A. I would also like to thank Dr. Zhi Ding at the University of Iowa for his suggestions.

I would like to thank the Department of Electrical and Computer Engineering, my research advisor, and the Whitaker Foundation for providing financial support. I would like to thank Dr. Nikolaos V. Tsekos and the cardiovascular imaging center in the Washington University School of Medicine for their patience with me.

I would like to especially thank Debbie Reeves, Hsiu-zhu Chang, and Cynthia Rouse for their generous help in my difficulties. I would also like to thank Betty J. Kelly, Jo Ann Loden, Shelia M. Collis, and Jo Ann Smith for their assistance.

Finally, I would like to especially thank my beloved parents, Xin Gao and Shuhua Song, my beloved husband, Heping Jiao, my cherished sons, Gaoliang Jiao and David

A. Jiao, as well as my brothers and sisters whose support and love have made this work possible. This dissertation is dedicated to them.



Style manual or journal used Discrete Mathematics (together with the style known as “auphd”). Bibliography follows van Leunen’s *A Handbook for Scholars*.

---

Computer software used The document preparation package T<sub>E</sub>X (specifically L<sup>A</sup>T<sub>E</sub>X 2<sub>ε</sub>) together with the departmental style-file `auphd.sty`.

---

## TABLE OF CONTENTS

LIST OF FIGURES		xi
LIST OF TABLES		xiv
1 INTRODUCTION		1
1.1 MRI, MRS, and MRSI . . . . .		3
1.1.1 MRI . . . . .		3
1.1.2 MRS . . . . .		8
1.1.3 MRSI . . . . .		10
1.2 MRSI Acquisition Methods and Existing Problems . . . . .		12
1.2.1 Rectangular Sampling . . . . .		12
1.2.2 Multi Spin Echo Imaging . . . . .		13
1.2.3 Hexagonal Sampling . . . . .		16
1.2.4 Other Existing Observation Optimization Strategies . . . . .		16
1.3 Thesis Overview and Contributions . . . . .		19
1.3.1 Overview . . . . .		19
1.3.2 Contributions . . . . .		20
2 EFFICIENT SEQUENTIAL FORWARD SELECTION		23
2.1 Introduction . . . . .		23
2.2 Criteria . . . . .		24
2.2.1 Signal Model . . . . .		24
2.2.2 Standard Criterion . . . . .		24
2.2.3 Modified Criterion . . . . .		25
2.3 SFS Algorithm . . . . .		27
2.3.1 Standard SFS algorithm . . . . .		27
2.3.2 Modified SFS algorithm . . . . .		28
2.4 Efficient Computation For SFS Algorithm . . . . .		30
2.5 Extending the SFS Process . . . . .		33
2.6 Experiments . . . . .		36
2.7 Discussion . . . . .		51
3 EFFICIENT BACKWARD SELECTION OF HEXAGONAL SAMPLES IN K-SPACE		55
3.1 Introduction . . . . .		55
3.2 Selection algorithm . . . . .		56
3.3 Regular Hexagonal Sampling . . . . .		58
3.4 Generalized Multidimensional Discrete Fourier Transform . . . . .		62

3.5	Experiments . . . . .	65
3.6	Conclusion . . . . .	68
4	SEQUENTIAL BACKWARD ARRAY SELECTION	70
4.1	Introduction . . . . .	70
4.2	The Mathematics of Sampling . . . . .	70
4.3	Basic Optimization Algorithm . . . . .	74
4.4	Image reconstruction from nonuniform samples . . . . .	79
4.5	Experiments . . . . .	80
4.6	Conclusion . . . . .	83
5	SEQUENTIAL FORWARD ARRAY SELECTION	85
5.1	Introduction . . . . .	85
5.2	Notation . . . . .	85
5.3	Criterion . . . . .	87
5.4	Efficient recursive algorithm . . . . .	88
5.5	Efficient computational method . . . . .	92
5.6	Experiments . . . . .	94
5.7	Conclusion . . . . .	99
6	CONCLUSION AND DISCUSSION	102
6.1	Efficient sequential forward selection . . . . .	102
6.2	Efficient backward selection of hexagonal samples . . . . .	103
6.3	Efficient selection of sample block . . . . .	103
6.4	Efficient sequential forward selection of array . . . . .	103
6.5	Future work . . . . .	104
	BIBLIOGRAPHY	110

## LIST OF FIGURES

1.1	(a) The spin magnetization $M_0$ without the application of the rf pulse, (b) The spin magnetization $M_0$ with the rf field $H_1(t)$ applied. . . . .	4
1.2	Image weighting as a function of TR and TE . . . . .	6
1.3	The replication of elliptical ROS for rectangular sampling of k-space at Nyquist density( $a$ and $b$ are semi major and minor respectively). . . . .	14
1.4	The replication of elliptical ROS for hexagonal sampling of k-space at Nyquist density . . . . .	17
2.1	(a) The real image, (b) The ROS image (white indicates the support region)	37
2.2	(a) The criterion curve versus the number of selected samples with the 128x128 ROS image, (b) The flop curve versus selection step with the 128x128 ROS . . . . .	40
2.3	(a) 5297 optimized k-space sample distribution (the 5168 black dots repre- sent the optimized minimum density, larger gray dots indicates 129 more optimized samples than the minimum density), (b) Absolute difference be- tween the optimized image reconstruction and the fully sampled $128 \times 128$ image. (Dynamic range is scaled by a factor of 5 for greater visibility). . .	42
2.4	(a) The image from the minimum density k-space data(5168 points). (b) The image from 5297 k-space samples (the ROS has been imposed as a constraint in the reconstruction). . . . .	43
2.5	(a) The point spread function from optimized k-space data (b) The point spread function from inverse FFT. . . . .	44
2.6	(a) Lowpass image from FFT, (b) Lowpass recursive solution at iteration 3, (c) Lowpass recursive solution at iteration 20, (d) Lowpass recursive solution at iteration 100. . . . .	45
2.7	(a) Water image from the full $64 \times 64$ real MRSI data, (b) Fat image from the full $64 \times 64$ real MRSI data, (c) The $64 \times 64$ ROS image (white indicates the support region), (d) $48 \times 48$ ROS image extracted from the $64 \times 64$ ROS (white indicates the support region), (e) $48 \times 48$ water image extracted from the $64 \times 64$ real water image, (f) $48 \times 48$ fat image extracted from the $64 \times 64$ real fat image. . . . .	47

2.8	(a) 1513 optimized k-space data distribution with $64 \times 64$ FOV (the minimum optimized 1439 points indicated by black dots, larger gray dots indicate 74 more samples than the minimum density), (b) 1513 optimized k-space samples with a reduced $48 \times 48$ FOV (the minimum optimized 1439 points indicated by black dots, larger gray dots indicate 74 more samples than the minimum density). . . . .	48
2.9	(a) Noise criterion curve versus the number of selected samples with the $48 \times 48$ ROS, (b) Flops per selection step versus the number of selected samples with the $48 \times 48$ ROS. . . . .	50
2.10	(a) Optimized PSF inside the ROS for a reduced $48 \times 48$ FOV, (b) Lowpass PSF for $48 \times 48$ FOV with 1513 lowpass k-space samples, (c) Lowpass PSF for $64 \times 64$ FOV with 1513 lowpass k-space samples. . . . .	51
2.11	(a) Water image reconstructed from the 1513 optimized k-space samples with $64 \times 64$ FOV with ROS constraint imposed, (b) Fat image reconstructed from the 1513 optimized k-space samples with $64 \times 64$ FOV with ROS constraint imposed. . . . .	52
2.12	(a) Absolute difference between the optimized water image reconstruction and the fully sampled $64 \times 64$ image (b) Absolute difference between the optimized fat image reconstruction and the fully sampled $64 \times 64$ image. (Dynamic range is scaled by a factor of 5 for greater visibility). . . . .	52
2.13	$48 \times 48$ FOV reconstruction: (a) Water image reconstructed from the 1513 optimized k-space samples with ROS constraint imposed, (b) Fat image reconstructed from the 1513 optimized k-space samples with ROS constraint imposed, (c) Water image from the 1513 lowpass k-space samples, (d) Fat image from the 1513 lowpass k-space samples. . . . .	53
2.14	(a) Absolute difference between the optimized water image reconstruction and the $48 \times 48$ extracted image, (b) Absolute difference between the optimized fat image reconstruction and the $48 \times 48$ extracted image. (Dynamic range is scaled by a factor of 5 for greater visibility). . . . .	54
3.1	(a) Hexagonal sampling pattern, (b) Hexagon . . . . .	61
3.2	Smith form decomposition flowchart . . . . .	64
3.3	(a) $96 \times 96$ image, (b) $96 \times 96$ ROS, (c) Reconstructed image from 5550 rectangular k-space samples, (d) Reconstructed image from 5550 hexagonal k-space samples. . . . .	66

3.4	Criterion curves versus samples remaining. . . . .	67
3.5	Time versus samples remaining. . . . .	67
4.1	typical sampling pattern. . . . .	71
4.2	Hexagonal sampling pattern. . . . .	72
4.3	Periodic nonuniform sampling example. . . . .	73
4.4	(a) The $64 \times 64$ region of support (3205 unknowns) (b) 3584 selected samples in the case 1 (c) 3328 selected samples in the case 2 (d) 3328 selected samples in the case 3 (black markers indicate selected samples) . . . . .	82
4.5	(a) The $128 \times 128$ region of support (white points indicate 3205 unknowns) (b) 3328 selected samples in Case 4 . . . . .	83
5.1	(a) The $64 \times 64$ region of support (3205 unknowns) (b) 3328 selected samples in Case 1 (c) 3328 selected samples in Case 2 (d) 3328 selected samples in Case 3 (black markers indicate selected samples) . . . . .	96
5.2	(a) The $128 \times 128$ region of support (white points indicate 3205 unknowns) (b) 3328 selected samples in Case 4 (c) 4096 selected samples in Case 4. . . . .	97
5.3	(a) The semilog criterion curve in Case 2 (b) The semilog criterion curve in Case 4 . . . . .	100

LIST OF TABLES

2.1	Comparison of the criterion and time versus tol . . . . .	39
2.2	Comparison of the selection criterion and time versus FOV with MRSI ROS image . . . . .	46
4.1	Comparison of the criterion in three cases . . . . .	81
5.1	Comparison of the criterion in four cases . . . . .	98
5.2	Comparison of the criterion in four cases . . . . .	98

## CHAPTER 1

### INTRODUCTION

Magnetic resonance spectroscopic imaging (MRSI) is an extension of localized magnetic resonance spectroscopy (MRS), which allows collection of *in-vivo* spectroscopic information from multiple regions simultaneously. MRSI is a completely non-invasive method for obtaining quantitative biochemical information [1], which shows great promise for use in basic physiological research and for clinical imaging of metabolic function [2,3]. The information acquired with MRSI is shown as either spectral line plots at a particular location or images of metabolite distributions, which can be used to assess regional metabolic abnormalities in various pathologies. In recent years, spectroscopic imaging studies have been performed on a large number of pathologies [3]. <sup>1</sup>H MRSI studies have indicated both focal and global metabolic changes in a variety of diseases including brain tumors [4–9], sub-acute and acute cerebral infarction [10, 11], multiple sclerosis [12, 13], AIDS dementia [14, 15], Alzheimer’s disease [16–18], and epilepsy [19–21]. Most of these diseases present challenges to neuronal viability, which relate to a reduction in the NAA concentration. For instance, a reduction in the NAA concentration was shown in severely affected areas in stroke. Lactate is often increased in the same regions, indicating ischemia [22]. The observed regional reduction of NAA could mark onset of Alzheimer’s disease in an early stage. Observed reductions in brain myo-inositol could indicate alterations in liver biochemistry [18]. In addition, an increase of choline is observed in most malignant brain tumors. For example, the choline increase has been found to correlate with tumor grade in astrocytomas [11]. On the other hand, applications of phosphorus



MRSI have focused on energy metabolism in the human brain, in skeletal muscle and cardiac muscle [23–25]. For example, metabolic changes have been observed in the brain due to tumors [26] and epilepsy [21]. ATP depletion was found to indicate infarcted regions in the cardiac muscle [25].

MRSI requires dedicated acquisition techniques because it combines elements from MRS and magnetic resonance imaging (MRI) [1, 3, 27, 28]. Despite its potential, MRSI has remained largely in a research setting because a relatively long time is required to acquire the images. In order for MRSI to reach its full potential in a clinical environment, the acquisition time must be reduced. When prior knowledge of the image is available, it may be possible to reconstruct the image from a subset of k-space samples. Examples of such prior knowledge are region of support, locations of anatomical boundaries, and relative smoothness of various image areas. Given this potential for reducing the number of k-space samples, we desire to choose the best possible combination of these samples to guarantee the quality of the reconstructed image. Towards this end, we are pursuing strategies where the imaging process is optimized so that only the most significant portions of the data set are acquired. The strategies we are developing have demonstrated significant reductions in imaging time with minimal noise amplification and no reduction in resolution.

## 1.1 MRI, MRS, and MRSI

### 1.1.1 MRI

MRI is a completely non-invasive method for imaging soft tissues and other structures in the body. MRI makes use of the nuclear magnetic resonance (NMR) phenomenon, which was discovered in 1946 [29], to obtain a proton density image of a given object. The history of MRI based on the principle of NMR goes back to the early 1970s. At that time both Lauterbur [30] and Damadian [31] proposed that NMR spectroscopic techniques could be applied to human imaging. Andrew *et al.* [32, 33] demonstrated that NMR imaging could show the details of the human anatomy. Subsequent images obtained by Moore *et al.* [34] and Holland *et al.* [35] proved NMR tomography is indeed capable of performing diagnostic imaging. Since MRI became clinically viable about 15 years ago, it has proven itself as an important diagnostic tool for a wide variety of health problems. MRI is unique in that it exploits a magnetic moment called spin, which is a physical property possessed by certain atomic nuclei such as those of hydrogen (protons). It is completely noninvasive and appears to be safe for children and probably even for pregnant women.

#### **The Physics of MRI** [1, 29, 36–41]

All materials contain nuclei, which are protons, neutrons, or a combination of both [39]. Nuclei that have an odd number of protons, neutrons, or both in combination, possess a nuclear *spin* or a magnetic moment. Under normal circumstances, these atomic nuclei in a sample are aligned randomly, and therefore their magnetic moments cancel each other and no signal can be measured. However, if a sample is placed into a powerful static magnetic field  $\mathbf{H}_0$ , spins align themselves with the external field either in a parallel

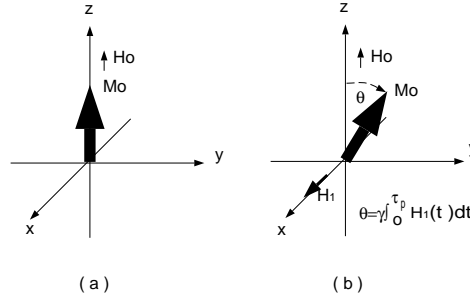


Figure 1.1: (a) The spin magnetization  $M_0$  without the application of the rf pulse, (b) The spin magnetization  $M_0$  with the rf field  $H_1(t)$  applied.

direction (in low-energy state) or in an antiparallel direction (in high-energy state) and start to precess at the Larmor precession frequency, which is proportional to the magnetic field strength. At thermal equilibrium, the net spin magnetization vector  $\mathbf{M}_0$  is along the external magnetic field  $\mathbf{H}_0$ . When an rf signal is applied to the system in the form of an rf magnetic field  $H_1$ , those protons in the lower-energy state tend to be excited to the higher-energy state and as a result,  $\mathbf{M}_0$  can be rotated or flipped by any angle  $\theta$ . After cessation of the rf magnetic field  $H_1$ , the excited protons tend to return to their low-energy state by emitting a well-defined rf frequency (i.e. the same frequency as the applied rf) by spin relaxation mechanisms such as spin-lattice and spin-spin relaxations, and  $\mathbf{M}_0$  lines up with  $\mathbf{H}_0$  again. This emission of rf signals is then picked up by an rf coil placed close to the excited object. This signal is called a *free induction decay* (FID), which is the central part of NMR imaging. The spin magnetization in the rotating frame with and without an rf pulse is shown in Figure 1.1. The flip angle  $\theta$  of the magnetization  $M_0$  is given by  $\theta = \gamma \int_0^{\tau_p} H_1(t) dt$ , where  $H_1(t)$  is the time-varying rf field intensity and  $\tau_p$  is the application length of the rf pulse. The angle  $\theta$  is typically set to  $90^\circ$  or  $180^\circ$ .

The two relaxation mechanisms are the transverse or spin-spin relaxation known as  $T_2$  relaxation and the longitudinal or spin-lattice relaxation known as  $T_1$  relaxation. Both of these relaxations and their respective relaxation times ( $T_1$  and  $T_2$ ) are quite sensitive to the molecular structures and the environments surrounding the nuclei. For example, the mean  $T_1$  and  $T_2$  values of normal tissues and those of many malignant tissues differ significantly, thereby allowing us to differentiate malignant tissue from normal tissues [1]. The imaging capabilities of these two important parameters,  $T_1$  and  $T_2$ , together with the spin densities and the flow-dependent phase information of the objects, make NMR imaging a unique, versatile, and powerful technique in diagnostic imaging.

Three widely used spin-echo techniques play an essential role in data acquisition for NMR and NMR imaging: the HAHN spin-echo technique [42], the CPMG technique [43, 44], and the stimulated echo techniques [42, 45]. Both Hahn and CPMG techniques have wide applications in all phases of NMR and NMR imaging to overcome several adverse effects that often arise in experimental situations, such as the effects of the gradient pulse rise time and the field inhomogeneity. The same goal can be achieved with stimulated echo but without suffering additional  $T_2$  decay.

In a typical spin echo sequence, the RF pulses are repeated many times; the interval between the repeated pulses is called the repetition time (TR). The interval in the pulse sequence between the end of the RF pulse and the detection of the returning MR signal is called the echo time (TE). By adjusting proper combinations of TR and TE, the image will show contrast related mainly to differences in proton density,  $T_1$  relaxation time, or  $T_2$  relaxation time of the tissue — in other words, the image is proton density weighted,  $T_1$  weighted or  $T_2$  weighted. If long TR and long TE are chosen so that  $T_1$  differences

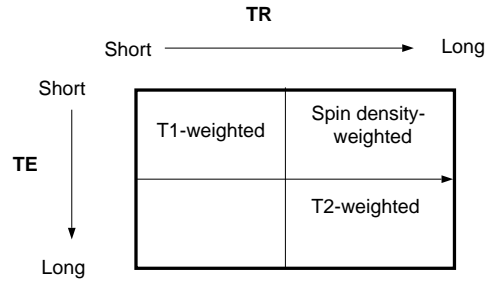


Figure 1.2: Image weighting as a function of TR and TE

are responsible for the observed contrast, the image is said to be T1-weighted. If short TR and short TE are chosen so that T2 differences are responsible for the observed contrast, the image is said to be T2-weighted. If long TR and short TE are selected so that both the T1 and T2 effects are minimized, then the image is said to be spin density- or proton density-weighted. Figure 1.2 shows these weighting rules.

In NMR imaging or MRI, a field gradient or a set of gradients is deliberately added to resolve the spatial distribution of spins by Fourier encodings. The basic form of the signal obtained can be expressed as [46–48]

$$s(t) = M_0 \int \int \int_{-\infty}^{\infty} \rho(x, y, z) \exp\{-i\gamma \int_0^t [xG_x(t') + yG_y(t') + zG_z(t')] dt'\} dx dy dz \quad (1.1.1)$$

The resulted FID or echo is in effect a Fourier transform-domain representation of the spatially distributed spin density. Many imaging algorithms can be derived from this basic form of the 3-D equation.

From the basic imaging equation in (1.1.1), a 3-D discrete imaging equation can be obtained by discrete Fourier encoding. Fourier-domain scanning uses both frequency and phase encodings. Discrete Fourier encoding can be achieved by changing the gradient

amplitude (or its length):

$$S(g_x, t_y, g_z) = M_0 \int \int \int \rho(x, y, z) \exp[-i\gamma(xg_x T_x + yG_y T_y + zg_z t_z)] dx dy dz \quad (1.1.2)$$

where  $g_x = n\Delta G_x$  and  $g_z = n\Delta G_z$ .  $\Delta G_x$  and  $\Delta G_z$  are the increments of the  $x$ -gradient amplitude and  $z$ -gradient amplitude, and  $n$  denotes the step number of the phase encoding gradient. The pulse length can also be varied provided that the pulse amplitude is kept constant. However, the former phase encoding method is more widely used due to the fact that the constant time or pulse width  $T_x$  employed in the former eliminates NMR parameter-dependent signal variations such as  $T_2$  decay [1]. The  $y$ -gradient  $G_y$  is used as the readout gradient, which is also the frequency-encoding gradient. This is distinguished from the phase-encoding gradients which in this case are the  $x$ -gradient and  $z$ -gradient. The number of phase encoding steps determines the  $x$ -directional and  $z$ -directional resolution, while the  $y$ -directional resolution remains constant regardless of the number of encoding steps employed. Theoretically the resolution of the  $y$ -directional resolution can be infinitely high. However, in most cases the resolution in the  $y$ -direction is limited by the bandwidth of the NMR data, the sampling interval, the frequency response of the electronics, and the SNR. In practical NMR imaging, the resolution is therefore largely determined by the number of phase encoding steps employed (e.g., the  $x$ -gradient and the  $z$ -gradient in this case) provided that the signal has a sufficient SNR. Other important physical parameters involved in NMR imaging are the spin-lattice and spin-spin relaxation times  $T_1$  and  $T_2$ . The increased phase encoding steps will improve resolution but cause long imaging time. If we let  $w_x = \gamma g_x T_x$ ,  $w_y = \gamma G_y t_y$ , and

$w_z = \gamma g_z T_z$ , (1.1.2) can be rewritten as

$$S(w_x, w_y, w_z) = M_0 \int \int \int \rho(x, y, z) \exp[-i(w_x x + w_y y + w_z z)] d_x d_y d_z \quad (1.1.3)$$

The 3-D density function can be obtained by taking a 3-D inverse Fourier transform of  $S(w_x, w_y, w_z)$ :

$$\rho(x, y, z) = c \int \int \int S(w_x, w_y, w_z) \exp[-i(w_x x + w_y y + w_z z)] d_{w_x} d_{w_y} d_{w_z} \quad (1.1.4)$$

where  $c$  is a constant. 2-D Fourier imaging can be derived directly by setting  $z = z_0$  as

$$S(w_x, w_y) = M_0 \int \int \rho(x, y, z = z_0) \exp[-i(w_x x + w_y y)] d_x d_y \quad (1.1.5)$$

and

$$\rho(x, y, z = z_0) = c \int \int S(w_x, w_y) \exp[-i(w_x x + w_y y)] d_{w_x} d_{w_y} \quad (1.1.6)$$

### 1.1.2 MRS

Because the magnetic field in the vicinity of a nucleus is influenced by the local conditions, the Larmor frequencies for two different nuclei of the same species may be shifted apart. This phenomenon is also known as chemical shift. The Larmor frequencies for two different nuclei of the same species are given by

$$v_k = \gamma(1 - \sigma_k)B_0 \quad (1.1.7)$$

$$v_{ref} = \gamma(1 - \sigma_{ref})B_0 \quad (1.1.8)$$

where  $\sigma_k$  and  $\sigma_{ref}$  are the screening (or shielding) constants of the sample and the reference materials, respectively, due to the diamagnetic, paramagnetic, and interatomic current effects. The chemical shift is defined as the difference of these two equations:

$$w_k \equiv v_k - v_{ref} = \gamma(\sigma_{ref} - \sigma_k)B_0 \quad (1.1.9)$$

To eliminate the field dependency of  $w_k$ , a relative chemical shift  $\delta_k$  is defined as

$$\delta_k = \frac{\sigma_{ref} - \sigma_k}{1 - \sigma_{ref}} \times 10^6 ppm \quad (1.1.10)$$

In proton NMR spectroscopy, tetramethylsilane (TMS) is a typical reference material. A positive value of  $\delta_k$  indicates that the nuclei of the sample resonate at a frequency higher than the reference material. In a high magnetic field the spectrum of a particular substance may be resolvable into several peaks due to the chemical shift, and the frequency difference between the peaks becomes larger with increasing magnetic field strength  $B_0$ . Therefore, chemical shift plays a key role in NMR spectroscopy.

Magnetic resonance spectroscopy is a unique tool in that it can noninvasively obtain quantitative biochemical information. Proton magnetic resonance spectroscopy plays an important role for the study of *in vivo* metabolites in animals and humans [49–55]. Phosphorus spectroscopy plays a key role in NMR spectroscopy especially in *in vivo* human studies [56, 57]. However, most of the spectroscopy techniques critically depend upon the quality of the spectral resolution that can be obtained. Good resolution can be achieved by optimizing the magnetic field homogeneity over the sample volume of interest by localization techniques. A number of volume localization techniques have been



developed such as rotating-frame zeugmatography [58,59], DRESS [60], SPARS [61,62], STEAM [50,63] and other techniques using high-order gradient fields and multidimensional localization [49,51–56,64–77].

### 1.1.3 MRSI

MRSI is a combination of MRS and MRI. MRSI differs from conventional spectroscopy in that the spectroscopic information is presented in the form of an image instead of in the form of a graph. Consequently, MRSI gives results which are readily interpretable in a qualitative sense and allows collection of *in vivo* spectroscopic data from multiple regions simultaneously. It shows great promise for use in basic physiological research and for clinical imaging of metabolic function [2]. Spectroscopic imaging studies have been performed on a large number of pathologies [3].  $^1\text{H}$  MRSI studies have indicated both focal and global metabolic changes in a number of diseases including brain tumors [4–9], sub-acute and acute cerebral infarction [10,11], multiple sclerosis [12,13], AIDS dementia [14,15], Alzheimer’s disease [16–18], and epilepsy [20]. Most of these diseases cause a reduction in the NAA concentration and challenges to neuronal viability [3]. Applications of phosphorus MRSI have focused on energy metabolism in the human brain, skeletal muscle and cardiac muscle [23–25]. For instance, Metabolic changes have been observed in the brain due to brain tumors [26] and epilepsy [21]. ATP depletion was found in the cardiac muscle to indicate infarcted regions [25].

MRSI can be expressed in the form of four-dimensional Fourier NMR imaging [27], which offered new possibilities of doing spatially resolved high-resolution spectroscopy.

This 4-D NMR technique is a variation of the three-dimensional Fourier imaging technique with an additional spectral dimension. The new spectral dimension indicates the chemical shift information. The acquired data in the frequency domain is then transformed into the spatial domain by an inverse four-dimensional Fourier transform to generate the NMR spectra as well as the 3-D image – in other words, the NMR spectrum at each voxel in the spatially resolved 3-D volume image. The observed NMR signal is given by

$$S(w_x, w_y, w_z, t_x) = \int_{w_k} \int_z \int_y \int_x \rho(x, y, z, w_k) \exp[-i(w_x x + w_y y + w_z z + w_k t_k)] d_x d_y d_z d_{w_k} \quad (1.1.11)$$

where  $w_x = \gamma g_x T_x$ ,  $w_y = \gamma g_y T_y$ , and  $w_z = \gamma g_z T_z$ ,  $g_x$ ,  $g_y$ , and  $g_z$  are the amplitude variables of the  $x$ ,  $y$ , and  $z$  gradients, and  $T_x$ ,  $T_y$ , and  $T_z$  are constant time intervals. A three-dimensionally resolved volume spectral image can be reduced to a two-dimensional slice spectral image by converting any one of the three coding gradients into the selection gradient.

The standard MRSI protocol is to acquire a set of k-space samples on a rectangular grid and perform an inverse Fourier transform on the acquired data to obtain the spatial-domain image and the NMR spectrum. Full four-dimensional Fourier imaging requires an imaging time of  $N_x N_y N_z T_R$  seconds for spectrally resolved 3-D volume imaging.  $N_x$ ,  $N_y$ ,  $N_z$  and  $T_R$  are the number of encoding steps of the  $x$ ,  $y$ ,  $z$  gradients and repetition time, respectively. Then  $N_x$ ,  $N_y$ , and  $N_z$  will represent the number of image pixels in the spatial domains  $x$ ,  $y$ , and  $z$ . Quite a large number of coding steps will be required even for the case of 2-D slice-selected spectroscopic imaging, and they are often too long for human *in vivo* imaging. This limitation results in truncated k-space data, which

causes ringing and limits the resolution of the reconstructed image. However, increased resolution is particularly important for making MRSI a clinically viable technique. For example, the use of MRSI to localize and assess brain tumors [7] and multiple sclerosis [78] as well as to determine the seizure focus of temporal lobe epilepsy [19] will all require increased resolution. A number of image modeling techniques have been proposed to incorporate a priori information from a proton-density MR imaging study to improve the resolution of the MR spectroscopic image of the same object [79–81]. When these image models are imposed on the image reconstruction process, the combination of k-space samples acquired can have a considerable effect on the quality of the reconstructed image. In this thesis, we consider images with a limited region of support (ROS). When the image has a limited region of support (ROS), it is possible to reconstruct the image from a subset of k-space samples. Therefore, we desire to develop strategies to choose the best possible combination of a reduced set of k-space samples to guarantee the quality of the reconstructed image while reducing the imaging time required. This is the goal of the thesis.

## **1.2 MRSI Acquisition Methods and Existing Problems**

### **1.2.1 Rectangular Sampling**

Rectangular sampling acquires a set of k-space samples on a rectangular grid. The spatial-domain image is reconstructed by performing an inverse Fourier transform on the acquired data. This is the standard MRSI protocol. If the spatial extent of the image is limited, rectangular sampling at the Nyquist rate will permit accurate reconstruction with no spatial aliasing (overlapping of the periodic images). Rectangular sampling

may be formally defined as sampling on a regular lattice whose basis vectors form an orthogonal set. The basis vectors need not be of equal magnitude. However, the time required to gather the data while maintaining an adequate signal-to-noise ratio (S/N) limits the number of k-space samples that can be acquired, which we have discussed in the previous section. This limitation is typically addressed by limiting the k-space acquisition to low spatial-frequency samples, which causes ringing and limits the resolution of the reconstructed image. On the other hand, in two or more dimensions rectangular sampling is inefficient if the image is isotropically spatially limited. Consider rectangular sampling of k-space for an image with a 2-D circular or elliptical ROS at Nyquist density. As shown in Figure 1.3, gaps exist among the replications. In the 2-D case, the mean sampling density is  $\frac{4}{\pi}$  as dense as the minimum sampling density required to avoid aliasing. This translates into 27% more time to obtain an image than is necessary, which can be critical in MRSI. Therefore, various other sampling schemes have been proposed to optimize the sampling strategy.

### 1.2.2 Multi Spin Echo Imaging

Multi-spin echo imaging is a class of rapid imaging techniques that includes *echo planar imaging* (EPI) and *spiral scan echo planar imaging* (SEPI).

Mansfield was the first to propose EPI. This method, in principle, allows us to obtain 2-D image data by a single excitation [82] and can be extended to a 3-D form. First, a slice of thickness  $\Delta z$  is selected by applying  $G_z$  together with a  $90^\circ$  selective rf pulse. Then an oscillating  $G_x$  and a small constant gradient  $G_y$  are applied. The generated

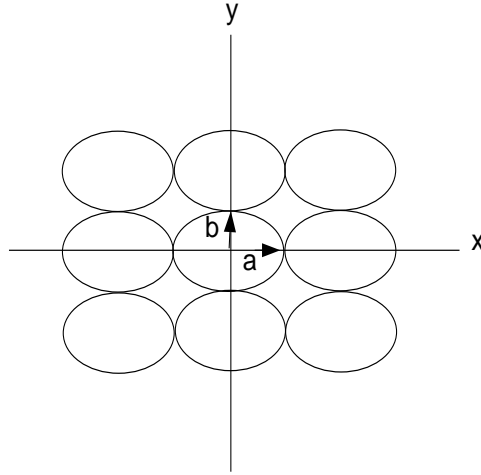


Figure 1.3: The replication of elliptical ROS for rectangular sampling of k-space at Nyquist density( $a$  and  $b$  are semi major and minor respectively).

FID and echoes can be written as

$$f(t) = \left\{ \sum_{n=0}^{\infty} g_n(t - 2n\pi) \exp\left(-\frac{t}{T_2}\right) \right\} \quad (1.2.1)$$

where  $g_n(t - 2n\pi)$  is the echo signal:

$$g_n(t - 2n\pi) = s(t) \quad (1.2.2)$$

The entire frequency or k-space can be covered with a single  $90^\circ$  rf pulse excitation by adjusting  $G_x$  and  $G_y$ . However, there exist some problems in EPI. One problem is that  $T_2$  decay requires a rapidly alternating gradient pulse of large amplitude, which is often difficult to obtain in practice. Another problem in EPI is the poor resolution in the

phase encoding direction due to the limitation in the number of phase encoding steps or the number of echoes that can be recalled due to the signal decay by  $T_2$ .

Some of the difficulties in the original EPI such as the resolution limits in the phase encoding direction can be partially resolved by the application of a spiral scan in k-space known as SEPI [75]. The spiral scan represents a close approximation of the concentric circles with which the entire frequency range of interest can be covered uniformly [83], thereby achieving approximately circularly symmetric resolution. The required k-space radial and angular sampling rates can be defined as

$$\Delta k_r = \frac{2\pi}{2N_r} \quad (1.2.3)$$

$$\Delta k_\theta = \frac{2\pi}{N_\theta} \quad (1.2.4)$$

where  $N_r$  and  $\Delta r$  denote the number of rotations in the k-domain and the image resolution in the spatial domain, respectively. The total required image data acquisition time  $T_D$  is given by multiplication of angular incremental time  $\Delta T$ , the number of rotations, and the number of samples in one complete revolution.

$$T_D = N_r N_\theta \Delta T \quad (1.2.5)$$

The main advantage of SEPI over standard EPI is the conjugate symmetry property of the spiral scan. This property allows the sampling rate to be increased by a factor of 2. One of the drawbacks of SEPI is that the complex 2-D interpolation of the polar coordinate data to Cartesian data is necessary for using an FFT to reconstruct the spatial image to display. Another drawback is that the samples on the circles near the origin are

too close while the samples on the outermost circles are too wide apart, causing either wasting of time or aliasing and increasing the complexity of the interpolation.

Multi-spin echo imaging techniques are inappropriate for standard MRSI, since the standard MRSI protocol uses the readout direction for the spectroscopic information and each point in k-space must be acquired by a separate excitation sequence. But they can be adapted to MRSI with some modifications [84–88].

### 1.2.3 Hexagonal Sampling

Hexagonal sampling [89] allows an image with an elliptical ROS to be reconstructed with no aliasing from fewer data points than rectangular sampling. Hexagonal sampling at the Nyquist rate has a 13.4% efficiency gain over rectangular sampling at the Nyquist rate and yields the most densely packed spatial replications for space-limited signals [90, 91]. However, Nyquist density sampling cannot reach the minimum density for an elliptical ROS image. Consider hexagonal sampling of k-space for an image with a 2-D circular or elliptical ROS at Nyquist density. As shown in Figure 1.4, gaps exist among the replications. Minimum density sampling yields samples linearly independent of each other, which cannot be reached through this uniform sampling strategy.

### 1.2.4 Other Existing Observation Optimization Strategies

The problem of optimizing the choice of k-space samples has also been addressed in various other ways. Von Kienlin *et al.* [92] introduced a criterion for optimizing the k-space samples using the SLIM [79] model for the image. This model assumes that the image is made up of homogeneous regions. The proposed criterion is based on the

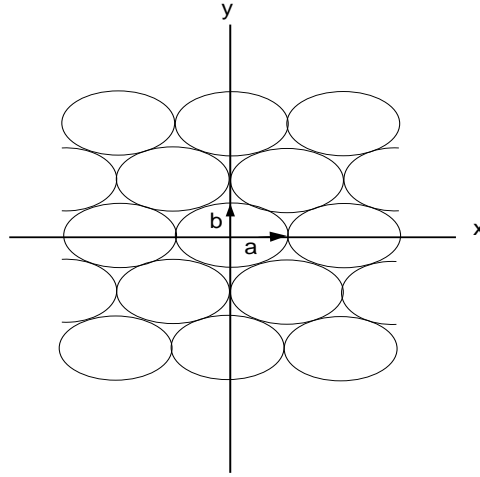


Figure 1.4: The replication of elliptical ROS for hexagonal sampling of k-space at Nyquist density

resulting point-spread function. However, their final criterion must be numerically optimized by a multidimensional nonlinear optimization algorithm, and the criterion contains multiple local minima. Furthermore, the criterion has only an indirect relation to image quality. Cao and Levin [93] used an image database to constrain the reconstructed image to a limited set of basis images and optimized the choice of k-space samples to minimize mean square error (MSE) in the reconstruction. The problem with this approach is that it may overly constrain the reconstruction when one is attempting to detect anomalies in the image. Furthermore, the authors did not propose an efficient optimization method. Plevritis and Mackovski [94] proposed a heuristic k-space selection method based on finding the highest-energy k-space locations of a binarized scout image. While this method may improve reconstruction results as compared to lowpass sampling, it has no clear connection to any measure of optimality in the reconstructed image.



Recognizing the combinatoric problem inherent in the previous approaches, two independent groups have proposed an alternative sampling scheme called coset sampling [95–97]. In this scheme, k-space is divided into rectangular blocks and the same irregular pattern of samples is selected within each block so that the sampling scheme becomes block-periodic. This approach is quite effective and reduces the optimization problem considerably under certain conditions. However, to achieve a significant reduction in the sampling density, the ROS must be well approximated by a collection of rectangles. Reeves *et al.* proposed sequential backward selection (SBS) [98,99] and sequential forward selection (SFS) [100] based on minimizing MSE in the reconstructed image. However, SBS cannot be implemented in real time because SBS eliminates the worst candidate rather than selects the best one. Therefore, observation cannot begin until the whole selection process finishes. The SFS algorithm based on MSE does not apply when there are more unknowns than selected samples, because the criterion is undefined in this case. Thus, the SFS algorithm cannot begin with no samples selected.

In addition to optimizing MRSI data acquisition, the techniques proposed here can be used for 3-D MRI. In the case of 3-D MRI the readout direction is used to sample along a line in the third k-space dimension, so these lines will appear as individual k-space points in the first two k-space dimensions. Therefore, if the 3-D image has a limited ROS in every slice along a particular dimension, the proposed algorithm can be used without modification to select the k-space distribution. The most efficient acquisition would use echo-volume imaging to traverse several selected k-space lines for every excitation period. The only restriction is that in the optimization algorithm we must use an ROS that completely contains the ROS at each slice. However, a relative shift of the ROS

from slice to slice will not affect the optimal set of k-space samples for that slice, since the criteria in (2) and (8) are unaffected by shifts of the ROS. We have proved this assertion in the appendix.

### 1.3 Thesis Overview and Contributions

#### 1.3.1 Overview

Nyquist density sampling yields the most densely packed spatial replications for space-limited signals, while minimum density sampling yields samples linearly independent of each other but not necessarily uniformly distributed. It can be shown that for 1-D space-limited functions, the two densities (or rates) are identical. For higher-dimensional space-limited functions, Nyquist densities can be significantly higher than minimum densities [101]. This is the rationale for optimized k-space sampling with a limited ROS. If the ROS is smaller than the image, Nyquist sampling represents a redundant sampling of k-space. The multidimensional extension of Papoulis' generalized sampling expansion states that the minimum frequency-sampling density of an M-D space-limited function is equal to the area of the ROS of the function [101]. That is, the minimum number of samples in k-space equals the area of the ROS. However, this theorem does not tell us how to achieve this minimum density sampling without losing any signal information.

In this thesis, we develop four MRSI observation optimization strategies to overcome the existing problems in different ways: 1) efficient SFS [102–104], 2) efficient SBS applied to hexagonal samples [105], 3) efficient SBS for block-periodic sampling [106–108], and 4) efficient SFS for block-periodic sampling. In each case, we develop an efficient optimization criterion based on minimizing the sum of squared errors in the reconstructed

image samples, an efficient computational strategy for the optimization procedure, and in one case an efficient image reconstruction method. These strategies tend to minimize the error criterion, but they do not guarantee the optimal observation selection.

### 1.3.2 Contributions

The contributions we propose are summarized as follows:

- A modified SFS algorithm [102–104] is developed to overcome the problems with standard SFS [100]. This entails the following contributions:
  - We present a modified form of the criterion that overcomes the existing problem for the standard SFS algorithm and develop an SFS algorithm for the new criterion.
  - We develop an efficient computational strategy for the new algorithm as well as the standard SFS algorithm, which drastically reduces storage space and computational time.
  - The combined algorithm can efficiently select a reduced set of k-space samples from which we can reach the minimum density without losing any signal information. Furthermore, if the data is noisy as is the case in MRSI, we can reduce noise amplification considerably by selecting a few more samples than the number of unknowns in the ROS. Simulations with real MR data show that a good-quality image can be reconstructed with only a few more samples than the minimum density with this method.

- It is more applicable in practice than SBS in that the best sample can be observed as soon as it is selected, making possible real-time selection and acquisition.
- We present an efficient SBS algorithm from hexagonal samples when the ROS is approximated by an ellipse. In this method, we make the following contributions:
  - A general periodic matrix FFT is implemented based on a rectangular FFT with the Smith form decomposition. A structured Smith form decomposition is implemented.
  - By choosing an appropriate periodic matrix  $N$ , the hexagonal samples in the frequency domain can be transformed to rectangular samples in the spatial domain without interpolation directly with the generalized FFT. Therefore, artifacts and extra computational time are avoided.
  - An efficient SBS algorithm is applied to hexagonal samples. The combined algorithm efficiently optimizes a reduced set of k-space samples and saves a great deal of selection time in comparison with SBS applied to common rectangular samples. The savings results from the fact that the algorithm begins with fewer samples than with a rectangular grid.
- We develop an SBS algorithm for periodic sample blocks. In this scheme, we make the following contributions:
  - It provides an efficient update formula for the criterion based on convolution kernels rather than large, non-sparse matrices;

- It provides an efficient update formula for the convolution kernels based on the deleted array.
- It provides an efficient reconstruction method based on convolutions rather than matrix inverses. The proposed method dramatically reduces storage and computational complexity.
- We develop an efficient SFS algorithm for periodic sample blocks. In this scheme, we make the following contributions:
  - It provides a modified criterion to avoid the singularity problem when extending the selection process.
  - It provides an efficient update formula for the criterion based only on the previous selected array.
  - It decomposes the block sample algorithm into a combination of single sample algorithms to efficiently solve the complicated array selection problem.
  - It seamlessly integrates the modified SFS algorithm for fewer samples than unknowns with the standard algorithm for more samples than unknowns.
  - It has great practical potential in that it can finish the selection in half a minute for a practical size image.

## CHAPTER 2

### EFFICIENT SEQUENTIAL FORWARD SELECTION

#### 2.1 Introduction

Sequential forward selection (SFS) is appealing as an optimization method because the previously selected sample can be observed while the next sample is selected. SFS tends to minimize the error criterion, but it does not guarantee the optimal observation selection. When the number of selected k-space samples is less than the number of unknowns at the beginning of the selection process, the optimality criterion is undefined and the resulting SFS algorithm cannot be used. In this chapter, we present a modified form of the criterion that overcomes this problem and develop an SFS algorithm for the new criterion. Then we develop an efficient computational strategy for this algorithm as well as for the standard SFS algorithm. The combined algorithm efficiently selects a reduced set of k-space samples from which the ROS can be reconstructed with minimal noise amplification. With the proposed algorithm, we can reach the minimum density without losing any signal information. If the samples are noisy as are the case in MRSI, we can reduce noise amplification considerably with a few more samples than the number of unknowns in the ROS. Furthermore, the proposed algorithm brings real-time implementation closer to reality because the previously selected sample can be observed while the next sample is selected.

## 2.2 Criteria

### 2.2.1 Signal Model

We model the observed k-space samples  $y$  as a vector resulting from a linear transformation of the original image  $x$  in the presence of additive noise  $w$ ; that is

$$y = Ax + w \tag{2.2.1}$$

where  $w$  is zero-mean, independently identical distributed (i.i.d.) noise and  $A \in C^{m \times n}$ ,  $m$  and  $n$  are integers. Given the observed signal  $y$ , the goal is to reconstruct a good estimate of  $x$ . We want to select the limited set of observations that will yield the best possible reconstruction of  $x$  by using the known mapping from the original to the observations. This is equivalent to choosing rows for  $A$  that correspond to the best set of observations  $y$ . For MRI and MRSI,  $A$  represents a Fourier transform matrix with columns removed corresponding to the voxels outside the ROS.

### 2.2.2 Standard Criterion

If the noise is zero-mean, i.i.d. and the reconstruction of  $x$  is performed via least squares, we can define a criterion  $E(A)$  that is proportional to the mean square error in the reconstruction [109] as

$$E(A) = \text{tr}(A^H A)^{-1} \tag{2.2.2}$$

Obviously, the criterion is not defined when  $A$  has fewer rows than columns. A critical limitation of the SFS algorithm based on this criterion is that it only applies

when the initial matrix has a column rank of  $n$ . A necessary condition, therefore, is that  $A$  have at least  $n$  rows to begin the update process [100]. Consequently, this criterion can not be used directly for an SFS algorithm that starts with no selected observations. Therefore, in the next section we present a modified form of the selection criterion that uses a pseudo-inverse in place of the inverse to make the initial selection process possible. We optimize the selection process based on the modified criterion until  $A$  is square. Afterwards, we switch the selection process to the standard algorithm.

### 2.2.3 Modified Criterion

When  $A$  has fewer rows than columns, we propose to use the following modified criterion:

$$E(A) = \text{tr}(A^H A)^+ \quad (2.2.3)$$

where  $(A^H A)^+$  is the pseudo-inverse of  $A^H A$ . Let  $U^H A V = \Sigma$  be the singular value decomposition (SVD) of  $A \in C^{m \times n}$  with  $r = \text{rank}(A)$ . Then  $(A^H A)^+ = V(\Sigma^H \Sigma)^+ V^H$ , where

$$(\Sigma^H \Sigma)^+ = \text{diag}\left(\frac{1}{\sigma_1^2}, \dots, \frac{1}{\sigma_r^2}, 0, \dots, 0\right), \quad (2.2.4)$$

and  $\sigma_i$  is the  $i$ th diagonal entry of  $\Sigma$ . Now, we consider the validity of the modified criterion and its relation to the standard criterion. The minimum-norm least-squares solution is given by

$$\begin{aligned} x_{LS} &= (A^H A)^+ A^H y \\ &= \sum_{i=1}^r \eta_i \eta_i^H x + (A^H A)^+ A^H w \end{aligned} \quad (2.2.5)$$



and

$$x = VV^H x = \sum_{i=1}^n \eta_i \eta_i^H x \quad (2.2.6)$$

where  $x$  is the ideal solution with  $A$  full rank and no noise and  $\eta_i$  is the  $i$ th column vector of  $V$ . Then,

$$\begin{aligned} E\|x - x_{LS}\|^2 &= \left\| \sum_{i=r+1}^n \eta_i \eta_i^H x \right\|^2 + \sigma_w^2 \text{tr}(A(A^H A)^+(A^H A)^+ A^H) \\ &= \sum_{i=r+1}^n \|x^T \eta_i\|^2 + \sigma_w^2 \text{tr}(A^H A)^+ \end{aligned} \quad (2.2.7)$$

When  $A$  is underdetermined, there are two parts in the error. One part is due to the loss of signal components; the other is due to noise. The error due to the loss of these signal components is not reflected in the modified criterion. However, the criterion does reflect the noise error. Thus, the criterion still provides a useful indicator of the degree to which the available components suppress or amplify noise. When a new row is selected, the number of zeroed signal components ( $n - r$ ) will decrease by one, and the corresponding noise will be reflected in the criterion and increase the criterion value. Therefore, we can choose the best new row based on the modified criterion such that the criterion increases by the minimum value. When at least  $n$  rows are ultimately to be selected, the error in the reconstructed signal due to the zeroed signal components will eventually disappear, and the pseudo-inverse criterion will be equivalent to the original inverse criterion. This justifies our neglect of the signal error component in using the modified error criterion.

Having modified the criterion, we can no longer use the standard SFS algorithm to optimize it. Note that  $AA^H = U(\Sigma\Sigma^H)U^H$ . Therefore,

$$E(A) = \text{tr}(A^H A)^+ = \sum_{i=1}^n \frac{1}{\sigma_i^2} = \text{tr}(AA^H)^{-1} \quad (2.2.8)$$

Now, the form of the criterion given by (2.2.8) no longer needs a pseudo-inverse and consequently is much more tractable as the basis of a selection algorithm.

## 2.3 SFS Algorithm

### 2.3.1 Standard SFS algorithm

Standard SFS begins with a matrix  $A$  with the number of rows at least equal to the number of columns, or equivalently, with the number of selected observations at least equal to the number of unknowns. It then sequentially selects the row that reduces the MSE criterion the most at each step until the desired number of rows are selected. Let  $A_+$  represents the new matrix after the  $i$ th row  $a_i$  is added to matrix  $A$ . Using the Sherman-Morrison matrix inversion formula [110] gives

$$(A_+^H A_+)^{-1} = (A^H A)^{-1} - \frac{(A^H A)^{-1} a_i^H a_i (A^H A)^{-1}}{1 + a_i (A^H A)^{-1} a_i^H} \quad (2.3.1)$$

Taking the trace of both sides gives

$$\text{tr}\{(A_+^H A_+)^{-1}\} = \text{tr}\{(A^H A)^{-1}\} - \frac{\text{tr}\{(A^H A)^{-1} a_i^H a_i (A^H A)^{-1}\}}{1 + a_i (A^H A)^{-1} a_i^H} \quad (2.3.2)$$

and using the property that  $\text{tr}\{CDE\} = \text{tr}\{DEC\}$ , we obtain

$$\text{tr}\{(A_+^H A_+)^{-1}\} = \text{tr}(A^H A)^{-1} - \frac{a_i(A^H A)^{-2} a_i^H}{1 + a_i(A^H A)^{-1} a_i^H} \quad (2.3.3)$$

Therefore, the criterion is minimized at each step by selecting the row (observation) that maximizes the second term of (2.3.3).

### 2.3.2 Modified SFS algorithm

In this section, we derive an efficient SFS algorithm for the modified criterion.

**Lemma 2.3.1** [111] *Let  $R$  denote an invertible partitioned matrix,*

$$R = \begin{bmatrix} P & \vdots & Q \\ \dots & & \dots \\ S & \vdots & T \end{bmatrix} \quad (2.3.4)$$

where  $P$  and  $T$  are invertible. Then

$$R^{-1} = \begin{bmatrix} E^{-1} & \vdots & FH^{-1} \\ \dots & & \dots \\ H^{-1}G & \vdots & H^{-1} \end{bmatrix} \quad (2.3.5)$$

where

$$E = P - QT^{-1}S, \quad (2.3.6)$$

$$F = -P^{-1}Q \quad (2.3.7)$$

$$G = -SP^{-1} \quad (2.3.8)$$

and

$$H = T - SP^{-1}Q \quad (2.3.9)$$

The matrix  $E$  is called the Schur complement of  $P$ , and the matrix  $H$  is called the Schur complement of  $T$ .

**Lemma 2.3.2** [111] Let  $E$  denote the Schur complement of  $P$ ,

$$E = P - QT^{-1}S. \quad (2.3.10)$$

Then the inverse of  $E$  is

$$E^{-1} = P^{-1} + FH^{-1}G \quad (2.3.11)$$

Now denote  $A_+$  as the new matrix after the  $i$ th row  $a_i$  is added to matrix  $A$ . Then we have a partitioned expression of  $A_+A_+^H$ :

$$A_+A_+^H = \begin{bmatrix} AA^H & \vdots & Aa_i^H \\ \dots & & \dots \\ a_iA^H & \vdots & a_ia_i^H \end{bmatrix} \quad (2.3.12)$$

From (2.3.5), (2.3.9), and (2.3.11)

$$\begin{aligned} \text{tr} \{(A_+A_+^H)^{-1}\} &= \text{tr}(E^{-1}) + \text{tr}(H^{-1}) \\ &= \text{tr}(AA^H)^{-1} \\ &\quad + \frac{1 + a_iA^H(AA^H)^{-2}Aa_i^H}{a_ia_i^H - a_iA^H(AA^H)^{-1}Aa_i^H} \end{aligned} \quad (2.3.13)$$

Therefore, the criterion is minimized at each step by selecting the row that minimizes the second term in (2.3.13) [103].

## 2.4 Efficient Computation For SFS Algorithm

From (2.3.13), we know that we need to calculate  $a_i A^H (AA^H)^{-2} A a_i^H$  and  $a_i A^H (AA^H)^{-1} A a_i^H$  for every candidate row  $a_i$  to determine the best one among all the candidate rows. If we have many candidate rows, then the computational cost can be enormous. However, by making use of the previous calculations for the next choice, we can reduce the computational burden.

Let  $v_i = (AA^H)^{-1} A a_i^H$  and  $\sigma_i = a_i a_i^H - a_i A^H (AA^H)^{-1} A a_i^H$ . Then

$$(A_+ A_+^H)^{-1} = \begin{bmatrix} (AA^H)^{-1} + \frac{1}{\sigma_i} v_i v_i^H & \vdots & -\frac{1}{\sigma_i} v_i \\ \dots & & \dots \\ -\frac{1}{\sigma_i} v_i^H & \vdots & \frac{1}{\sigma_i} \end{bmatrix} \quad (2.4.1)$$

$$\begin{aligned} A_+^H (A_+ A_+^H)^{-1} A_+ &= A^H (AA^H)^{-1} A \\ &+ \frac{1}{\sigma_i} (A^H v_i v_i^H A - a_i^H v_i^H A - A^H v_i a_i + a_i^H a_i) \end{aligned} \quad (2.4.2)$$

Let  $u_i = A^H v_i$ . Then

$$a_j A_+^H (AA^H)^{-1} A_+ a_j^H = a_j A^H (AA^H)^{-1} A a_j^H + \frac{1}{\sigma_i} |a_j u_i - a_j a_i^H|^2 \quad (2.4.3)$$

$$(A_+ A_+^H)^{-2} = (A_+ A_+^H)^{-1} (A_+ A_+^H)^{-1}$$

$$= \begin{bmatrix} P & Q \\ S & T \end{bmatrix} \quad (2.4.4)$$

$$\begin{aligned} P &= (AA^H)^{-2} + \frac{1}{\sigma_i} v_i v_i^H (AA^H)^{-1} + \frac{1}{\sigma_i} (AA^H)^{-1} v_i v_i^H \\ &\quad + \frac{1}{\sigma_i^2} (v_i v_i^H)^2 + \frac{1}{\sigma_i^2} v_i v_i^H \end{aligned} \quad (2.4.5)$$

$$Q = -\frac{1}{\sigma_i} (AA^H)^{-1} v_i - \frac{1}{\sigma_i^2} v_i v_i^H v_i - \frac{1}{\sigma_i^2} v_i \quad (2.4.6)$$

$$S = -\frac{1}{\sigma_i} v_i^H (AA^H)^{-1} - \frac{1}{\sigma_i^2} v_i^H v_i v_i^H - \frac{1}{\sigma_i^2} v_i^H \quad (2.4.7)$$

$$T = \frac{1}{\sigma_i^2} v_i^H v_i + \frac{1}{\sigma_i^2} \quad (2.4.8)$$

Let  $z_i = (AA^H)^{-1} v_i$  and  $w_i = A^H z_i$ . Then

$$\begin{aligned} A_+^H (A_+ A_+^H)^{-2} A_+ &= A^H (AA^H)^{-2} A + \frac{1}{\sigma_i} (u_i w_i^H + w_i u_i^H) \\ &\quad - \frac{1}{\sigma_i} (a_i^H w_i^H + w_i a_i) \\ &\quad + \frac{1 + \|v_i\|^2}{\sigma_i^2} (u_i u_i^H - a_i^H u_i^H - u_i a_i + a_i^H a_i) \end{aligned} \quad (2.4.9)$$

$$\begin{aligned} a_j A_+^H (A_+ A_+^H)^{-2} A_+ a_j^H &= a_j A^H (AA^H)^{-2} A a_j^H \\ &\quad + \frac{2}{\sigma_i} [\operatorname{Re}((a_j w_i)(a_j u_i)^H) - \operatorname{Re}((a_j w_i)(a_j a_i^H)^H)] \\ &\quad + \frac{1 + \|v_i\|^2}{\sigma_i^2} |a_j u_i - a_j a_i^H|^2 \end{aligned} \quad (2.4.10)$$

Now, when we choose the best row from the remaining candidate rows to add to  $A_+$ , we can recursively update  $a_j A_+^H (A_+ A_+^H)^{-1} A_+ a_j^H$  and  $a_j A_+^H (A_+ A_+^H)^{-2} A_+ a_j^H$  for every candidate row  $a_j$  using (2.4.3) and (2.4.10). The initial values of these quantities can be shown to be zero. Once  $u_i$  and  $w_i$  have been computed, the update formulas in (2.4.3) and (2.4.10) only require vector inner products. The computational cost will be reduced greatly in this way.

To calculate  $u_i$  and  $w_i$ , we need to calculate  $v_i$  and  $z_i$  first. To calculate  $v_i = (AA^H)^{-1} A a_i^H$  and  $z_i = (AA^H)^{-1} v_i$ , we need to deal with  $(AA^H)^{-1}$ . However, in this problem,  $AA^H$  is huge and cannot be stored or inverted. Therefore, instead of finding the inverse matrix explicitly, we compute the solution by finding the minimizer of a quadratic function of the form:

$$\Phi(f) = \|g - Df\|^2 \quad (2.4.11)$$

where  $g$  is a known vector and  $D$  is a known matrix. We use the conjugate gradients method [112] which is defined as follows:

$$p_0 = r_0 = D^H g \quad (2.4.12)$$

$$f_0 = 0 \quad (2.4.13)$$

$$r_k = -\frac{1}{2} \nabla \Phi(f_k) = D^H (g - Df_k) \quad (2.4.14)$$

$$p_k = r_k + (||r_k||^2 / ||r_{k-1}||^2) p_{k-1} \quad (2.4.15)$$

$$f_{k+1} = f_k + \beta_k p_k \quad (2.4.16)$$

$$\beta_k = \frac{(p_k, r_k)}{\|Dp_k\|^2} \quad (2.4.17)$$

where  $p_k$  is called the direction vector, and  $\beta_k$  is chosen to minimize  $\Phi(f)$  in the  $p_k$  direction. Note that the conjugate gradients iteration does not require the storage of  $D$  as long as the operation  $Dx$  can be performed on an arbitrary vector  $x$  in some way other than by a matrix-vector multiply. In this setting,  $Dx$  can be computed using FFT's and other simple operations. Since  $f$  has finite dimensions, the minimum can be reached in finite steps. The vectors  $v_i$  and  $u_i$  will be the solutions corresponding to different definitions of  $g$  and  $D$ . Therefore, we can greatly reduce the computational time and storage space by using the conjugate gradients algorithm to solve the inversion problem instead of calculating the inverse directly.

## 2.5 Extending the SFS Process

When more samples than unknowns are desired, the selection can be continued with the standard SFS algorithm in Section 2.3.1 based on (2.2.2). For computational efficiency, we derive a recursive method for updating  $a_i(A^H A)^{-2}a_i^H$  and  $a_i(A^H A)^{-1}a_i^H$ , which are needed to evaluate the second term in (2.3.3). For completeness, we reproduce the derivation in [100], along with our own extension that allows us to compute the initial values of the recursion. Using the Sherman-Morrison matrix inversion formula, we have the update formula for  $(A_+^H A_+)^{-1}$  as follows:

$$\begin{aligned} (A_+^H A_+)^{-1} &= (A^H A)^{-1} - \frac{(A^H A)^{-1} a_i^H a_i (A^H A)^{-1}}{1 + a_i (A^H A)^{-1} a_i^H} \\ &= (A^H A)^{-1} - \frac{1}{\sigma_i} g_i g_i^H \end{aligned} \quad (2.5.1)$$



where  $g_i = (A^H A)^{-1} a_i^H$ . Let  $h_i = (A^H A)^{-1} g_i$ . Then

$$(A_+^H A_+)^{-2} = (A^H A)^{-2} - \frac{1}{\sigma_i} g_i h_i^H - \frac{1}{\sigma_i} h_i g_i^H + \frac{1}{\sigma_i^2} (g_i g_i^H)^2 \quad (2.5.2)$$

$$a_j (A_+^H A_+)^{-1} a_j^H = a_j (A^H A)^{-1} a_j^H - \frac{1}{\sigma_i} |a_j g_i|^2 \quad (2.5.3)$$

$$a_j (A_+^H A_+)^{-2} a_j^H = a_j (A^H A)^{-2} a_j^H - \frac{2}{\sigma_i} \text{Re}(a_j g_i (a_j h_i)^H) + \frac{\|g_i\|^2}{\sigma_i^2} |a_j g_i|^2 \quad (2.5.4)$$

Now we need to find the initial value of  $a_i (A^H A)^{-2} a_i^H$  and  $a_i (A^H A)^{-1} a_i^H$ . When  $A$  is square (the initial  $A$  for the extended SFS algorithm), we have the following relations after some matrix manipulation:

$$a_j (A^H A)^{-1} a_j^H = a_j A^H (A A^H)^{-2} A a_j^H \quad (2.5.5)$$

$$a_j (A^H A)^{-2} a_j^H = a_j A^H (A A^H)^{-3} A a_j^H \quad (2.5.6)$$

The term  $a_j A^H (A A^H)^{-2} A a_j^H$  is already available from the initial SFS process from (2.4.10). We also need an efficient recursive formula to update  $a_j A^H (A A^H)^{-3} A a_j^H$ . Let  $c_i = (A A^H)^{-1} z_i$  and  $d_i = A^H c_i$ . Using (2.4.1) and (2.4.4), after some matrix manipulation we have

$$\begin{aligned} (A_+ A_+^H)^{-3} &= (A_+ A_+^H)^{-2} (A_+ A_+^H)^{-1} \\ &= \begin{bmatrix} E & F \\ G & H \end{bmatrix} \end{aligned} \quad (2.5.7)$$

where

$$\begin{aligned}
E &= (AA^H)^{-3} + \frac{1}{\sigma_i}(v_i c_i^H + c_i v_i^H) \\
&\quad + \frac{1}{\sigma_i} z_i z_i^H + \frac{1 + \|v_i\|^2}{\sigma_i^2} (v_i z_i^H + z_i v_i^H) \\
&\quad + \frac{v_i^H z_i}{\sigma_i^2} v_i v_i^H + \frac{(1 + \|v_i\|^2)^2}{\sigma_i^3} v_i v_i^H
\end{aligned} \tag{2.5.8}$$

$$F = -\frac{1}{\sigma_i} c_i - \frac{v_i^H z_i}{\sigma_i^2} v_i - \frac{1 + \|v_i\|^2}{\sigma_i^2} z_i - \frac{(1 + \|v_i\|^2)^2}{\sigma_i^3} v_i \tag{2.5.9}$$

$$\begin{aligned}
G &= -\frac{1}{\sigma_i} c_i^H - \frac{v_i^H z_i}{\sigma_i^2} v_i^H \\
&\quad - \frac{1 + \|v_i\|^2}{\sigma_i^2} z_i^H - \frac{(1 + \|v_i\|^2)^2}{\sigma_i^3} v_i^H
\end{aligned} \tag{2.5.10}$$

$$H = \frac{1}{\sigma_i^2} v_i^H z_i + \frac{(1 + \|v_i\|^2)^2}{\sigma_i^3} \tag{2.5.11}$$

$$\begin{aligned}
&A_+^H (A_+ A_+^H)^{-3} A_+ \\
&= A^H (AA^H)^{-3} A + \frac{1}{\sigma_i} w_i w_i^H + \frac{1}{\sigma_i} (u_i d_i^H + d_i u_i^H - a_i^H d_i^H - d_i a_i) \\
&\quad + \frac{1 + \|v_i\|^2}{\sigma_i^2} (u_i w_i^H + w_i u_i^H - a_i^H w_i^H - w_i a_i) \\
&\quad + \left( \frac{v_i^H z_i}{\sigma_i^2} + \frac{(1 + \|v_i\|^2)^2}{\sigma_i^3} \right) (u_i u_i^H - a_i^H u_i^H - u_i a_i + a_i^H a_i)
\end{aligned} \tag{2.5.12}$$

$$\begin{aligned}
& a_j A_+^H (A_+ A_+^H)^{-3} A_+ a_j^H \\
&= a_j A^H (A A^H)^{-3} A a_j^H + \frac{1}{\sigma_i} |a_j w_i|^2 + \frac{2}{\sigma_i} (\operatorname{Re}((a_j d_i)(a_j u_i)^H) - \operatorname{Re}((a_j d_i)(a_j a_i^H)^H)) \\
&\quad + \frac{2(1 + \|v_i\|^2)}{\sigma_i^2} (\operatorname{Re}((a_j w_i)(a_j u_i)^H) - \operatorname{Re}((a_j w_i)(a_j a_i^H)^H)) \\
&\quad + \left( \frac{v_i^H z_i}{\sigma_i^2} + \frac{(1 + \|v_i\|^2)^2}{\sigma_i^3} \right) |a_j u_i - a_j a_i^H|^2 \tag{2.5.13}
\end{aligned}$$

Now, we can use this recursive formula to update  $a_j A_+^H (A_+ A_+^H)^{-3} A_+ a_j^H$  until we have the same number of samples as unknowns. Then we use this value as the initial value of  $a_j (A^H A)^{-2} a_j$  to begin the recursion for the extended SFS algorithm.

## 2.6 Experiments

To demonstrate the value of our method, we applied it to an actual MR data set. Figure 2.1(a) shows a  $128 \times 128$  MR scout image (courtesy of the Center for Nuclear Imaging Research, University of Alabama at Birmingham) reconstructed from the full  $128 \times 128$  k-space sample set. The k-space samples of the scout image are considered to be the full image data set for selection purposes. This data set was a rapidly acquired scout image, which contains some significant artifacts outside the ROS. The presence of these artifacts tests the ability of the algorithm to provide a good selection and reconstruction in spite of violating the assumptions of the ROS.

Figure 2.1(b) shows the ROS identified by hand. It contains 5168 possibly nonzero voxels. Using this ROS, the k-space data were selected optimally by the proposed algorithm. Since the initial criterion with a single selected sample in the frequency domain

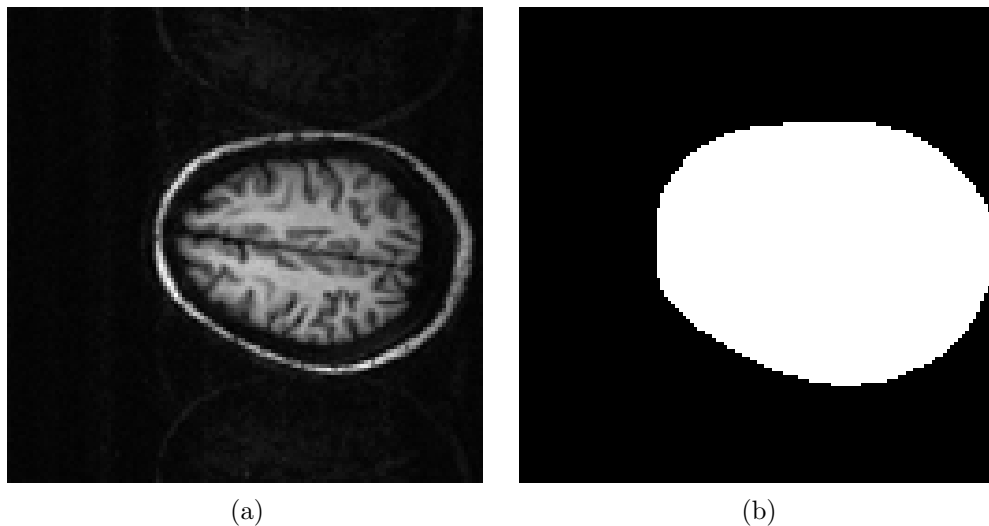


Figure 2.1: (a) The real image, (b) The ROS image (white indicates the support region)

is the same regardless of the sample, we arbitrarily choose the DC sample as the initial point for the recursive method. We have shown in the appendix that any circular shift of the selection pattern in  $k$ -space yields the same criterion value. Therefore, a shift of the initial point only causes a circular shift of the resulting optimal selection, which is also optimal. To illustrate how the criterion changes as more samples are selected, we continued the SFS process until all 16,384  $k$ -space samples were selected. First, we chose 5168  $k$ -space samples (matching the number of points in the ROS) from 16,384 candidate points with the modified algorithm in Section 2.4. Then we switched to the algorithm in Section 2.5 to continue the SFS process.

The criterion curve for the whole selection process is shown in Figure 2.2(a). When matrix  $A$  is underdetermined, the criterion increases with each selected sample and reaches a maximum value when  $A$  is square. This is because the pseudo-inverse solution

reduces the degrees of freedom for the noise, and the corresponding error resulting from zeroing out some signal components is not included in the criterion. Equation (2.2.7) shows that the MSE criterion for the minimum-norm least-squares solution includes two terms when  $A$  is underdetermined — one term represents the error due to the missing signal components and the other representing the error due to observation noise. As more samples are selected, the error from missing signal components decreases. When the number of observations equals the number of unknowns, this term disappears entirely. Since we know we will select the minimum density so that no signal components are missed, we ignore this term in our modified criterion and only keep the noise term that reflects the noise amplification level during the selection process. For each row of  $A$  that is added, the number of degrees of freedom for noise increases by one, causing the criterion to increase until  $A$  becomes square. Since the criterion only represents the noise portion of the error and the missing signal portion is unknown, we must select rows for  $A$  until the unknown signal error disappears — that is, when  $A$  becomes square. Thereafter, the criterion decreases with each selected sample because the average noise will decrease when more samples are observed while the number of the unknowns is fixed. The flop curve in Figure 2.2 (b) shows the relation of the criterion to the condition number indirectly, which has the same shape as the criterion curve. The average number of flops for the whole selection process is  $2.1759 \times 10^8$ . The average number of flops is  $3.086 \times 10^8$  before the minimum density and  $1.7566 \times 10^8$  after it.

An interesting result can be observed from the criterion curve. The curve drops sharply right after the maximum value and then becomes smooth. Therefore, the reconstructed image will improve greatly if we select only a few more samples than the number

Table 2.1: Comparison of the criterion and time versus tol

# samples	tol=1e-5			tol=1e-3		
	5168	5297	16384	5168	5297	16384
MSE	10.8543	2.3362	0.3153	10.8542	2.3421	-0.3816
time(hr)	18	22	41	12	15	30

of unknowns. After this, selecting more samples yields diminishing returns in terms of image quality improvement as a function of additional acquisition time. In Table 2.1, we see that the criterion value is 10.8542 when the selected number equals the number of the unknowns in the ROS (5168). Then with only 129 more samples selected, the criterion drops drastically from 10.8542 to 2.3362; i.e, the net drop is 8.52. However, with 11216 more samples selected, the criterion decreases only by 2. Image quality improvement is purely a function of the noise level decrement in the reconstructed image. There is no direct relation of the quality criterion to the spatial resolution since the spatial resolution in the reconstruction is fixed; However, the samples optimized with the proposed criterion covers the whole k-space nonuniformly. With this approach, we achieve the same spatial resolution as that obtained with the full uniform k-space data.

The optimal sampling pattern with 5168 samples is shown in Figure 2.3(a) by the black dots . The image reconstructed from these 5168 k-space samples is shown in Figure 2.4(a). To demonstrate the improvement obtained by selecting a few more samples than the ROS, we reconstructed the image by selecting 129 more noisy samples than the ROS (5297 k-space points), where the criterion drops from 10.85 to 2.34. The corresponding sample pattern is shown in Figure 2.3(a) by 129 gray dots. The reconstructed image is shown in Figure 2.4(b). The difference image between the optimized image from

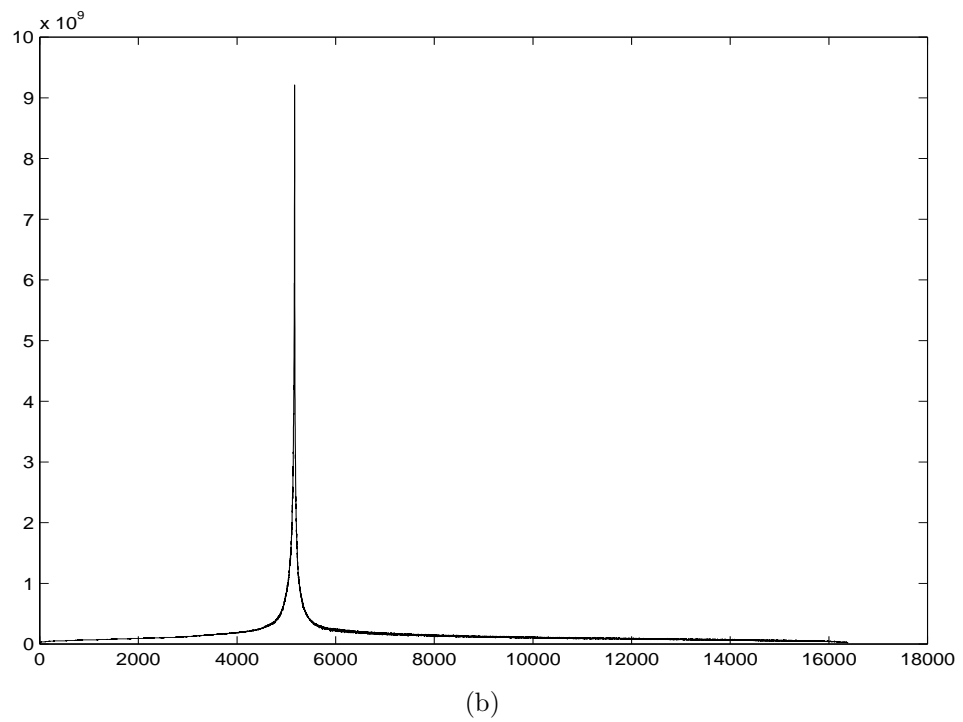
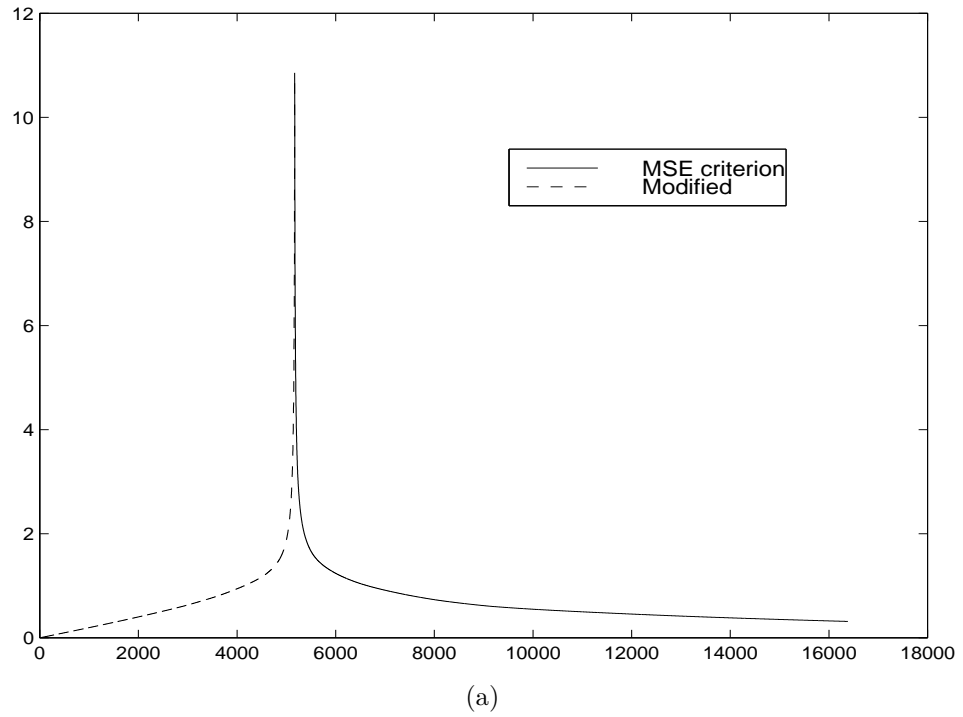


Figure 2.2: (a) The criterion curve versus the number of selected samples with the 128x128 ROS image, (b) The flop curve versus selection step with the 128x128 ROS .

5297 k-space samples and the original image is shown in Figure 2.3 (b). The artifacts outside the ROS are the systematic difference between them. When k-space samples are acquired independently as in MRSI, the noise variance at each k-space location is the same. However, our data set was acquired by a rapid scan through k-space in which the samples are not acquired independently. In addition, the artifacts outside the ROS are low-frequency noise, which is not considered in the model. Thus, the noise is larger at the lowest, most powerful frequencies in the acquisition process. Therefore, once we found the optimal sample distribution, we circularly shifted it so that DC and a few other adjacent frequencies were unselected. Since according to the theorem in the appendix the criterion is invariant to periodic shifts of the selection, this step will have no negative effects on reconstruction quality.

The discrete impulse response for the optimized set is an impulse for every location in the ROS. The impulse response from the optimized k-space data is shown in Figure 2.5(a). That explains why we can reconstruct the image exactly at the minimum density if there is no noise outside the ROS. For comparison purposes, we also used 5297 low-frequency noisy samples in a circle around DC to reconstruct the image from a zero-padded FFT and a least-squares method. The impulse response from the inverse FFT of the lowpass filter is shown in Figure 2.5(b). Only about 1/3 of the energy is concentrated on the center point with 2/3 of the energy spread out to form a lowpass impulse response. The lowpass image from a zero padded FFT has about half the resolution of the optimized image. There are obvious rings in the reconstructed image from a zero-padded FFT as expected. Therefore, the zero-padded FFT reconstruction of the image is not included here. Instead, iterative reconstructions of the lowpass image at 3 different



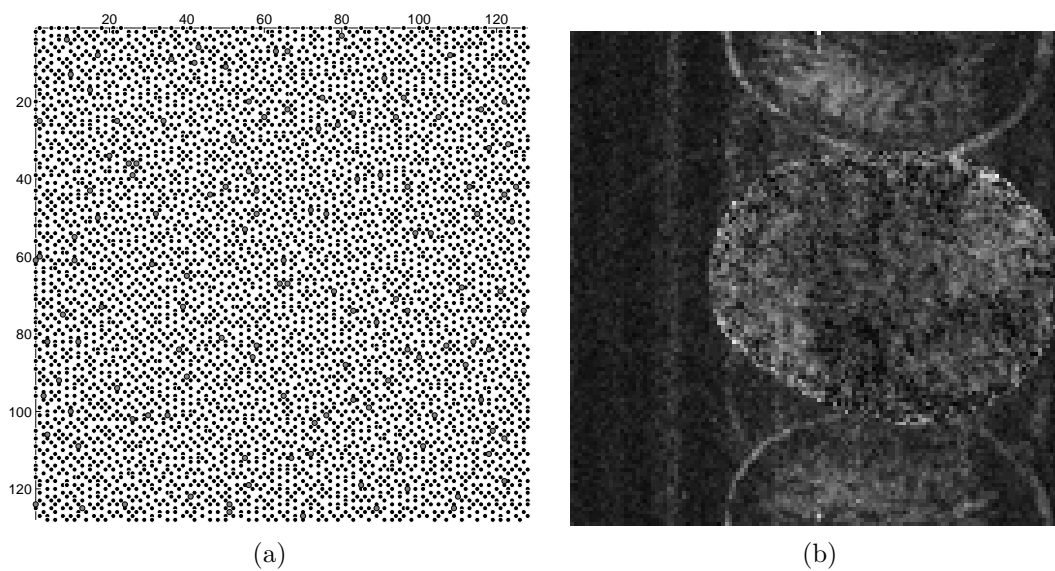


Figure 2.3: (a) 5297 optimized k-space sample distribution (the 5168 black dots represent the optimized minimum density, larger gray dots indicates 129 more optimized samples than the minimum density), (b) Absolute difference between the optimized image reconstruction and the fully sampled  $128 \times 128$  image. (Dynamic range is scaled by a factor of 5 for greater visibility).

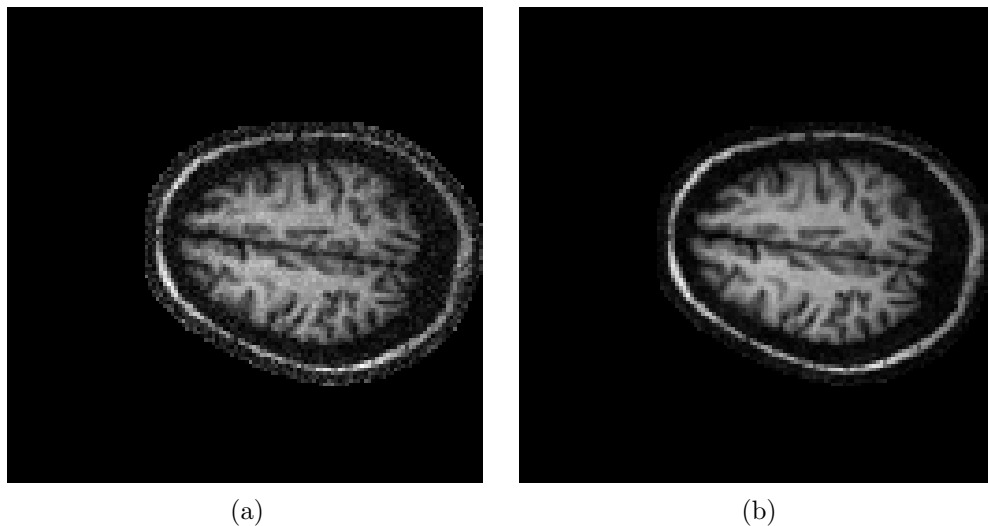


Figure 2.4: (a) The image from the minimum density k-space data(5168 points). (b) The image from 5297 k-space samples (the ROS has been imposed as a constraint in the reconstruction).

iterations are shown in Figure 2.6. Figure 2.6(a) shows the reconstructed image from an inverse FFT of 5297 lowpass samples. Figure 2.6(b) shows the reconstructed images from a least-squares solution at iteration 5. Figure 2.6(c) shows the reconstructed images from a least-squares solution at iteration 20. Figure 2.6(d) shows the reconstructed images from a least-squares solution at iteration 100. The resulting system is extremely ill-conditioned and gets progressively worse as the iterations continue.

The tolerance for ending the conjugate gradients algorithm has some effect on the accuracy of the computational criterion and the computational time which is shown in Table 2.1. Here, we define the tolerance as the gradient vector norm of a quadratic function that needs to be minimized. The function reaches the minimum when the gradient vector norm equals zero. In theory, the MSE with all 16,384 points observed is

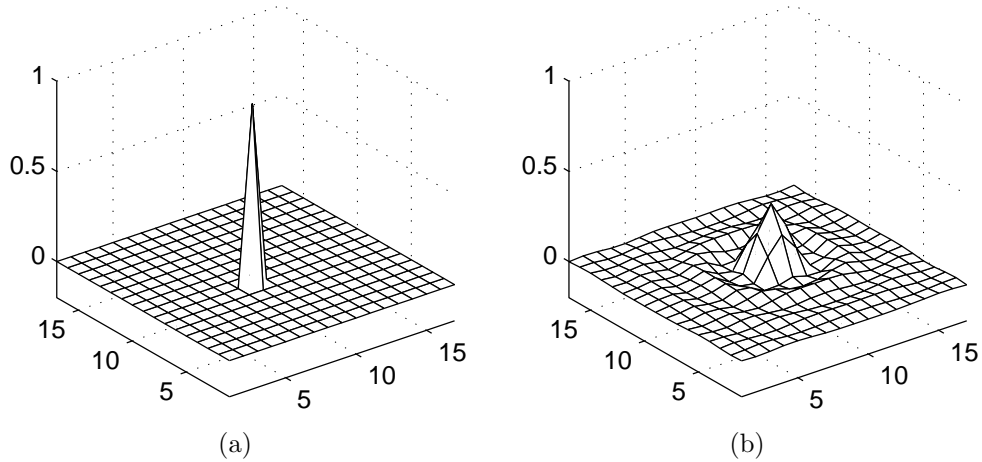


Figure 2.5: (a) The point spread function from optimized k-space data (b) The point spread function from inverse FFT.

0.3154. When  $tol = 10^{-5}$ , the final computational criterion is 0.3153, almost the same as the theoretical value. When  $tol = 10^{-3}$ , there is an obvious accumulating computational error to the criterion when a huge number (16384) of samples is selected as shown in Table 2.1, and the sample selection pattern is a little different from that for  $tol = 10^{-5}$ . When the selection number is not quite as large, (5297 in Table 2.1 and 4096 or 2304 in Table 2.2), the accumulating error is acceptable. To finish the whole process takes 30 hours when  $tol = 10^{-3}$  and 41 hours when  $tol = 10^{-5}$  (running on a 250MHz Sun Ultra Sparc processor). The smaller the FOV is, the faster the selection process will be. Here, we chose to use  $tol = 10^{-5}$  to assure reliability of the results.

To evaluate the method for MRSI, we applied the method to an actual 1H MRSI data set. Figure 2.7(a) and (b) shows the water and fat image from a full  $64 \times 64$  real k-space MRSI data set (courtesy of the Center for Nuclear Imaging Research, University of Alabama at Birmingham) and the ROS identified by hand. It contains 1439 possibly

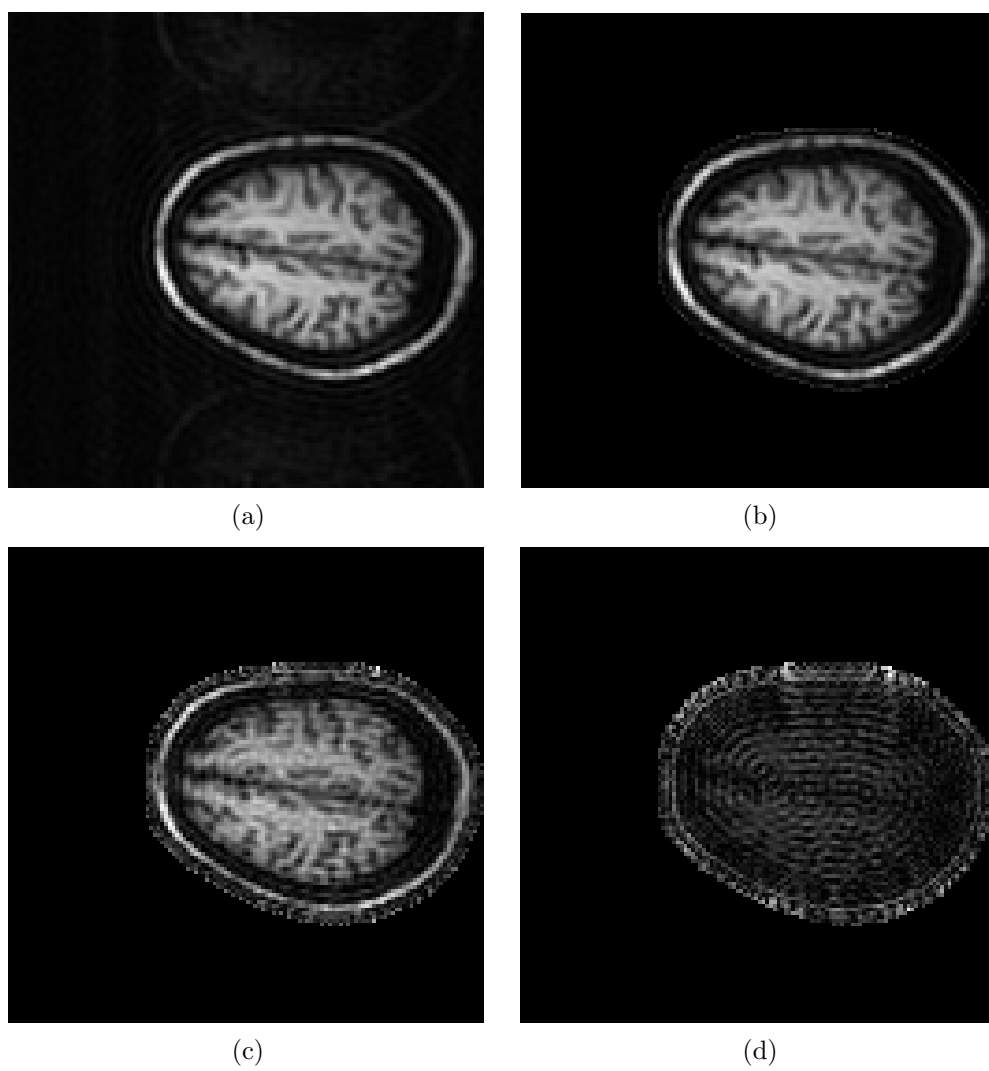


Figure 2.6: (a) Lowpass image from FFT, (b) Lowpass recursive solution at iteration 3, (c) Lowpass recursive solution at iteration 20, (d) Lowpass recursive solution at iteration 100.

Table 2.2: Comparison of the selection criterion and time versus FOV with MRSI ROS image

		64 × 64 FOV			48 × 48 FOV		
# samples		1439	1513	4096	1439	1513	2304
tol=	MSE	6.4186	1.8906	0.3513	8.4318	2.2886	0.6245
1e-5	time(hr)	1.13	1.39	2.47	0.77	0.92	1.15
tol=	MSE	6.1709	1.9027	0.3184	8.4318	2.2887	0.6440
1e-3	time(hr)	0.72	0.9	1.64	0.497	0.598	0.757

nonzero voxels. Using this ROS, the k-space data were selected optimally by the proposed algorithm. Figure 2.7(c) shows the ROS identified by hand. Using this ROS, the k-space data were selected optimally by the proposed algorithm. To illustrate how the criterion changes as more samples are selected, we continued the SFS process until all 4096 k-space samples were selected. First, we chose 1439 k-space samples (matching the number of points in the ROS) from 4096 candidate points with the modified algorithm in Section 2.4. Then we switched to the algorithm in Section 2.5 to continue the SFS process. To compare the results with a reduced FOV, we applied the proposed method and the traditional lowpass method to a reduced 48 × 48 FOV. Figure 2.7 (d) shows the 48 × 48 ROS image extracted from the 64 × 64 ROS image. Figure 2.7 (e) shows the 48 × 48 water image extracted from the 64 × 64 real image. Figure 2.7 (f) shows the 48 × 48 fat image extracted from the 64 × 64 real image. The results are summarized in Table 2.2.

The set of 1513 optimized k-space samples with the 64 × 64 FOV is plotted in Figure 2.8(a). Figure 2.8(b) shows the 1513 optimized k-space data set distribution with the 48 × 48 FOV. The 1439 black dots represent the optimized minimum density sampling. The larger gray dots represent an additional 74 optimized samples to reduce the noise. Both distributions cover all of k-space with the larger interval in the 48 × 48 case.

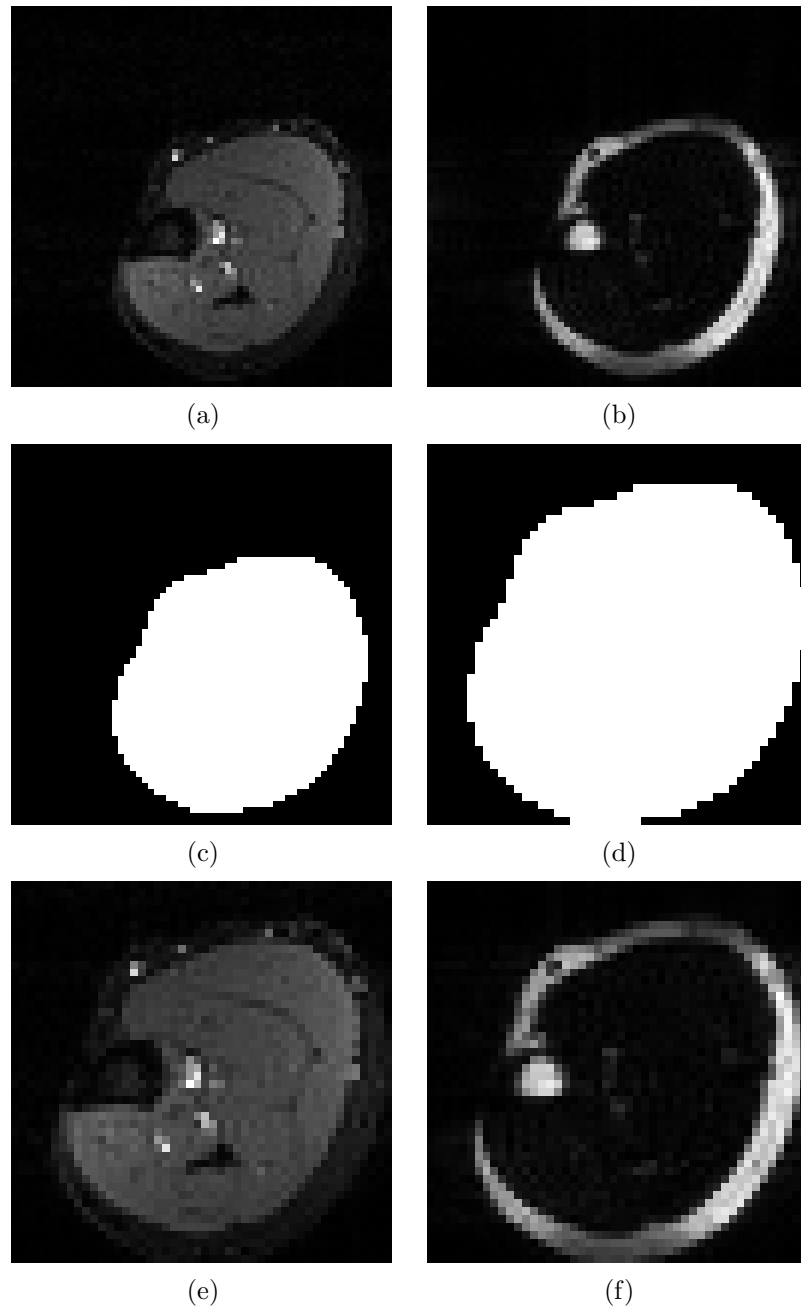


Figure 2.7: (a) Water image from the full  $64 \times 64$  real MRSI data, (b) Fat image from the full  $64 \times 64$  real MRSI data, (c) The  $64 \times 64$  ROS image (white indicates the support region), (d)  $48 \times 48$  ROS image extracted from the  $64 \times 64$  ROS (white indicates the support region), (e)  $48 \times 48$  water image extracted from the  $64 \times 64$  real water image, (f)  $48 \times 48$  fat image extracted from the  $64 \times 64$  real fat image.

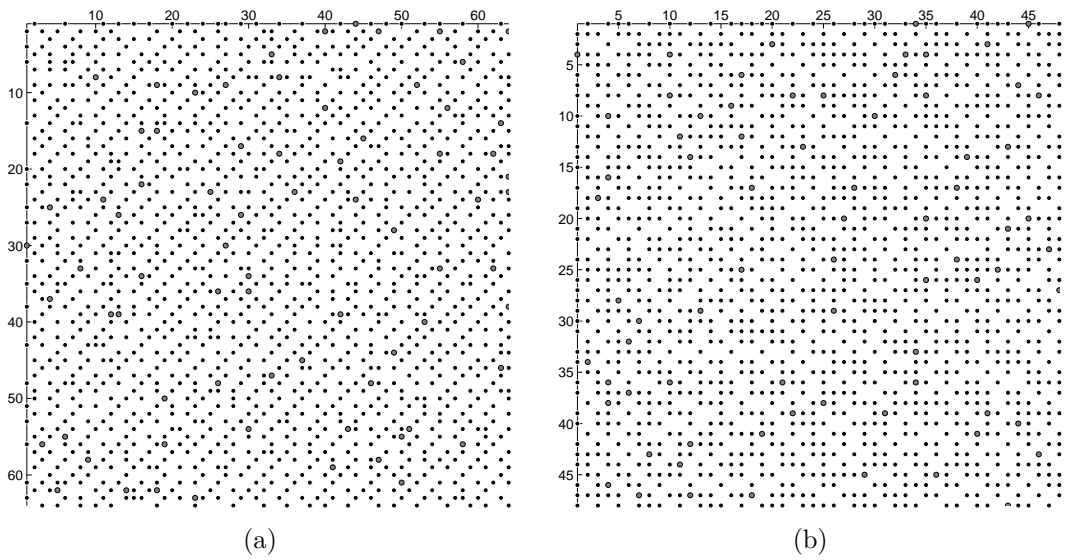


Figure 2.8: (a) 1513 optimized k-space data distribution with  $64 \times 64$  FOV (the minimum optimized 1439 points indicated by black dots, larger gray dots indicate 74 more samples than the minimum density), (b) 1513 optimized k-space samples with a reduced  $48 \times 48$  FOV (the minimum optimized 1439 points indicated by black dots, larger gray dots indicate 74 more samples than the minimum density).

The noise criterion curve versus the number of selected samples with the reduced  $48 \times 48$  ROS image is shown in Figure 2.9(a). The criterion value drops sharply right after the maximum value at the minimum density. From Table 2.2, we see that the selection time reduced greatly with smaller FOV, making it possible for real-time implementation. The flop curve is shown in Figure 2.9(b). The average number of flops per recursive step for the whole selection process is  $8.0730 \times 10^7$ . The average number of flops per recursive step is  $8.6022 \times 10^7$  before the minimum density and  $7.1926 \times 10^7$  after the minimum density.

The optimized PSF with a reduced  $48 \times 48$  FOV is shown in Figure 2.10(a), which is an impulse. The optimized PSF with the  $64 \times 64$  FOV is also an impulse (not include). The PSF for 1513 lowpass samples with the reduced  $48 \times 48$  FOV is shown in Figure 2.10(b). The PSF for 1513 lowpass samples with the  $64 \times 64$  FOV is shown in Figure 2.10(c). From Figure 2.10(b) and Figure 2.10(c), we see that the percent of the energy on the point is proportional to the percent of the lowpass area in the FOV for the lowpass PSF, while the width of the lowpass PSF is inversely proportional to the area of the lowpass region. However, with the circular or elliptical ROS, the lowpass image cannot reconstruct the image exactly.

The water and fat reconstruction images from 1513 optimized k-space samples with a  $64 \times 64$  FOV are shown in Figure 2.11 (a) and (b). The corresponding difference images between the optimal image and the original image are shown in Figure 2.12. The water and fat reconstruction images from 1513 optimized k-space samples with the reduced  $48 \times 48$  FOV are shown in Figure 2.13 (a) and (b). The corresponding difference images



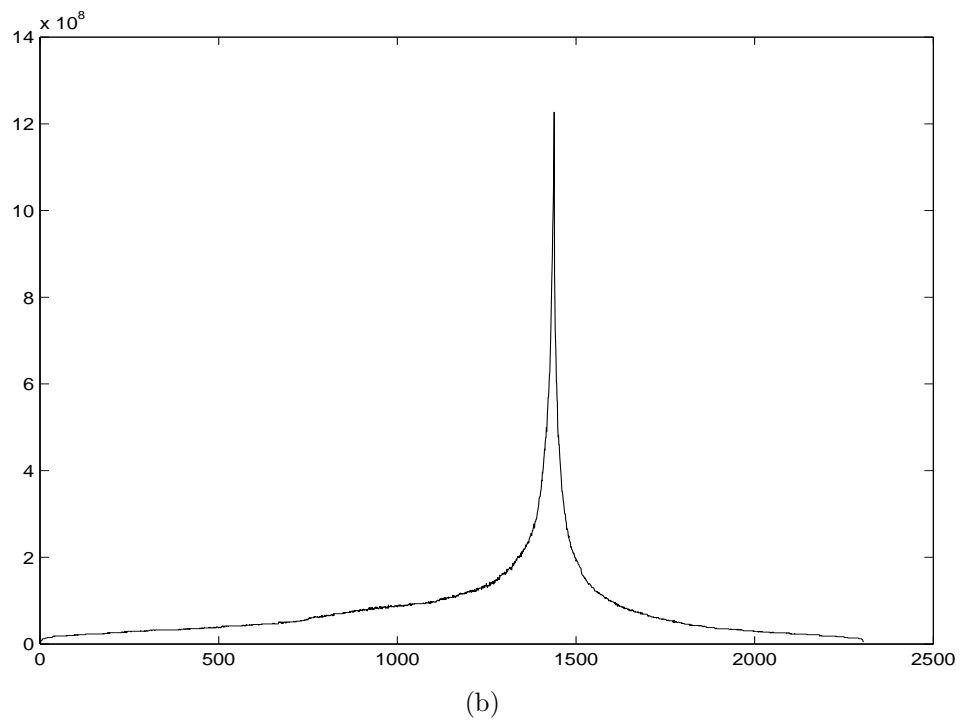
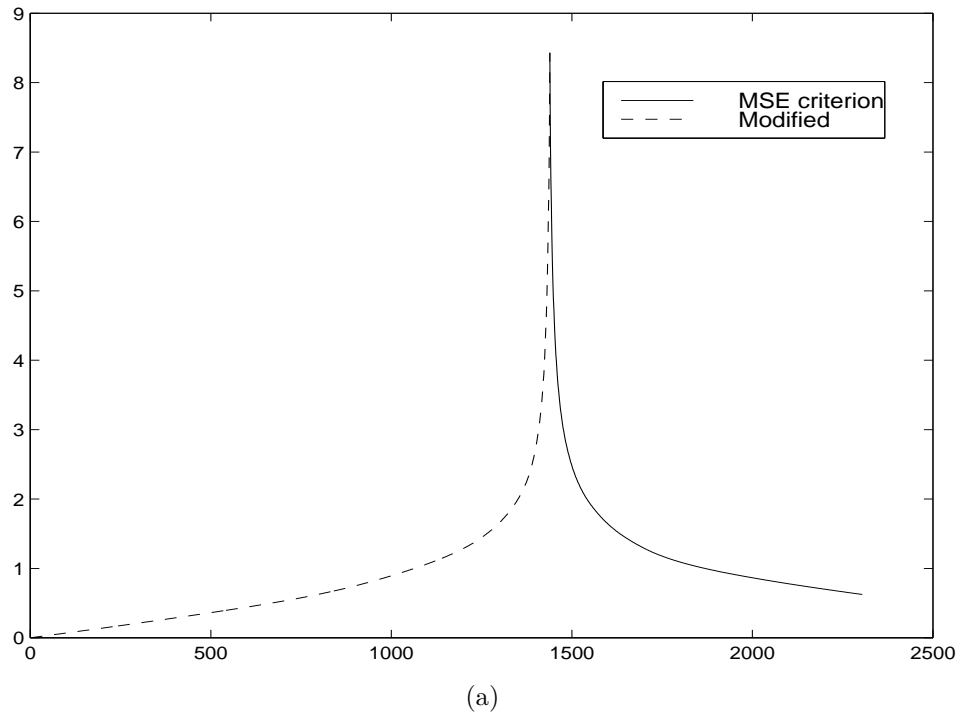


Figure 2.9: (a) Noise criterion curve versus the number of selected samples with the  $48 \times 48$  ROS, (b) Flops per selection step versus the number of selected samples with the  $48 \times 48$  ROS.

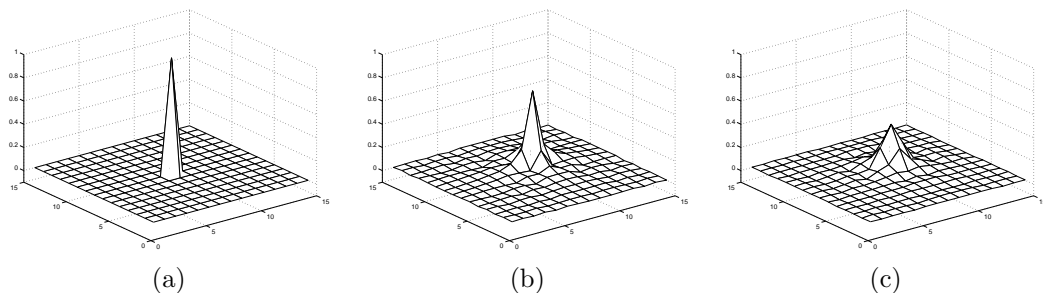


Figure 2.10: (a) Optimized PSF inside the ROS for a reduced  $48 \times 48$  FOV, (b) Lowpass PSF for  $48 \times 48$  FOV with 1513 lowpass k-space samples, (c) Lowpass PSF for  $64 \times 64$  FOV with 1513 lowpass k-space samples.

between the optimal image and the original image are shown in Figure 2.14. The lowpass water and fat image from 1513 k-space samples are shown in Figure 2.13 (c) and (d).

## 2.7 Discussion

The work presented here is important for optimizing MRSI data acquisition and can also be used for 3-D MRI. The new SFS algorithm presented in this paper has the following advantages: 1) it overcomes the limitation of the SFS algorithm based on the standard MSE criterion in that it can start with an empty initial matrix; 2) it drastically reduces storage space and computational time with the proposed SFS recursive algorithm and the conjugate gradients algorithm; 3) it is more applicable in practice than SBS in that the best sample can be observed as soon as it is selected, making possible real-time selection and acquisition. Simulation with real MR data shows a good-quality image can be reconstructed with only a few more samples than the minimum density by our method. Further work is clearly necessary to accelerate the algorithm if it is to be useful

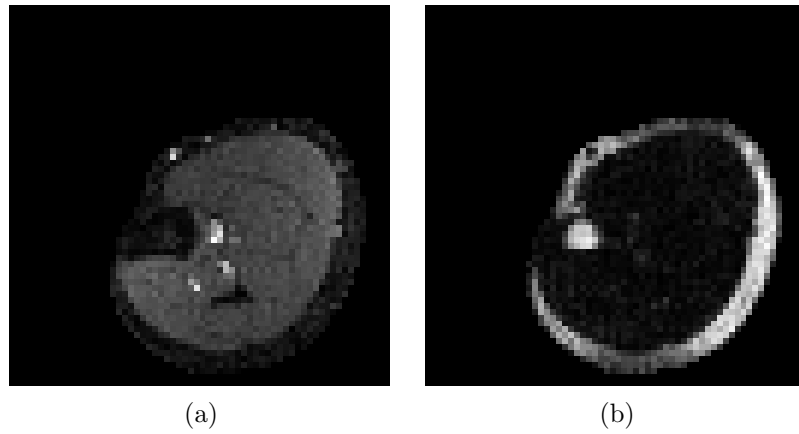


Figure 2.11: (a) Water image reconstructed from the 1513 optimized k-space samples with  $64 \times 64$  FOV with ROS constraint imposed, (b) Fat image reconstructed from the 1513 optimized k-space samples with  $64 \times 64$  FOV with ROS constraint imposed.

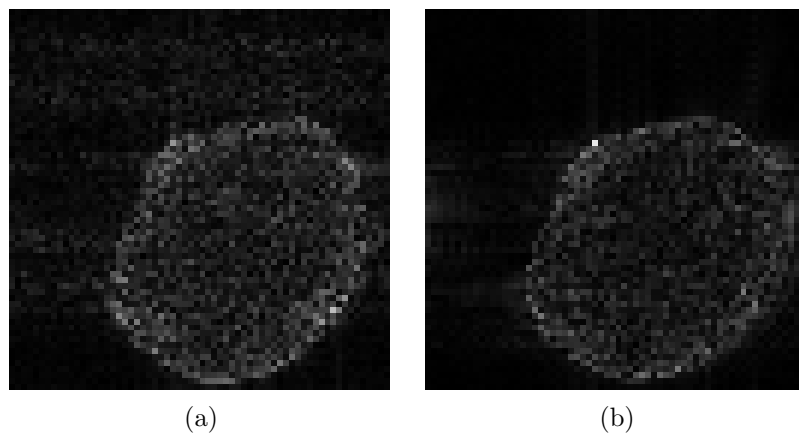


Figure 2.12: (a) Absolute difference between the optimized water image reconstruction and the fully sampled  $64 \times 64$  image (b) Absolute difference between the optimized fat image reconstruction and the fully sampled  $64 \times 64$  image. (Dynamic range is scaled by a factor of 5 for greater visibility).

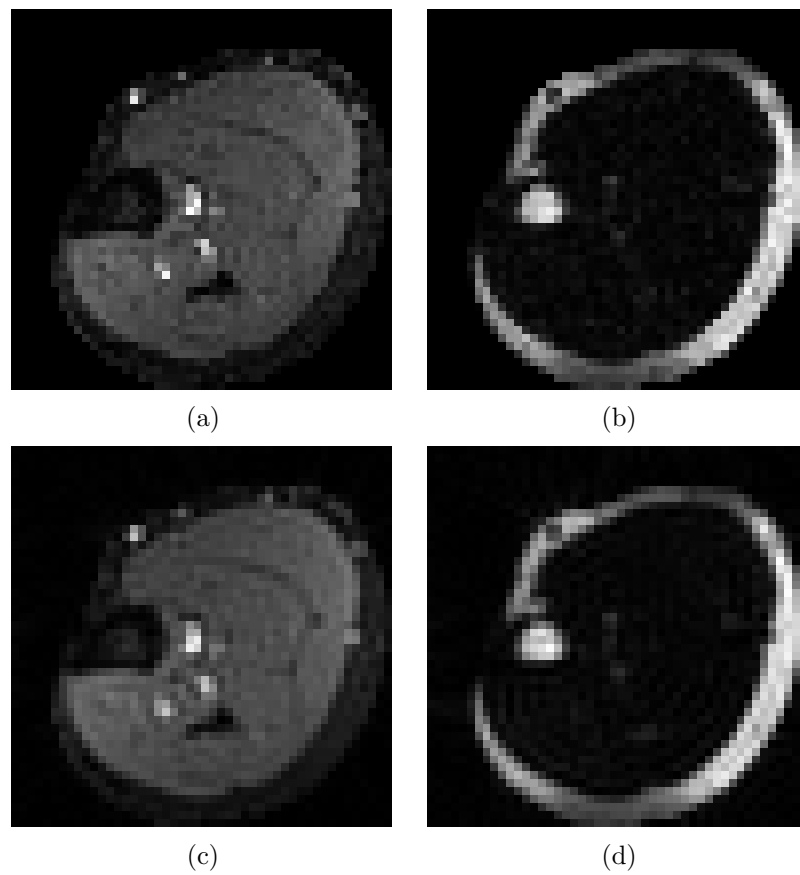


Figure 2.13:  $48 \times 48$  FOV reconstruction: (a) Water image reconstructed from the 1513 optimized k-space samples with ROS constraint imposed, (b) Fat image reconstructed from the 1513 optimized k-space samples with ROS constraint imposed, (c) Water image from the 1513 lowpass k-space samples, (d) Fat image from the 1513 lowpass k-space samples.

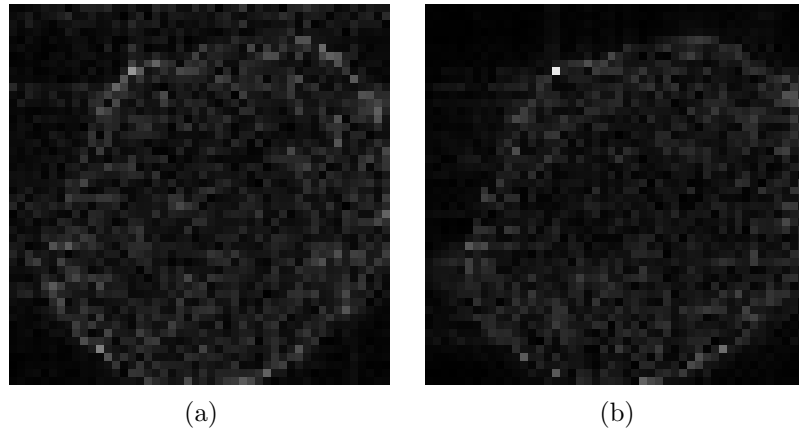


Figure 2.14: (a) Absolute difference between the optimized water image reconstruction and the  $48 \times 48$  extracted image, (b) Absolute difference between the optimized fat image reconstruction and the  $48 \times 48$  extracted image. (Dynamic range is scaled by a factor of 5 for greater visibility).

in a real-time context on an ordinary computer. However, the algorithm described here brings real-time implementation closer to reality.

## CHAPTER 3

### EFFICIENT BACKWARD SELECTION OF HEXAGONAL SAMPLES IN K-SPACE

#### 3.1 Introduction

Hexagonal sampling at the Nyquist rate has a 13.4% efficiency gain over rectangular sampling at the Nyquist rate for an elliptical ROS and yields the most densely packed spatial replications for space-limited signals [90,91]. However, Nyquist density sampling cannot reach the minimum density for an elliptical ROS image. Minimum density sampling yields samples linearly independent of each other, which can be reached through a nonuniform sampling strategy [101].

Reeves *et al.* proposed sequential backward selection (SBS) on a rectangular grid [98,99,103] based on minimizing mean squared error (MSE) in the reconstructed image. SBS begins with a full set of candidate samples and sequentially eliminates one sample at a time until the desired number remain. SBS represents a suboptimal approach to determine an optimized set of sample locations. However, SBS can guarantee a given level of performance before actually performing the optimization [100,113]. Furthermore, in extensive simulations we have found that SBS provides nearly optimal results in every case. By comparison, random or heuristic selection methods may yield wildly erratic results. To reduce selection time, we present sequential backward selection (SBS) on a hexagonal grid.

The motivation for using a hexagonal grid is that we can begin the elimination process with fewer candidate samples than in the rectangular case. Thus, we have fewer samples to eliminate to reach the desired number of remaining samples. It would be

possible simply to eliminate randomly some samples from a rectangular grid candidate set so that there are fewer samples to eliminate. However, there is no guarantee that this initial candidate set would be a good one from which to begin the backward selection process. Reeves and Zhao have shown that the upper bound on MSE of the final selection is proportional to the MSE resulting from the initial candidate set [100]. The initial candidate set defined by a hexagonal grid yields the lowest possible MSE for the same number of samples. Thus, the upper bound on the MSE of the final selection resulting from a hexagonal candidate grid is as low as possible when beginning with the same number of candidate samples. As such, it is an ideal starting point for the backward selection process.

Standard fast Fourier transform (FFT) algorithms cannot be used directly for non-rectangularly sampled data. To make use of the standard fast Fourier transform, we use a Smith normal form decomposition to transform the hexagonal DFT into a rectangular DFT. Since standard display devices require images to be displayed on a rectangular grid, the proposed algorithm yields an image sampled on a rectangular grid directly without interpolation by properly setting the periodic matrix in the frequency domain.

### 3.2 Selection algorithm

Sequential backward selection begins with a candidate matrix and sequentially eliminates the least important row at each step until the desired number of rows remain. Let  $a_i$  represent row  $i$  of  $A$ . If we eliminate  $a_i$  from  $A$ , the inverse matrix  $(\tilde{A}^H \tilde{A})^{-1}$  is given

by the Sherman-Morrison matrix inversion formula [110] as

$$(\tilde{A}^H \tilde{A})^{-1} = (A^H A)^{-1} - \frac{(A^H A)^{-1} a_i^H a_i (A^H A)^{-1}}{1 + a_i (A^H A)^{-1} a_i^H} \quad (3.2.1)$$

Taking the trace of both sides gives

$$\text{tr}\{(\tilde{A}^H \tilde{A})^{-1}\} = \text{tr}\{(A^H A)^{-1}\} + \frac{\text{tr}\{(A^H A)^{-1} a_i^H a_i (A^H A)^{-1}\}}{1 - a_i (A^H A)^{-1} a_i^H} \quad (3.2.2)$$

and using the property that  $\text{tr}\{CDE\} = \text{tr}\{DEC\}$ , we obtain

$$\text{tr}\{(\tilde{A}^H \tilde{A})^{-1}\} = \text{tr}(A^H A)^{-1} + \frac{a_i (A^H A)^{-2} a_i^H}{1 + a_i (A^H A)^{-1} a_i^H} \quad (3.2.3)$$

Therefore, the criterion is minimized at each step by selecting the row (observation) that minimizes the second term of (3.2.3). With this recursive formula, we need only evaluate  $a_i (A^H A)^{-1} a_i^H$  and  $a_i (A^H A)^{-2} a_i^H$  for all  $i$  to determine the row to be eliminated rather than computing the matrix inverse  $(A^H A)^{-1}$  with each row  $a_i$  in turn being eliminated.

We can follow a procedure similar to the one in [103] and described in Chapter 2 to recursively compute the quantities needed to evaluate the second term in (3.2.3). Let  $g_i = (A^H A)^{-1} a_i^H$ ,  $h_i = (A^H A)^{-1} g_i$ , and  $\sigma_i = 1 - a_i (A^H A)^{-1} a_i^H$ . To avoid storing a huge matrix, we compute  $g_i$  and  $h_i$  iteratively by minimizing  $\phi(v_i) = \|e_i - Av_i\|^2$  and  $\phi(w_i) = \|v_i - A^H Aw_i\|^2$  with the conjugate gradients method [114]. With these quantities in hand, we can efficiently compute

$$a_j (\tilde{A}^H \tilde{A})^{-1} a_j^H = a_j (A^H A)^{-1} a_j^H + \frac{1}{\sigma_i} |a_j g_i|^2 \quad (3.2.4)$$



$$a_j(\tilde{A}^H \tilde{A})^{-2} a_j^H = a_j(A^H A)^{-2} a_j^H + \frac{2}{\sigma_i} \text{Re}(a_j g_i (a_j h_i)^H) + \frac{|g_i|^2}{\sigma_i^2} |a_j g_i|^2 \quad (3.2.5)$$

Note that  $v_i$  and  $w_i$  only need to be computed for the row being eliminated in each elimination step, since every remaining row can be evaluated from the recursively computed terms in (3.2.4) and (3.2.5).

To use the recursion formulas, we must have initial conditions. Assume that  $A$  represents a Fourier transform matrix with columns removed corresponding to voxels outside the ROS. Let the image size be  $m$  and the ROS size be  $n$ .  $A^H A = mI$  because the columns of  $A$  are orthogonal to each other. Therefore, the initial value of  $a_j(A^H A)^{-1} a_j^H$  is  $n/m$  for all  $j$ . The initial value of  $a_j(A^H A)^{-2} a_j^H$  is  $n/m^2$  for all  $j$ . Since the criterion increment is the same for all  $j$ , we may arbitrarily choose any sample as the first to be eliminated.

### 3.3 Regular Hexagonal Sampling

All MR imaging methods use discrete data that has been sampled from an idealized continuous data function. The data sampling pattern determines the image replication pattern. If  $X_c(d)$  represent the continuous data function, the sampled data  $X$  at an integer sequence of points  $n$  may be expressed as

$$X(\mathbf{n}) = X_c(\mathbf{V}\mathbf{n}) \quad (3.3.1)$$

where  $V$  is the sampling matrix whose columns are the basis vectors of the sampling pattern [115]. The hexagonal sampling pattern is shown in Figure 3.1(b). The axis

direction is drawn in an orientation that conforms to an image matrix. For rectangular sampling,  $\mathbf{V}$  is a diagonal matrix. For hexagonal sampling,

$$\mathbf{V} = \begin{bmatrix} 2d_1 & -d_1 \\ 0 & d_2 \end{bmatrix} \quad (3.3.2)$$

where  $d_1 = d_2/\sqrt{3}$ . The sampling matrix is not unique for a given sampling pattern because different basis vectors can be chosen. The sampling matrix in (3.3.2) has the advantage of creating the rectangular image pixels directly from a discrete Fourier transform without interpolation. To keep pixels on a square array,  $d_2/d_1$  must be a rational fraction rather than the optimal value of  $\sqrt{3}$  [116]. Use of  $d_2/d_1 = 7/4$  yields a near-optimal efficiency gain of 12.5% compared to 13.4% for  $d_2/d_1 = \sqrt{3}$ . When sampling in the frequency domain, the reconstructed image from a discrete Fourier transform is replicated periodically in the spatial domain. The periodic matrix in the spatial domain is

$$\begin{aligned} \mathbf{N} &= 2\pi(\mathbf{V}^T)^{-1} \\ &= \begin{bmatrix} \frac{2\pi}{2d_1} & 0 \\ \frac{2\pi}{2d_2} & \frac{2\pi}{d_2} \end{bmatrix} \\ &= \begin{bmatrix} \frac{7}{8}M & 0 \\ \frac{M}{2} & M \end{bmatrix} \end{aligned} \quad (3.3.3)$$

where  $M \leq 2\pi/d_2$  is an integer divisible by 8 that represents the length of one side of the square image. On the other hand, discrete sampling of the image in the spatial domain causes periodic replication of the sample pattern in the frequency domain. The periodic

matrix in the frequency domain is

$$\mathbf{N}^T = \begin{bmatrix} \frac{7}{8}M & \frac{M}{2} \\ 0 & M \end{bmatrix} \quad (3.3.4)$$

It should be noted that the periodic matrix in (3.3.4) should be an integer matrix. It defines a rectangular replication pattern in the frequency domain, although its sampling pattern is hexagonal. The periodic matrix in (3.3.3) defines a hexagonal replication pattern in the spatial domain. Figure 3.1(a) shows as an example of the rectangular replication of the  $4 \times 6$  representative hexagonal samples within the region defined by the diamond symbols. It is known that a rectangular replication pattern in one domain corresponds to a rectangular sampling pattern in the transformed domain, and a hexagonal replication pattern in one domain corresponds to a hexagonal sampling pattern in the transformed domain regardless of the sampling pattern in the original space. Therefore, the periodic matrix in (3.3.4) defines image pixels on a rectangular grid in the spatial domain.

For the image to be exactly recoverable from the hexagonal sequence defined by (3.3.1), it must be space-limited with a hexagonal ROS as shown in Figure 3.1(b) with

$$d_1 < \frac{\pi}{b}, \quad d_2 < \frac{4\pi}{2a + c} \quad (3.3.5)$$

When  $a = c = \frac{2\pi}{\sqrt{3}}b$ , the ROS is a regular hexagon. However, the horizontal and vertical sampling interval are not the same even for a regular hexagon. Consider a space-limited waveform with a circular ROS. If  $b$  denotes the radius of this region, then for this waveform sampled rectangularly the maximum sampling periods are  $d_1 = \pi/b$ ,  $d_2 = \pi/b$ .

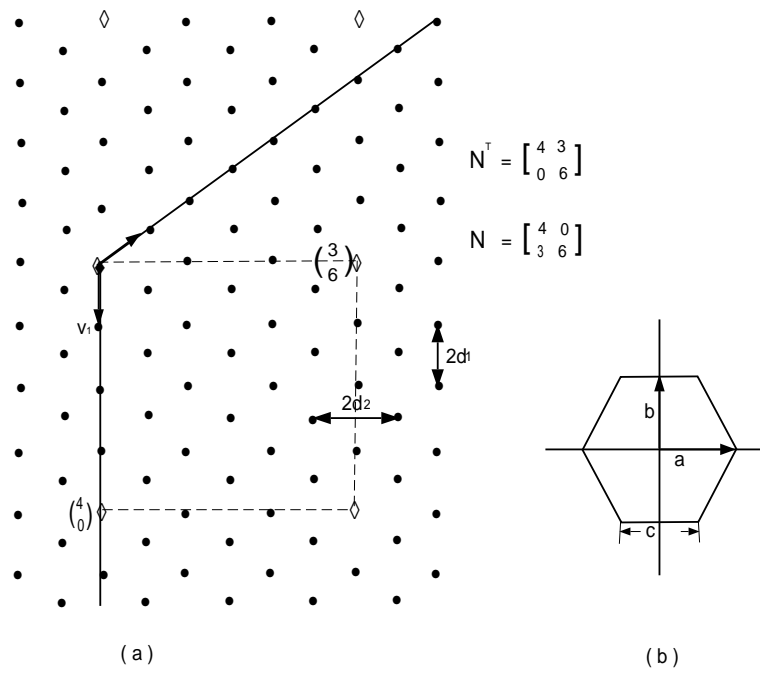


Figure 3.1: (a) Hexagonal sampling pattern, (b) Hexagon

For sampling this same waveform hexagonally we can choose  $d_1 = \pi/b$ ,  $d_2 = 2\pi/\sqrt{3}b$ . The mean sampling density is less for hexagonal sampling. In general, the mean sampling density is proportional to the area of the assumed ROS. For a circularly space-limited waveform, hexagonal sampling involves 13.4% fewer samples than rectangular sampling. If we use SBS beginning with a full hexagonal grid rather than a full rectangular grid, the selection time will be reduced because fewer samples must be eliminated. The resolution will not be reduced.

### 3.4 Generalized Multidimensional Discrete Fourier Transform

An FFT from a hexagonal grid is necessary both for the selection algorithm as well as for reconstruction once the samples are acquired. Many FFT algorithms have been developed for the evaluation of rectangular multidimensional DFTs (MDFTs). We present a procedure to make use of these algorithms for general MDFTs. A generalized MDFT pair is

$$x(\mathbf{n}) = \frac{1}{|\det \mathbf{N}|} \sum_{\mathbf{k}} X(\mathbf{k}) e^{j\mathbf{k}^T (2\pi \mathbf{N}^{-1}) \mathbf{n}} \quad (3.4.1)$$

$$X(\mathbf{k}) = \sum_{\mathbf{n}} x(\mathbf{n}) e^{-j\mathbf{k}^T (2\pi \mathbf{N}^{-1}) \mathbf{n}} \quad (3.4.2)$$

where  $\mathbf{N}$  is an integer periodic matrix in (3.3.3). By using the Smith form decomposition [117, 118],  $\mathbf{N}$  can be decomposed into

$$\mathbf{N} = \mathbf{U} \mathbf{D} \mathbf{V} \quad (3.4.3)$$

where  $\mathbf{U}$  and  $\mathbf{V}$  are unimodular integer matrices (determinant is  $\pm 1$ ) and  $\mathbf{D}$  is diagonal with  $|\det(\mathbf{D})| = |\det(\mathbf{N})|$ . To get desired Smith forms, two steps are performed. First, using elementary (regular unimodular) matrices, multiply the given integer matrix recursively on the left and right until the matrix is reduced to a diagonal form with the diagonal entry values in increasing order. Elementary row and column operations correspond to multiplication of the matrix on the left and right respectively by suitable unimodular matrices. Initially,  $\mathbf{U} = \mathbf{I}$ ,  $\mathbf{D} = \mathbf{N}$ , and  $\mathbf{V} = \mathbf{I}$ . The flowchart of the Smith form decomposition is shown in Figure 3.2. The diagonal matrix  $\mathbf{D}$  obtained in the first step may not be what we desire. However, we can impose structure on the available Smith forms by pivoting factors between diagonal elements of  $\mathbf{D}$  [119]. Specifically, matrix product  $\mathbf{PDS}$  can move an integer factor  $i$  from one diagonal entry to the other diagonal entry with  $\det(\mathbf{P}) = \pm 1$  and  $\det(\mathbf{S}) = \pm 1$ .

With Smith forms in (3.4.3), the MDFFT pair in (3.4.1) and (3.4.2) can be expressed as

$$\begin{aligned}
X(\mathbf{k}) &= \sum_{\mathbf{n}} x(\mathbf{n}) e^{-j\mathbf{k}^T (2\pi \mathbf{V}^{-1} \mathbf{D}^{-1} \mathbf{U}^{-1}) \mathbf{n}} \\
&= \sum_{\mathbf{n}} x(\mathbf{n}) e^{-j(\mathbf{V}^{-T} \mathbf{k})^T \mathbf{D}^{-1} (\mathbf{U}^{-1} \mathbf{n})} \\
&= \sum_{\hat{\mathbf{n}}} x(\mathbf{U} \hat{\mathbf{n}}) e^{-j\hat{\mathbf{k}}^T \mathbf{D}^{-1} \hat{\mathbf{n}}} \\
&= \hat{X}(\hat{\mathbf{k}}) \\
&= \hat{X}(\mathbf{V}^{-T} \mathbf{k})
\end{aligned} \tag{3.4.4}$$

$$x(\mathbf{n}) = \sum_{\mathbf{k}} X(\mathbf{k}) e^{j\mathbf{k}^T (2\pi \mathbf{V}^{-1} \mathbf{D}^{-1} \mathbf{U}^{-1}) \mathbf{n}}$$

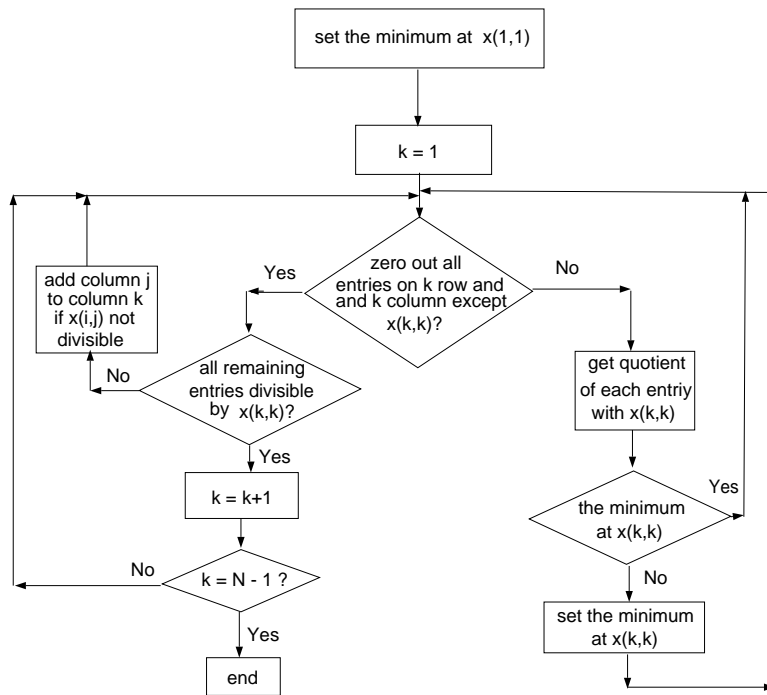


Figure 3.2: Smith form decomposition flowchart

$$\begin{aligned}
&= \sum_{\mathbf{k}} X(\mathbf{k}) e^{j(\mathbf{V}^{-T}\mathbf{k})^T \mathbf{D}^{-1}(\mathbf{U}^{-1}\mathbf{n})} \\
&= \sum_{\hat{\mathbf{k}}} X(\mathbf{V}^T \hat{\mathbf{k}}) e^{j\hat{\mathbf{k}}^T \mathbf{D}^{-1}\hat{\mathbf{n}}} \\
&= \hat{x}(\hat{\mathbf{n}}) \\
&= \hat{x}(\mathbf{U}^{-1}\mathbf{n}) \tag{3.4.5}
\end{aligned}$$

With (3.4.4) and (3.4.5), a matrix- $\mathbf{N}$  DFT becomes a matrix- $\mathbf{D}$  DFT. The general MDFT problem converts to a rectangular MDFT problem. The matrix- $\mathbf{N}$  MDFT algorithm involves three steps. First, scramble the input sequence  $x(\mathbf{n})$  according to the relation  $\mathbf{n} = (\mathbf{U}\hat{\mathbf{n}}) \bmod N$ . Second, compute a rectangular matrix- $\mathbf{D}$  DFT of the resulting sequence. Third, unscramble the output sequence  $X(\hat{\mathbf{k}})$  according to the relation  $\hat{\mathbf{k}} = (\mathbf{V}^{-T}\mathbf{k}) \bmod \mathbf{D}$ . The matrix- $\mathbf{N}$  inverse MDFT involves three similar steps.

### 3.5 Experiments

To demonstrate the value of our method, we applied it to an actual MR data set. Figure 3.3(a) shows a  $96 \times 96$  MR image from a  $128 \times 128$  rapidly acquired scout image (courtesy of the Center for Nuclear Imaging Research, University of Alabama at Birmingham) reconstructed from the full  $128 \times 128$  k-space sample set. Figure 3.3(b) shows a  $96 \times 96$  ROS identified from Figure 3.3(a). It contains 5168 possibly nonzero voxels. For the ROS in 3.3(b), the k-space data were selected by SBS from a  $96 \times 96$  rectangular k-space grid, which correspond to samples of the rectangular DFT coefficients of the image in Figure 3.3(a). Likewise, k-space samples were selected by SBS from an  $84 \times 96$  hexagonal k-space grid, which correspond to samples of the hexagonal DFT of the equivalent  $84 \times 96$  image.



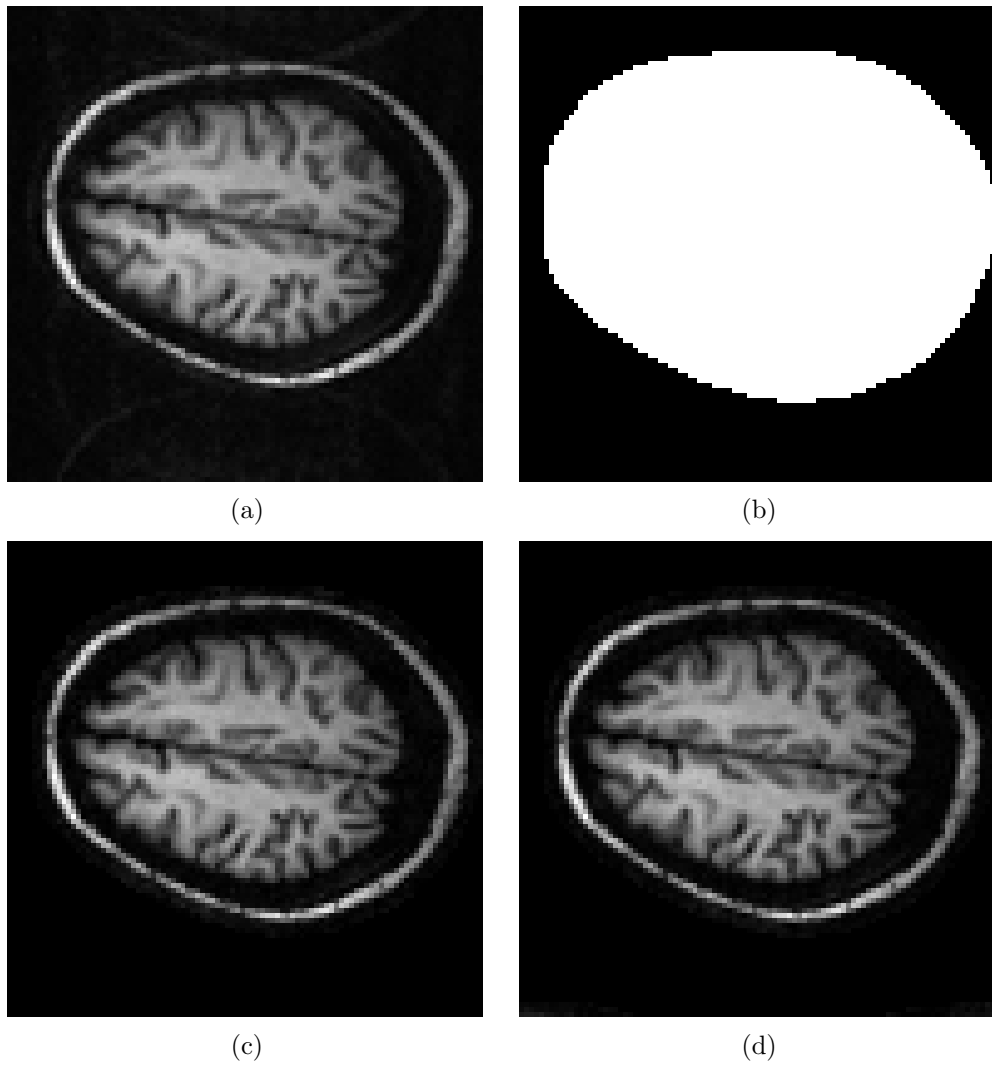


Figure 3.3: (a)  $96 \times 96$  image, (b)  $96 \times 96$  ROS, (c) Reconstructed image from 5550 rectangular k-space samples, (d) Reconstructed image from 5550 hexagonal k-space samples.

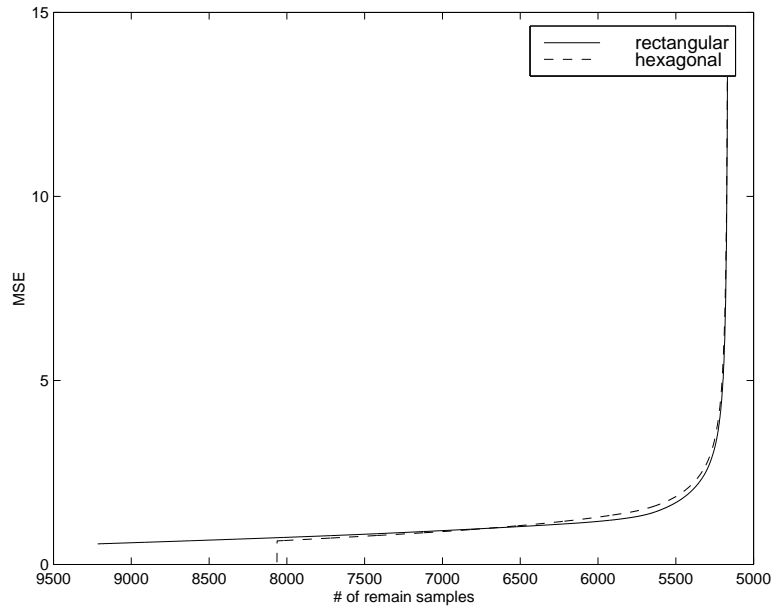


Figure 3.4: Criterion curves versus samples remaining.

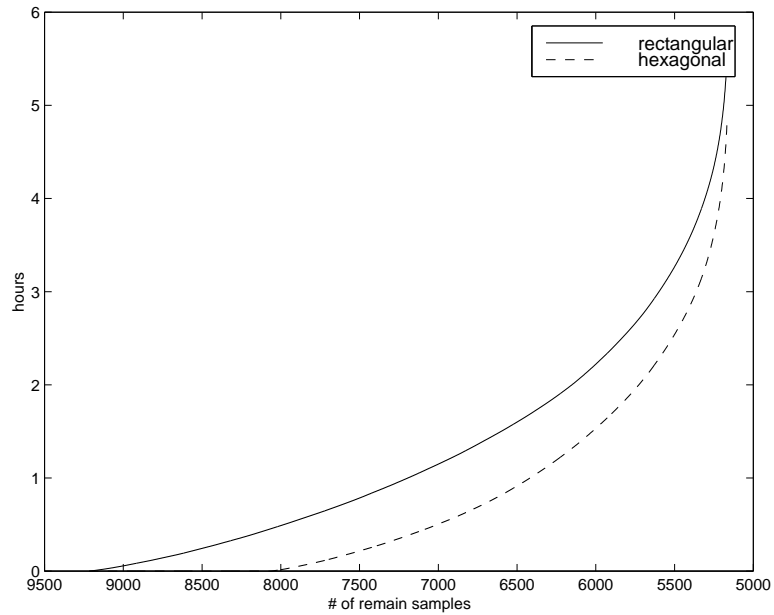


Figure 3.5: Time versus samples remaining.

Figure 3.4 shows the criterion comparison between SBS on a rectangular grid and SBS on a hexagonal grid. Figure 3.5 shows the selection time comparison between SBS on a rectangular grid and a hexagonal grid. We observed that when the selection approaches 5168 samples, the criterion curves and selection time curves increase sharply but increase very little when stopping with only a few more samples than 5168. The two criterion curves are very close throughout the process. However, the selection time for SBS from a hexagonal grid is always significantly less than that for SBS from a rectangular grid. When selecting more than 6500 samples, the selection time in the hexagonal case takes less than half of the selection time of the rectangular case. These observations tell us we can sample at a rate lower than the Nyquist rate on a hexagonal grid with minimal noise amplification as long as we acquire a few more samples than the number of nonzero pixels in the ROS. As a further comparison, we reconstructed the image from 5500 selected samples for both the rectangular and hexagonal cases. The reconstructions were done iteratively using a conjugate gradients algorithm. The results shown in Figure 3.3(c) and (d) demonstrate the good results that can be obtained with either selection method. Although there is no difference in resolution for the two cases and little difference in noise amplification, the selection time is much smaller for SBS on a hexagonal grid as shown in Figure 3.5.

### 3.6 Conclusion

We proposed a new method for reducing selection time for MRSI samples by applying SBS on a hexagonal grid rather than a rectangular grid. To make use of a standard

rectangular FFT, we computed a generalized MDFT based on a Smith form decomposition. To avoid interpolation artifacts, we chose an appropriate periodic matrix in the frequency domain such that we can compute rectangular-grid image pixels directly from hexagonal-grid frequency domain samples without interpolation. A lower than Nyquist rate on a hexagonal grid can be achieved with the proposed method. Furthermore, SBS on a hexagonal grid takes significantly less selection time than SBS on a rectangular grid.

## CHAPTER 4

### SEQUENTIAL BACKWARD ARRAY SELECTION

#### 4.1 Introduction

In this chapter, we develop an efficient algorithm for optimizing the dithering pattern so that the image can be reconstructed as reliably as possible from a periodic nonuniform set of samples, which can be obtained from a dithered rectangular-grid array. Taking into account the frequency support of the image, we sequentially eliminate the least informative array recursively until the minimal number of arrays remain. The advantage of the proposed algorithm is that convolution and downsampling take the place of operations involving a huge non-sparse matrix. Therefore, the proposed algorithm shows high efficiency in computational time and memory space. The resulting algorithm can be useful not only in magnetic resonance imaging but is also extremely important in some sensor array optimization problems, in digital reception of multiband signal transmissions, and in PMMW imaging [106, 107].

#### 4.2 The Mathematics of Sampling

Typical MRSI observations are laid out in a rectangular grid pattern as shown in Figure 4.1. The heavy dots represent the locations of the sensor elements in the unshifted sensor array. The light dots represent other locations to which the sensor array can be shifted. Assuming a circular ROS, if the radius of the ROS is  $R$  m, the Nyquist sample spacing in each dimension considered individually is  $\frac{\pi}{R}$ . This is the maximum uniform rectangular sample spacing that avoids aliasing. However, it is well

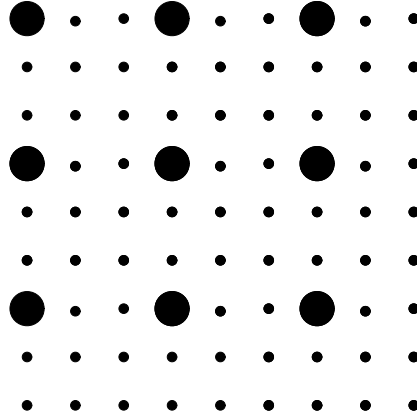


Figure 4.1: typical sampling pattern.

known that a circularly bandlimited image can be sampled uniformly on a hexagonal grid with a 13.4% lower sampling density without aliasing [90,91], where  $\Delta x = 2\pi/\sqrt{3}R$  and  $\Delta y = \pi/R$ . (See Figure 4.2.)

In fact, if we allow nonuniform sampling we can reduce the average sampling density even further [101]. In particular, we can sample an image using a periodic replication of a nonperiodic sampling pattern to capture the information in a bandlimited image without aliasing. An example of this kind of sampling pattern is shown in Figure 4.3. In this example, each  $3 \times 3$  block sampling pattern is periodically replicated over the frequency image plane. This pattern results from shifting the array in Figure 4.1 according to each offset sample in one of the  $3 \times 3$  blocks.

If we represent the discretized frequency image as a vector  $y$ , the unknown discretized spatial support by a vector  $x$ , and the mapping from the spatial-domain samples to the frequency-domain image by  $F$ , the fully sampled frequency image can be expressed

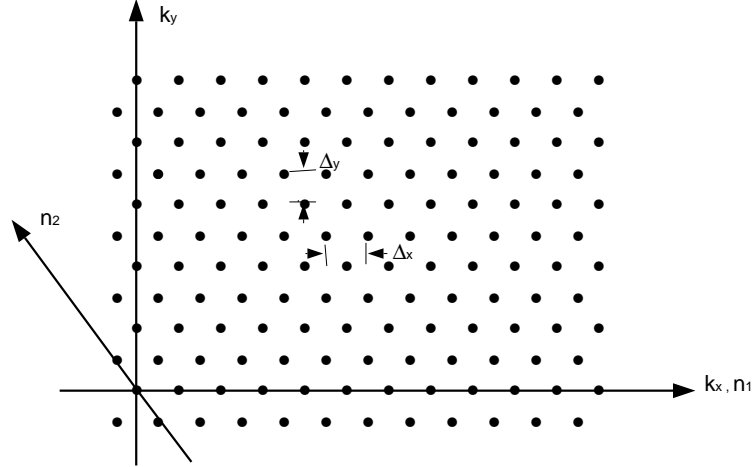


Figure 4.2: Hexagonal sampling pattern.

as

$$y = Fx + u \quad (4.2.1)$$

where  $u$  is zero-mean, i.i.d. noise. If we sample the image  $y$  using a single position of the sensor array with offset indexed by  $i$ , we can represent this by

$$y_i = Q_i y \quad (4.2.2)$$

where  $Q_i$  downsamples the fully sampled image and orders the result into a vector. Then we can rewrite  $y$  in a rearranged form  $y_r$  as

$$\begin{aligned} y_r &= [y_1^H \ y_2^H \ \dots \ y_n^H]^H \\ &= [Q_1^H \ Q_2^H \ \dots \ Q_n^H]^H (Fx + u) \\ &= Q_r Fx + u_r \end{aligned} \quad (4.2.3)$$

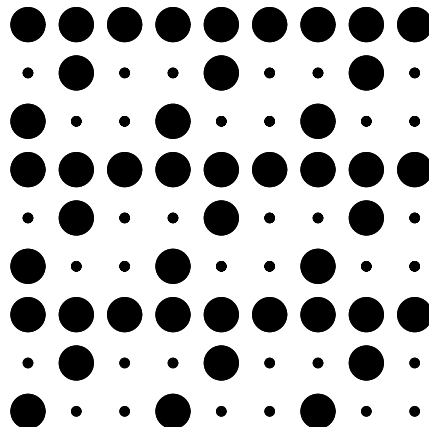


Figure 4.3: Periodic nonuniform sampling example.

where  $u_r$  is the similarly rearranged version of  $u$  and  $Q_r = [Q_1^H \ Q_2^H \ \dots \ Q_n^H]^H$ . If we choose a subset of  $k$  of the  $n$  shifted arrays, we obtain

$$\begin{aligned}
 \tilde{y}_r &= [y_{i_1}^H \ y_{i_2}^H \ \dots \ y_{i_k}^H]^H & (4.2.4) \\
 &= [Q_{i_1}^H \ Q_{i_2}^H \ \dots \ Q_{i_k}^H]^H (Fx + u) \\
 &= \tilde{Q}_r Fx + \tilde{u}_r
 \end{aligned}$$

where  $\tilde{u}_r$  is the corresponding subset of  $u_r$  and  $\tilde{Q}_r$  is the corresponding subset of  $Q_r$ .

As long as the  $\{Q_i\}$  are properly chosen and enough subsets are selected, the unknown spatial samples  $x$  can be reconstructed from  $\tilde{y}_r$  in a least-squares sense by

$$\hat{x} = (F^H \tilde{Q}_r^H \tilde{Q}_r F)^{-1} F^H \tilde{Q}_r^H \tilde{y}_r \quad (4.2.5)$$

The precise conditions under which a least-squares reconstruction is defined are discussed in [101] and [95]. A necessary condition is that the product of the number of samples



in the array and the number of selected array positions equals or exceeds the number of unknown frequency samples. Assuming that  $u$  has unit variance, the sum of squared errors (SSE) in the reconstructed spatial samples is given by

$$E(\tilde{Q}_r) = \text{tr}(F^H \tilde{Q}_r^H \tilde{Q}_r F)^{-1} \quad (4.2.6)$$

### 4.3 Basic Optimization Algorithm

We must optimize (4.2.6) with respect to the entries of  $\tilde{Q}_r$  to provide the most useful information for reconstruction of images in the minimal necessary acquisition time. Unfortunately, optimization of (4.2.6) is a large-scale combinatoric optimization problem, and an optimal solution is prohibitive to find. We use sequential backward selection (SBS) to optimize (4.2.6). The key challenge in this optimization task is that the available SBS algorithms do not apply directly, since they are designed to eliminate one sample location at a time [98]. Instead, we must eliminate a whole periodic array of samples at one time here. This severely complicates the relevant equations and the resulting computational complexity of an already complex algorithm.

Without loss of generality, we assume that  $F$  is scaled so that it has orthonormal columns. Therefore, we have the following from [98]:

$$E(Q_r) = \text{tr}(F^H \tilde{Q}_r^H \tilde{Q}_r F)^{-1} \quad (4.3.1)$$

$$= \text{tr}(F^H \tilde{Q}_r^H \tilde{Q}_r F)^{-1} F^H F \quad (4.3.2)$$

$$= \text{tr} F(F^H \tilde{Q}_r^H \tilde{Q}_r F)^{-1} F^H \quad (4.3.3)$$

To manipulate this matrix, we use the following theorem.

**Theorem 4.3.1** *The matrix  $B = F(F^H \tilde{Q}_r^H \tilde{Q}_r F)^{-1} F^H$  can be represented in the following form:*

$$B = [H_1 H_2 \dots H_n] \begin{bmatrix} Q_1^H Q_1 \\ Q_2^H Q_2 \\ \vdots \\ Q_n^H Q_n \end{bmatrix} \quad (4.3.4)$$

where  $H_i, i = 1, \dots, n$ , are convolution matrices.

The proof is in Appendix B. Let  $Z = F^H \tilde{Q}_r^H \tilde{Q}_r F$  and  $Y$  be the matrix that results after  $Q_j$  is deleted. Then  $Y = Z - F^H Q_j^H Q_j F$ . By using the matrix inversion formula, we have

$$Y^{-1} = Z^{-1} + Z^{-1} F^H Q_j^H (I - Q_j F Z^{-1} F^H Q_j^H)^{-1} Q_j F Z^{-1} \quad (4.3.5)$$

$$F Y^{-1} F^H = F Z^{-1} F^H + F Z^{-1} F^H Q_j^H (I - Q_j F Z^{-1} F^H Q_j^H)^{-1} Q_j F Z^{-1} F^H \quad (4.3.6)$$

Suppose that we delete the array corresponding to  $Q_j$  from  $Q_r$  so that  $B$  becomes  $\tilde{B}$  and  $Q_r$  becomes  $\tilde{Q}_r$ . Then from (4.3.6) and the definition of  $B$

$$\tilde{B} = B + B Q_j^H (I - Q_j B Q_j^H)^{-1} Q_j B$$

$$= B + BQ_j^H G_j Q_j^H B \quad (4.3.7)$$

where  $G_j = (I - Q_j B Q_j^H)^{-1}$ . This matrix inverse can be evaluated efficiently as a result of the following theorem:

**Theorem 4.3.2** *Assume that the  $\{H_i\}$  are circulant matrices. Then  $G_j$  is a circulant matrix.*

The proof is in Appendix B.

Because  $G_j$  is the inverse of a circulant matrix, it can be computed efficiently using FFT's.

Using the fact that  $B$  is symmetric,  $Q_j Q_j^H = I$  and  $Q_i Q_j^H = 0$  with  $i \neq j$ , the updating term of Eq. (4.3.7) becomes

$$\begin{aligned} \Delta_j &= BQ_j^H G_j Q_j B^H \\ &= H_j Q_j^H Q_j Q_j^H G_j Q_j Q_j^H Q_j H_j^H \\ &= H_j Q_j^H G_j Q_j H_j^H \end{aligned} \quad (4.3.8)$$

From the property  $\text{tr}(ABC) = \text{tr}(BCA)$ , we have

$$\text{tr}(\Delta_j) = \text{tr}(G_j Q_j H_j^H H_j Q_j^H) \quad (4.3.9)$$

In the form of (4.3.9), the criterion increment can be efficiently evaluated for all remaining  $j$ , since the matrix in the right-hand trace can be evaluated much more efficiently than can  $\Delta_j$ . The array  $j$  that gives the minimum value of (4.3.9) will cause the

minimum SSE increase and therefore should be deleted. Only after we determine the optimal  $j$  are we required to compute  $\Delta_j$ .

Once the optimal  $j$  is chosen, we must update the convolution kernels  $h_i, i = 1, 2, \dots, n$ , that construct the convolution matrices  $H_i, i = 1, 2, \dots, n$ , so that they are available for the next elimination step. First, we need initial values for the  $\{H_i\}$  to begin the SBS process. If we begin with all arrays selected,  $Q_r^H Q_r = I$ , and we have

$$B = F(F^H F)^{-1} F^H \quad (4.3.10)$$

$$= F F^H \quad (4.3.11)$$

Thus, the initial  $B$  represents an operation in the frequency domain that is equivalent to zeroing the spatial-domain signal outside the ROS. Consequently, the initial  $\{H_i\}$  matrices are chosen to be the equivalent convolution operation with the ROS as the spatial response. These matrices are stored and updated as impulse responses rather than in their full matrix representation.

Because both  $B$  and  $\tilde{B}$  in (4.3.7) are of the form (4.3.4), the update term  $\Delta_j = \tilde{B} - B$  is also of the same form. Thus, the convolution matrices that define  $\tilde{B}$  can be updated by updating  $H_i, i = 1, \dots, n$ . The form of the update is given by

$$\Delta_j = [\Delta H_{1,j} \quad \Delta H_{2,j} \quad \dots \quad \Delta H_{n,j}] \begin{bmatrix} Q_1^H Q_1 \\ Q_2^H Q_2 \\ \vdots \\ Q_n^H Q_n \end{bmatrix} \quad (4.3.12)$$

More specifically, these update terms are given by

$$\begin{aligned}
\Delta_j &= BQ_j^H G_j Q_j B^H \\
&= H_j Q_j^H G_j Q_j [H_1 \ H_2 \ \dots \ H_n] \begin{bmatrix} Q_1^H Q_1 \\ Q_2^H Q_2 \\ \vdots \\ Q_n^H Q_n \end{bmatrix}
\end{aligned} \tag{4.3.13}$$

Thus,

$$\begin{aligned}
\tilde{B} &= [H_1 + \Delta H_{1,j} \ H_2 + \Delta H_{2,j} \ \dots \ H_n + \Delta H_{n,j}] \begin{bmatrix} Q_1^H Q_1 \\ Q_2^H Q_2 \\ \vdots \\ Q_n^H Q_n \end{bmatrix} \\
&= [\tilde{H}_1 \ \tilde{H}_2 \ \dots \ \tilde{H}_n] \begin{bmatrix} Q_1^H Q_1 \\ Q_2^H Q_2 \\ \vdots \\ Q_n^H Q_n \end{bmatrix}
\end{aligned} \tag{4.3.14}$$

Since the matrices  $\{\Delta H_{i,j}\}$  are circulant, we only need to calculate one column of each.

Let  $h_i$  be the first column of  $H_i$ . Then we use the following procedure to calculate the update:

For  $i = 1, \dots, n$ :

1.  $r = Q_j h_i$ . This is accomplished by downsampling  $h_i$  with offset  $j - 1$ .

2.  $s = G_j r$ . This is a filtering operation using FFT's.
3.  $t = Q_j^H s$ . This is an upsampling operation with offset  $j - 1$ .
4.  $\Delta h_i = H_j t$ . This is a filtering operation using FFT's.

Thus, we can implement the algorithm with convolution kernels rather than huge non-sparse matrices. We can efficiently evaluate the criterion increase with (4.3.9) and update the convolution kernels with (4.3.12) and (4.3.14) using only convolution, down-sampling, and upsampling operations. The above updating process can be continued recursively until the minimal number of arrays remains. The proposed method dramatically reduces storage and computational complexity.

#### 4.4 Image reconstruction from nonuniform samples

Once the best array set  $\tilde{y}_r$  is selected, the unknown spatial samples  $x$  (and thus the entire spatial-domain image) can be reconstructed from  $\tilde{y}_r$  in a least-squares sense. However, the least-square solution in (4.2.5) involves inversion of a huge matrix. Therefore, directly using (4.2.5) to reconstruct the image is probably prohibitive. However, if we store the resulting impulse responses from the SBS process that correspond to the selected array offsets, we can efficiently compute the least-squares reconstruction as follows:

$$\begin{aligned}\hat{y} &= F^H (F \tilde{Q}_r^H \tilde{Q}_r F^H)^{-1} F \tilde{Q}_r^H \tilde{y}_r \\ &= \tilde{B} \tilde{Q}_r^H \tilde{y}_r\end{aligned}$$

$$= [\tilde{H}_1 \ \tilde{H}_2 \ \dots \ \tilde{H}_n] \begin{bmatrix} Q_1^H Q_1 \\ Q_2^H Q_2 \\ \vdots \\ Q_n^H Q_n \end{bmatrix} \tilde{y}_r \quad (4.4.1)$$

where  $\tilde{H}_1 \ \tilde{H}_2 \ \dots \ \tilde{H}_n$  has been computed with the efficient algorithm in Section 4.3.

Then the spatial samples can be reconstructed as follows:

$$\hat{x} = F\hat{y} \quad (4.4.2)$$

With (4.4.1) and (4.4.2), we can efficiently reconstruct the whole spatial image with convolutions.

## 4.5 Experiments

Figure 4.4(a) shows a circular region of support (ROS) containing 3205 unknowns in a  $64 \times 64$  grid. We experimented with three cases for this ROS, in which the number of array elements decreased from case to case but the number of possible dithered positions increased, so that the number of potential sample locations was fixed. In each case we began with all possible array offsets and sequentially eliminated one array offset at a time.

Table 4.1 lists the simulation results for these three cases. In the first case, the criterion matrix was undefined after three arrays were eliminated. (The inverse in (4.3.3) does not exist.) To keep the criterion defined, we needed to keep 14 of the  $16 \times 16$  arrays, corresponding to 3584 samples. In the second and third cases, 52 of the  $8 \times 8$  arrays and

Table 4.1: Comparison of the criterion in three cases

Case 1 16x16	# of arrays criterion	16 3205	15 4244	14 5612	13 undefined
Case 2 8x8	# of arrays criterion	64 3205	60 4178	56 5357	52 8542
Case 3 4x4	# of arrays criterion	256 3205	240 4171	224 5358	208 7658
Case 4 8x8	# of arrays criterion	64 3779	60 4202	56 4990	52 8445
	# of samples	4096	3840	3584	3328

208 of the  $4 \times 4$  arrays were necessary to keep the criterion defined, corresponding to 3328 samples. The latter sample pattern yielded a lower error criterion than the former with the same total number of samples. Figure 4.5(a) shows the same ROS in a  $128 \times 128$  grid. This allowed us to consider array offsets spaced more closely together. We experimented with one case (Case 4) for this ROS. In comparison with Case 2, the array size is the same but there are 256 possible array locations in Case 4. The same number of arrays and samples were necessary to keep the criterion defined, but the criterion achieved was lower. The comparison of Case 2 and Case 4 suggests that with the same array size, the more possible offsets the better the potential performance. However, this seems to be a function of where the SBS procedure is stopped, which is evident from a comparison of the various intermediate stopping points.

Figure 4.4(b), 4.4(c), and 4.4(d) show the selected sample patterns for Case 1, Case 2, and Case 3. Figure 4.5(b) shows the selected sample pattern for Case 4.



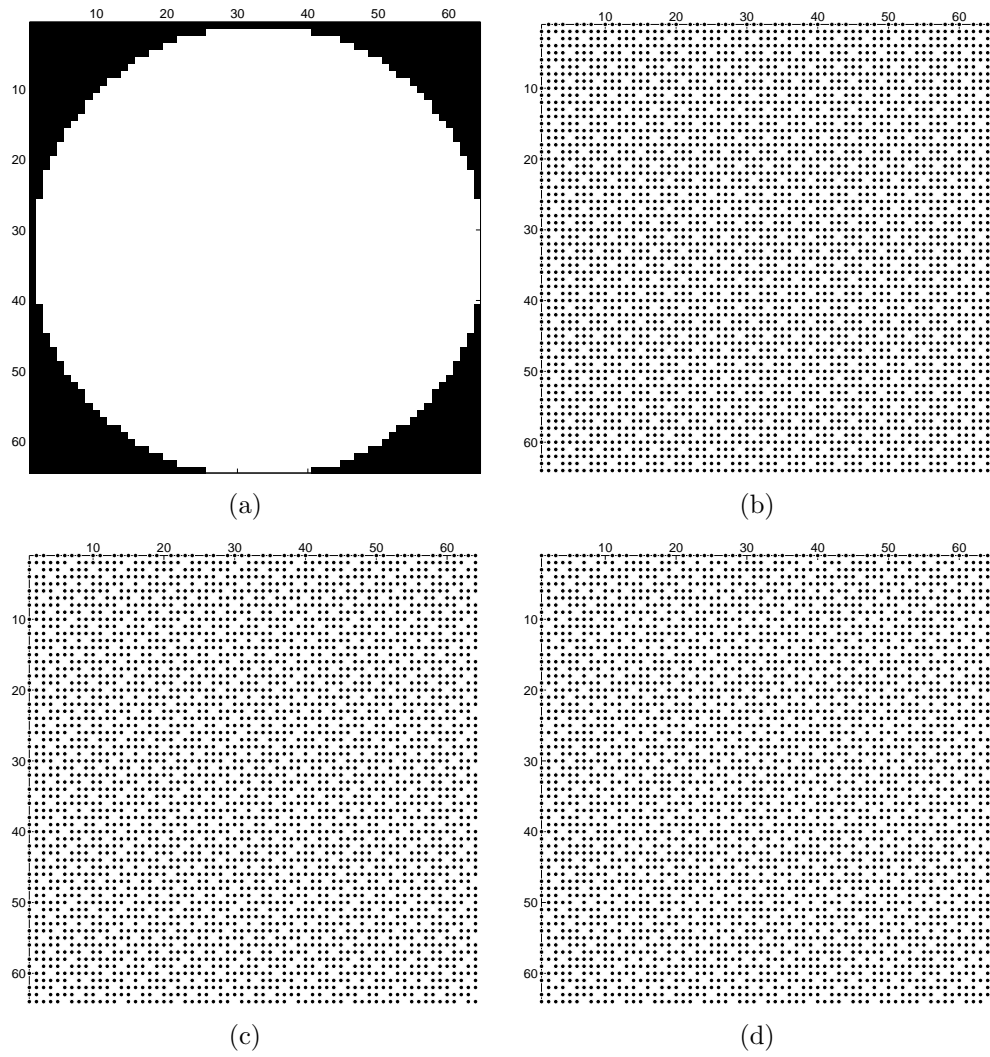


Figure 4.4: (a) The  $64 \times 64$  region of support (3205 unknowns) (b) 3584 selected samples in the case 1 (c) 3328 selected samples in the case 2 (d) 3328 selected samples in the case 3 (black markers indicate selected samples)

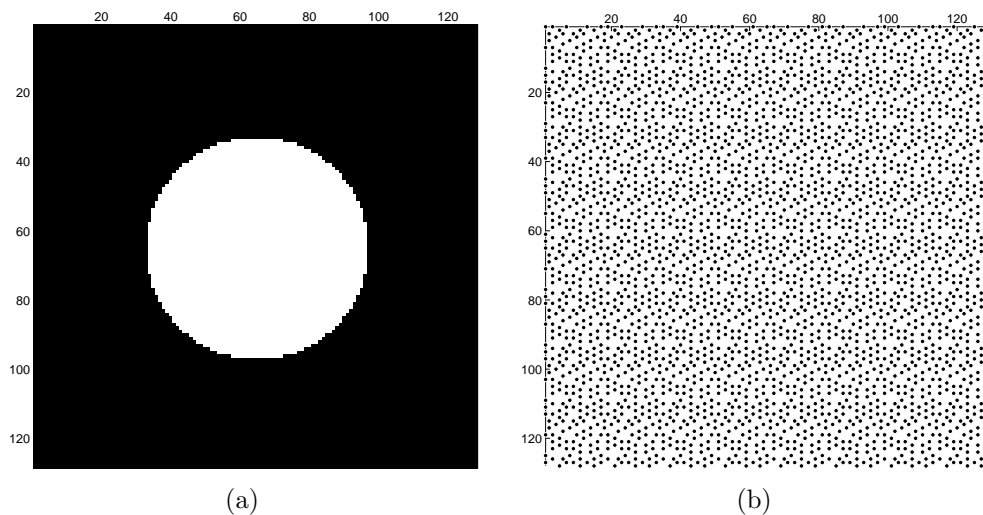


Figure 4.5: (a) The  $128 \times 128$  region of support (white points indicate 3205 unknowns) (b) 3328 selected samples in Case 4

#### 4.6 Conclusion

We have developed an efficient sampling pattern optimization technique that provides the most useful information for reconstructing images with a limited ROS in the minimal necessary acquisition time. The proposed algorithm has the following advantages: 1) it provides an efficient update formula for the criterion based on convolution kernels rather than large, non-sparse matrices; 2) it provides an efficient update formula for the convolution kernels based on the deleted array; 3) it provides an efficient reconstruction method based on convolution. The proposed method dramatically reduces storage and computational complexity. We found that the lowest SSE is obtained when the number of possible dithered positions is largest, given the same total number of samples.

We have not accounted for some practical concerns. That is, we have assumed throughout that all filtering operations are circular convolutions. Furthermore, one must take into account the fact that the array and the image have a finite size, and therefore boundary effects become an issue.

## CHAPTER 5

### SEQUENTIAL FORWARD ARRAY SELECTION

#### 5.1 Introduction

In this chapter, we develop an efficient algorithm different from that in Chapter 4 for optimizing the dithering pattern so that the image can be reconstructed from a periodic nonuniform set of samples as reliably as possible. In this algorithm, we begin the development with the modified criterion from Chapter 2 and sequentially select the least noisy sample recursively based on a given ROS until the desired number of arrays is selected. To simplify the complicated block selection algorithm, we decompose the block selection algorithm into a sum of single sample selection algorithms. To avoid the singularity at the switching point, we further modify the criterion for extending the selection process from the number of unknowns more than the number of selected samples to less than the number of selected samples. The advantage of this method compared to the SFS of single samples is time saved from selecting one block each time. The disadvantage is that it may be impossible to reach the minimum density. The advantage compared to SBS of sample blocks is that it brings real-time implementation into the realm of possibility because the previously selected sample block can be observed while the next sample block is selected.

#### 5.2 Notation

If we represent the discretized frequency image with size  $m \times n$  as a column-ordered vector  $y$ , the unknown discretized spatial support by a vector  $x$ , and the mapping from

the spatial-domain samples to the frequency-domain image by  $F$ , the fully sampled frequency image can be expressed as

$$y = Fx + w \quad (5.2.1)$$

where  $w$  is zero-mean, i.i.d. noise. Suppose the array size is  $m_1 \times n_1$  and the possible dithered positions of the array are  $m_2 \times n_2$ . We have  $m = m_1 \times m_2$  and  $n = n_1 \times n_2$ .

If we sample the frequency image  $y$  using a single position of the sensor array with offset indexed by  $1 \leq i \leq n$ , we can represent this by

$$y_i = Q_i y \quad (5.2.2)$$

where  $Q_i$  downsamples the fully sampled image and orders the result into a vector. Then we can rewrite  $y$  in a rearranged form  $y_r$  as

$$\begin{aligned} y_r &= [y_1^H \ y_2^H \ \dots \ y_n^H]^H \quad (5.2.3) \\ &= [Q_1^H \ Q_2^H \ \dots \ Q_{L_1}^H]^H (Fx + w) \\ &= Q_r Fx + w_r \end{aligned}$$

where  $w_r$  is the similarly rearranged version of  $w$  and  $Q_r = [Q_1^H \ Q_2^H \ \dots \ Q_n^H]^H$ . If we choose a subset of  $k$  of the  $N$  shifted arrays, we obtain

$$\begin{aligned} \tilde{y}_r &= [y_{k_1}^H \ y_{k_2}^H \ \dots \ y_{k_k}^H]^H \quad (5.2.4) \\ &= [Q_{k_1}^H \ Q_{k_2}^H \ \dots \ Q_{k_k}^H]^H (Fx + w) \end{aligned}$$

$$= \tilde{Q}_r F x + \tilde{w}_r$$

where  $\tilde{w}_r$  is the corresponding subset of  $w_r$  and  $\tilde{Q}_r$  is the corresponding subset of  $Q_r$ .

### 5.3 Criterion

Let  $A = \tilde{Q}_r F$ . In chapter 2, we have shown that the criteria is the trace of  $(AA^H)^{-1}$  when the number of selected samples is less than the number of unknowns in in the ROS and the trace of  $(A^H A)^{-1}$  when the number of selected samples is more than the number of unknowns in the ROS. To unite these two different criteria into one for selection purposes, we propose a modified criterion as follows

$$\begin{aligned} E(\tilde{Q}_r) &= \text{tr}(AA^H + \varepsilon I)^{-1} \\ &= \text{tr}(\tilde{Q}_r F F^H \tilde{Q}_r^H + \varepsilon I)^{-1} \end{aligned} \quad (5.3.1)$$

where  $\varepsilon$  is a very small number.

Let  $n_r$  be the number of unknowns in the ROS. When  $m_1 n_1 k \leq n_r$  and  $A_k A_k^H$  is nonsingular,

$$\lim_{\varepsilon \rightarrow 0} \text{tr}(A_k A_k^H + \varepsilon I_k)^{-1} = \text{tr}(A_k A_k^H)^{-1} \quad (5.3.2)$$

Let the singular value decomposition of  $A_k = U_k \Sigma_k V_k^H$ . Then

$$\begin{aligned} \text{tr}(A_k A_k^H + \varepsilon I)^{-1} &= \text{tr}(U_k \Sigma_k \Sigma_k^H U_k^H + \varepsilon I_k)^{-1} \\ &= \text{tr} U_k^H (U_k \Sigma_k \Sigma_k^H U_k^H + \varepsilon I_k)^{-1} U_k \end{aligned}$$

$$\begin{aligned}
&= \text{tr} (\Sigma_k \Sigma_k^H + \varepsilon U_k^H U_k)^{-1} \\
&= \text{tr} (\Sigma_k \Sigma_k^H + \varepsilon I_k)^{-1}
\end{aligned} \tag{5.3.3}$$

When  $m_1 n_1 k \geq n_r$ ,  $\Sigma_k$  has only  $n_r$  nonzero elements.

$$\text{tr} (\Sigma_k \Sigma_k^H + \varepsilon I_k)^{-1} = \sum_{i=1}^{n_r} \frac{1}{|\sigma_i|^2 + \varepsilon} + (m_1 n_1 k - n_r) \frac{1}{\varepsilon} \tag{5.3.4}$$

$$\begin{aligned}
\text{tr} (A_k^H A_k)^{-1} &= \lim_{\varepsilon \rightarrow 0} \sum_{i=1}^{n_r} \frac{1}{|\sigma_i|^2 + \varepsilon} \\
&= \lim_{\varepsilon \rightarrow 0} \text{tr} (A_k A_k^H + \varepsilon I)^{-1} - (m_1 n_1 k - n_r) \frac{1}{\varepsilon}
\end{aligned} \tag{5.3.5}$$

Since the second term in 5.3.5 is a constant at each step, it has no effect on the selection procedure. We only need this term to evaluate the true criterion after the selection. Therefore, 5.3.3 and 5.3.5 show the reasonability of the selection criterion in 5.3.1.

#### 5.4 Efficient recursive algorithm

To simplify the computational method, we first transform the block matrix in 5.3.1 into a diagonal block matrix after some modulation.

$$\begin{aligned}
AA^H &= \tilde{Q} F F^H \tilde{Q}^H \\
&= [Q_{n_1}^H F F^H Q_{n_2}^H \cdots Q_{n_k}^H]^H F F^H [Q_{n_1} Q_{n_2} \cdots Q_{n_k}]
\end{aligned}$$

$$= \begin{bmatrix} Q_{n_1} F F^H Q_{n_1}^H & Q_{n_1} F F^H Q_{n_2}^H & \cdots & Q_{n_1} F F^H Q_{n_k}^H \\ Q_{n_2} F F^H Q_{n_1}^H & Q_{n_2} F F^H Q_{n_2}^H & \cdots & Q_{n_2} F F^H Q_{n_k}^H \\ \vdots & \vdots & \cdots & \vdots \\ Q_{n_k} F F^H Q_{n_1}^H & Q_{n_k} F F^H Q_{n_2}^H & \cdots & Q_{n_k} F F^H Q_{n_k}^H \end{bmatrix} \quad (5.4.1)$$

$Q_i F F^H Q_j^H, i, j = 1, 2, \dots, n$ , are easily seen to be circulant matrices, since  $F F^H$  is circulant and  $Q_i F F^H Q_i$  are the same for  $i = 1, 2, \dots, n$  because  $F F^H$  is a circulant matrix. Therefore,  $AA^H$  is conjugate symmetric matrix with circulant blocks [120] (circulant-block-circulant blocks in the 2-D case).

Let  $F_d$  represent the downsampled Fourier matrix corresponding to the dithered array. Then  $F_d^H F_d = I$ .  $F_d Q_i F F^H Q_j F_d^H$  diagonalizes the circulant matrix  $Q_i F F^H Q_j, i, j = 1, 2, \dots, n$  [120]. Let  $\text{diag}(d_{ij1}, d_{ij2}, \dots, d_{ijg}) = F_d Q_i F F^H Q_j F_d^H$ . Finally, let  $F_D$  be a block-diagonal matrix formed by replicating  $F_d$  along the diagonal  $k$  times,

$$\begin{aligned} & (AA^H)^{-1} \\ &= F_D F_D^H (AA^H)^{-1} F_D F_D^H \\ &= F_D (F_D A A^H F_D^H)^{-1} F_D^H \\ &= F_D \begin{bmatrix} F_D Q_{n_1} F F^H Q_{n_1}^H F_D d^H & F_D Q_{n_1} F F^H Q_{n_2}^H F_D^H & \cdots & F_D Q_{n_1} F F^H Q_{n_k}^H F_D^H \\ F_D Q_{n_2} F F^H Q_{n_1}^H F_D^H & F_D Q_{n_2} F F^H Q_{n_2}^H F_D^H & \cdots & F_D Q_{n_2} F F^H Q_{n_n}^H F_D^H \\ \vdots & \vdots & \cdots & \vdots \\ F_D Q_{n_k} F F^H Q_{n_1}^H F_D^H & F_D Q_{n_k} F F^H Q_{n_2}^H F_D^H & \cdots & F_D Q_{n_k} F F^H Q_{n_k}^H F_D^H \end{bmatrix}^{-1} F_D^H \end{aligned}$$



$$\begin{aligned}
&= F_D \begin{bmatrix} \text{diag}(d_{111} \cdots d_{11m}) & \text{diag}(d_{121} \cdots d_{12m}) & \cdots & \text{diag}(d_{1n1}d_{1n2} \cdots d_{1nm}) \\ \text{diag}(d_{211} \cdots d_{21m}) & \text{diag}(d_{221} \cdots d_{22m}) & \cdots & \text{diag}(d_{2n1} \cdots d_{2nm}) \\ \vdots & \vdots & \cdots & \vdots \\ \text{diag}(d_{k11} \cdots d_{k1m}) & \text{diag}(d_{k21} \cdots d_{k2m}) & \cdots & \text{diag}(d_{nn1} \cdots d_{nnm}) \end{bmatrix}^{-1} F_D^H \\
&= F_D \begin{bmatrix} \text{diag}(\hat{d}_{111} \cdots \hat{d}_{11m}) & \text{diag}(\hat{d}_{121} \cdots \hat{d}_{12m}) & \cdots & \text{diag}(\hat{d}_{1n1}\hat{d}_{1n2} \cdots \hat{d}_{1nm}) \\ \text{diag}(\hat{d}_{211} \cdots \hat{d}_{21m}) & \text{diag}(\hat{d}_{221} \cdots \hat{d}_{22m}) & \cdots & \text{diag}(\hat{d}_{2n1} \cdots \hat{d}_{2nm}) \\ \vdots & \vdots & \cdots & \vdots \\ \text{diag}(\hat{d}_{k11} \cdots \hat{d}_{k1m}) & \text{diag}(\hat{d}_{k21} \cdots \hat{d}_{k2m}) & \cdots & \text{diag}(\hat{d}_{nn1} \cdots \hat{d}_{nnm}) \end{bmatrix} F_D^H
\end{aligned} \tag{5.4.2}$$

where

$$\begin{aligned}
D_g^{-1} &= \begin{bmatrix} d_{11g} & d_{12g} & \cdots & d_{1kg} \\ d_{21g} & d_{22g} & \cdots & d_{2kg} \\ \vdots & \vdots & \cdots & \vdots \\ d_{k1g} & d_{k2g} & \cdots & d_{kkg} \end{bmatrix}^{-1} \\
&= \begin{bmatrix} \hat{d}_{11g} & \hat{d}_{12g} & \cdots & \hat{d}_{1kg} \\ \hat{d}_{21g} & \hat{d}_{22g} & \cdots & \hat{d}_{2kg} \\ \vdots & \vdots & \cdots & \vdots \\ \hat{d}_{k1g} & \hat{d}_{k2g} & \cdots & \hat{d}_{kkg} \end{bmatrix}
\end{aligned} \tag{5.4.3}$$

where  $g = 1, 2, \dots, m$ . To calculate the vector  $d_{ij}$ , we do the following steps, which involves only FFT's instead of matrix operations [120, 121].

1. Take the FFT of the ROS image to get the impulse response  $h$ , which is the first column of  $FF^H$ .  $FF^H$  is a circulant matrix. Only the first column needs to be stored.
2. Shift  $h$  by  $j$ , then downsample the shifted  $h$  by  $Q_i$  to get the first column  $h_d$  of the circulant matrix  $Q_i FF^H Q_j$ ,  $i, j = 1, 2, \dots, n$ .
3. Take the FFT of  $h_d$  to get the diagonal vector of the diagonal matrix  $F_d Q_i FF^H Q_j F_d^H$ .

By using the property  $\text{tr}(ABC) = \text{tr}(CAB)$ , we have

$$\begin{aligned}
& \text{tr}(AA^H)^{-1} \\
&= \text{tr} \left( F^H F_d \begin{bmatrix} \text{diag}(\hat{d}_{111} \hat{d}_{112} \cdots \hat{d}_{11m}) & \cdots & \text{diag}(\hat{d}_{1k1} \hat{d}_{1k2} \cdots \hat{d}_{1km}) \\ \text{diag}(\hat{d}_{211} \hat{d}_{212}^H \cdots \hat{d}_{21m}^H) & \cdots & \text{diag}(\hat{d}_{2k1} \hat{d}_{2k2} \cdots \hat{d}_{2km}) \\ \vdots & \cdots & \vdots \\ \text{diag}(\hat{d}_{k11}^H \hat{d}_{k12}^H \cdots \hat{d}_{k1m}^H) & \cdots & \text{diag}(\hat{d}_{kk1} \hat{d}_{kk2} \cdots \hat{d}_{kkm}) \end{bmatrix} \right) \\
&= \text{tr} \begin{bmatrix} \text{diag}(\hat{d}_{111} \hat{d}_{112} \cdots \hat{d}_{11m}) & \cdots & \text{diag}(\hat{d}_{1k1} \hat{d}_{1k2} \cdots \hat{d}_{1km}) \\ \text{diag}(\hat{d}_{211} \hat{d}_{212} \cdots \hat{d}_{21m}) & \cdots & (\hat{d}_{2k1} \hat{d}_{2k2} \cdots \hat{d}_{2km}) \\ \vdots & \vdots & \cdots & \vdots \\ \text{diag}(\hat{d}_{k11} \hat{d}_{k12} \cdots \hat{d}_{k1m}) & \cdots & \text{diag}(\hat{d}_{kk1} \hat{d}_{kk2} \cdots \hat{d}_{kkm}) \end{bmatrix} \quad (5.4.4)
\end{aligned}$$

Let  $\tilde{A}$  represent the new  $A$  after the  $i$ th array is added to  $A$ .

$$\begin{aligned}
\tilde{A}\tilde{A}^H &= [Q^H \ Q_i^H]^H FF^H [Q \ Q_i] \\
&= \begin{bmatrix} QFF^H Q^H & QFF^H Q_i^H \\ Q_i^H FF^H Q^H & Q_i FF^H Q_i^H \end{bmatrix} \quad (5.4.5)
\end{aligned}$$

Let  $\tilde{D}_g$  represent the corresponding new  $D_g$  after adding the  $i$ th array.

$$\tilde{D}_g = \begin{bmatrix} D_g & S_{i_g}^H \\ S_{i_g} & T_{i_g} \end{bmatrix} \quad (5.4.6)$$

With Lemma 2.3.5 and 2.3.11 in Chapter 2, we have

$$\tilde{D}_g^{-1} = \begin{bmatrix} P^{-1} + P^{-1}S_i^H\sigma_iS_iP^{-1} & -P^{-1}S_i^H \\ -\sigma_iS_iP^{-1} & \sigma_i^{-1} \end{bmatrix} \quad (5.4.7)$$

where  $\sigma_i = T_i - S_iP^{-1}Q_i$  is a scalar,  $T_i$  are the same for  $i = 1, 2, \dots, m$  and  $P = D_g$ .

$$\text{tr}(\tilde{D}_g^{-1}) = \text{tr}(P^{-1}) + \frac{1 + S_iP^{-2}S_i^H}{T_i - S_iP^{-1}R_i} \quad (5.4.8)$$

Let  $\nabla_g$  represent the second term in (5.4.8) and  $\nabla$  represent the criterion increment for each step. Then

$$\nabla_g = \frac{1 + S_iP^{-2}S_i^H}{T_i - S_iP^{-1}R_i} \quad (5.4.9)$$

$$\nabla = \sum_{g=1}^m \nabla_g \quad (5.4.10)$$

where  $g = 1, 2, \dots, m$ .

We select the array to minimize  $\nabla$  each step.

## 5.5 Efficient computational method

To find the minimizer of  $\nabla$  in 5.4.10, which we denote as the  $i$ th array, we need to calculate  $\nabla_g, g = 1, 2, \dots, n$  for every possible  $j = 1, 2, \dots, n$ . That is, we must calculate

$S_j P^{-1} S_j^H$  and  $S_j P^{-2} S_j^H$  for every possible  $j = 1, 2, \dots, n$ . The computational burden will be huge. To reduce the computational cost, we derived recursive formulas for the above two terms such that the updated parts are calculated based only on the previous selected array.

Let  $\tilde{S}_j$  represent the new  $S_j$  after the  $i$ th array added. Note that the elements of  $\tilde{S}_j$  come from  $S_j$ , but  $\tilde{S}_j$  only includes the elements corresponding to the offsets already selected,  $s_{ji}$ . Let  $\tilde{P} = \tilde{D}_g$ ,  $\sigma_i = H_i = T_i - S_i P^{-1} Q_i$ ,  $R_i = P^{-1} S_i^H$ . Then

$$\begin{aligned}
& \tilde{S}_j \tilde{P}^{-1} \tilde{S}_j^H \\
&= [S_j \ s_{ji}] \begin{bmatrix} P^{-1} + \frac{1}{\sigma_i} P^{-1} S_i^H S_i P^{-1} & -P^{-1} S_i^H \\ -\frac{1}{\sigma_i} S_i P^{-1} & \frac{1}{\sigma_i} \end{bmatrix} [S_j \ s_{ji}]^H \\
&= S_j P^{-1} S_j^H + S_j P^{-1} S_i^H H_i^{-1} S_i P^{-1} S_j^H - S_j P^{-1} S_i^H H_i^{-1} s_{ji}^H + s_{ji} H_i^{-1} s_{ji} \\
&= S_j P^{-1} S_j^H + \frac{1}{\sigma_i} (S_j R_i) (S_j R_i)^H - \frac{1}{\sigma_i} s_{ji} (S_j R_i)^H - \frac{1}{\sigma_i} (S_j R_i) s_{ji}^H + \frac{1}{\sigma_i} s_{ji} s_{ji}^H \\
&= S_j P^{-1} S_j^H + \frac{1}{\sigma_i} (||S_j R_i|| - 2\text{Re}((S_j R_i) s_{ji}^H) + |s_{ji}|) \tag{5.5.1}
\end{aligned}$$

Let  $F_i = P^{-1} R_i$ .

$$\begin{aligned}
& \tilde{S}_j \tilde{P}^{-2} \tilde{S}_j^H \\
&= [S_j \ s_{ji}] \begin{bmatrix} P^{-1} + \frac{1}{\sigma_i} P^{-1} S_i^H S_i P^{-1} & -P^{-1} S_i^H \\ -\frac{1}{\sigma_i} S_i P^{-1} & \frac{1}{\sigma_i} \end{bmatrix}^2 [S_j \ s_{ji}]^H \\
&= S_j P^{-2} S_j^H + S_j P^{-2} S_i^H H_i^{-1} S_i P^{-1} S_j^H - S_j P^{-2} S_i^H H_i^{-1} s_{ji}^H \\
&\quad + S_j P^{-1} S_i^H H_i^{-1} S_i P^{-2} S_j^H + S_j P^{-1} S_i^H H_i^{-1} S_i P^{-2} S_i^H H_i^{-1} P^{-1} S_j^H \\
&\quad - S_j P^{-1} S_i^H H_i^{-1} S_i P^{-2} S_i^H H_i^{-1} s_{ji}^H - s_{ji} H_i^{-1} S_i P^{-2} S_j^H
\end{aligned}$$

$$\begin{aligned}
& -s_{ji}H_i^{-1}S_iP^{-2}S_i^H H_i^{-1}S_iP^{-1}S_j^H + s_{ji}H_i^{-1}S_iP^{-2}S_i^H H_i^{-1}s_{ji}^H \\
& + S_jP^{-1}S_i^H H_i^{-2}S_iP^{-1}S_j^H - S_jP^{-1}S_i^H H_i^{-2}s_{ji}^H - s_{ji}H_i^{-2}S_iP^{-1}S_j^H + s_{ji}H_i^{-2}s_{ji}^H \\
= & S_jP^{-2}S_j^H + \frac{2}{\sigma_i}Re(S_jR_i(S_jF_i)^H) - \left(\frac{2}{\sigma_i}((S_jF_i)s_{ji}^H) + S_jF_i s_{ij}^H\right) \\
& + \frac{1 + \|R_i\|^2}{\sigma_i^2} \|S_jR_i\|^2 + \frac{1 + \|R_i\|^2}{\sigma_i^2} |s_{ji}|^2 - \frac{1 + \|R_i\|^2}{\sigma_i^2} 2Re((S_jR_i)s_{ji}^H) \\
= & S_jP^{-2}S_j^H + \frac{2}{\sigma_i}(Re(S_jR_i(S_jF_i)^H) - (S_jF_i)s_{ji}^H) \\
& + \frac{1 + \|R_i\|^2}{\sigma_i^2} (\|S_jR_i\|^2 - 2Re((S_jR_i)s_{ji}^H) + |s_{ji}|^2)
\end{aligned} \tag{5.5.2}$$

With (5.5.1) and (5.5.2), the inverses only operate on the previous selection array rather than all possible arrays. We use Gaussian elimination to solve for  $R_i$  and  $F_i$ . The computational cost is drastically reduced.

## 5.6 Experiments

Figure 5.1(a) shows a circular region of support (ROS) containing 3205 unknowns in a  $64 \times 64$  grid. We experimented with three cases for this ROS, in which the number of array elements decreased from case to case but the number of possible dithered positions increased, so that the number of potential sample locations was fixed. In each case we began with all possible array offsets and sequentially eliminated one array offset at a time.

In Case 1, the array size is  $4 \times 4$ , and the number of possible dithered positions is  $16 \times 16$ . In Case 2, the number of dithered positions is  $8 \times 8$ , the array size is  $8 \times 8$ . In Case 3, the number of possible dithered positions is  $16 \times 16$ , the array size is  $4 \times 4$ . Figure 5.1(b), (c), (d) shows the sampling pattern with 13 arrays selected in Case 1,

52 arrays selected in Case 2, and 208 arrays selected in Case 3 (corresponding to 3328 points).

To make a comparison with the same array size but different number of potential dithered positions we considered Case 4. In Case 4, the array size is  $8 \times 8$ , the same as that in Case 2. However, the number of possible dithered positions is  $16 \times 16$ , different than that in Case 2. In Case 4, we set  $\varepsilon = 10^{-2}$  to reduce accumulated error due to ill-conditioning. Figure 5.2(a) shows a  $128 \times 128$  ROS with 3205 unknowns. Figure 5.2(b) shows the selection pattern with 52 arrays (3328 points) selected.

Table 5.1 shows the criterion values at various steps for the four cases. In the experiments, we used  $\varepsilon = 10^{-4}$  to avoid the singularity in the selection process. When all 4096 samples are selected, the criterion values for Case 1, Case 2, and Case 3 are approximately equal to  $891/\varepsilon$ . This is consistent with the analysis. Let  $A = FS$ ,  $S$  is diagonal matrix with 3205 diagonal elements corresponding to nonzero unknowns as 1 and 891 diagonal elements corresponding to zero locations as 0.

$$\begin{aligned} \text{tr}(AA^H + \varepsilon I)^{-1} &= (FSF^H + \varepsilon FF^H)^{-1} \\ &= F(S + \varepsilon I)^{-1}F^H \end{aligned} \quad (5.6.1)$$

$$\begin{aligned} \text{tr}(AA^H + \varepsilon I)^{-1} &= \text{tr}(F^H F(S + \varepsilon I)^{-1}) \\ &= \text{tr}(S + \varepsilon I)^{-1} \\ &= \frac{891}{\varepsilon} + \frac{3205}{1 + \varepsilon} \\ &\approx 8910000 + 3205 \end{aligned}$$

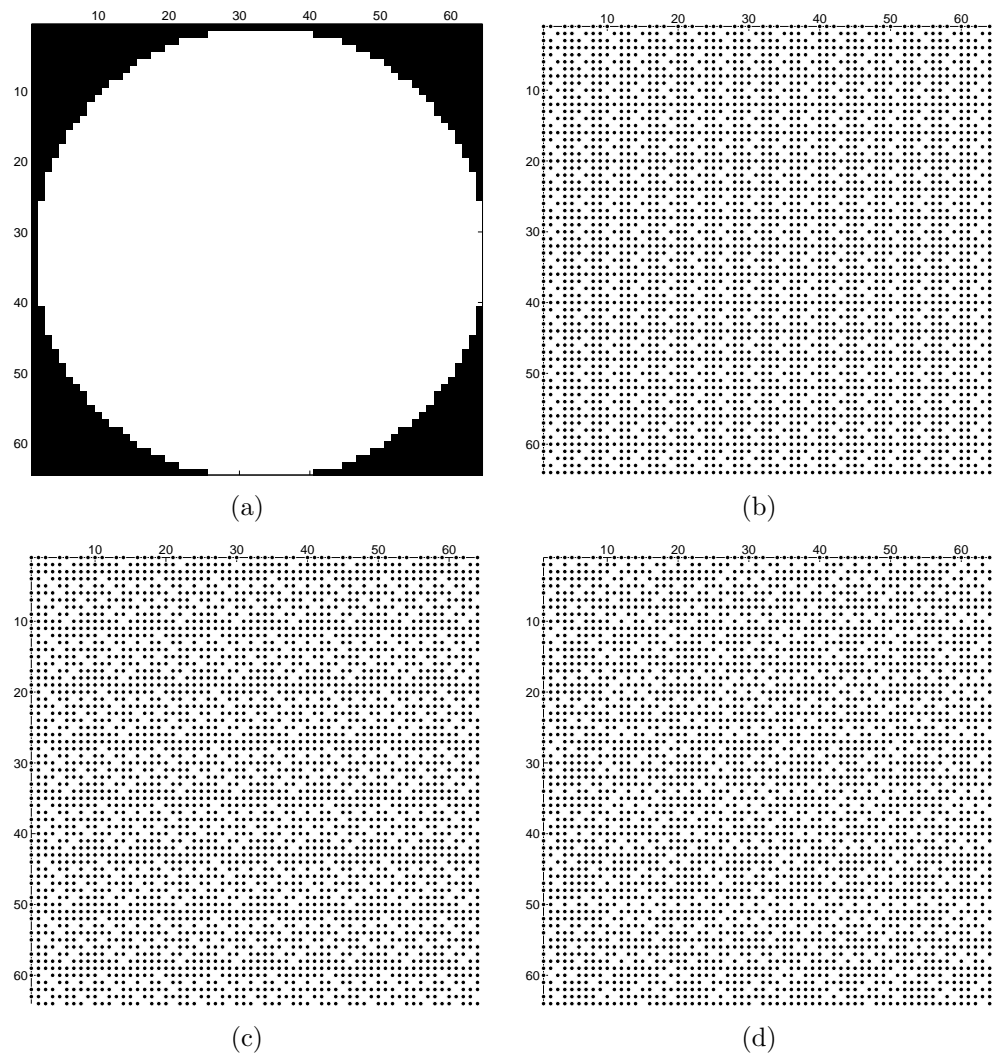


Figure 5.1: (a) The  $64 \times 64$  region of support (3205 unknowns) (b) 3328 selected samples in Case 1 (c) 3328 selected samples in Case 2 (d) 3328 selected samples in Case 3 (black markers indicate selected samples)

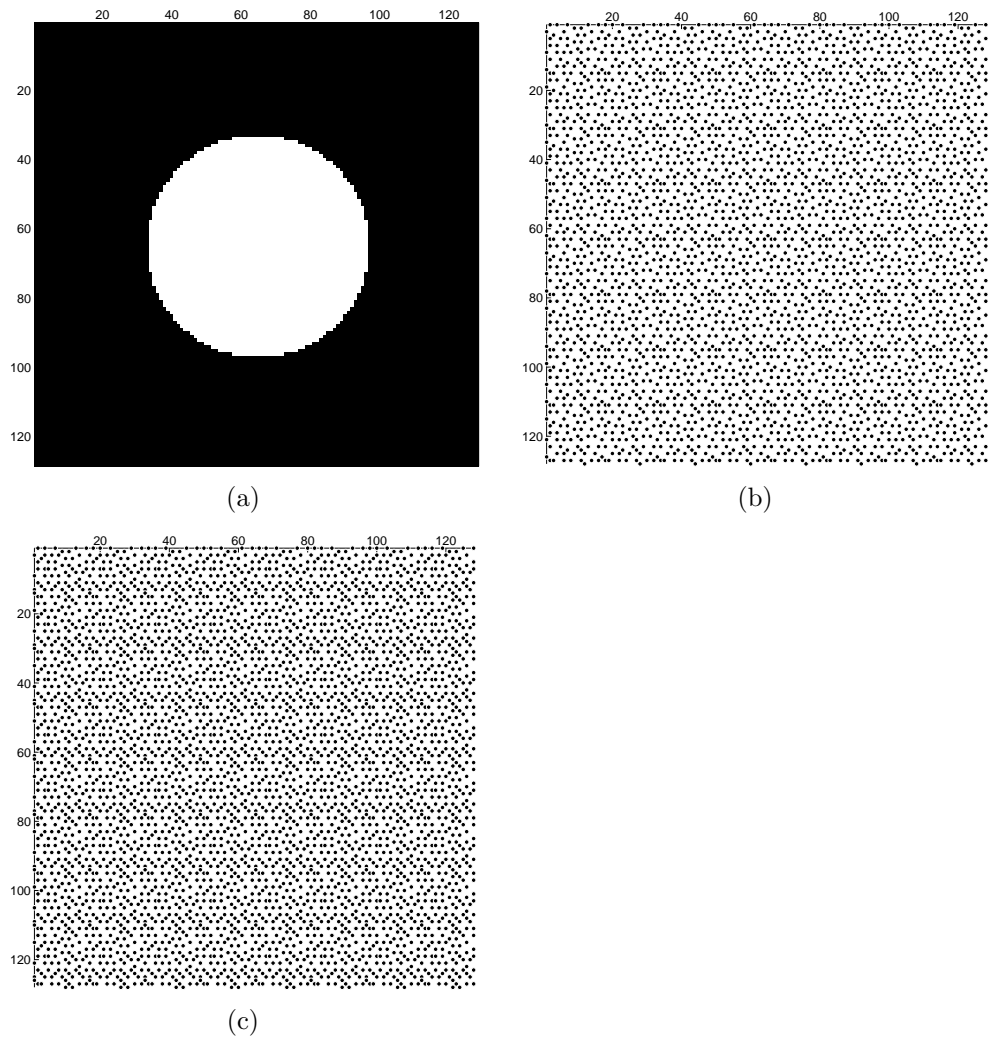


Figure 5.2: (a) The  $128 \times 128$  region of support (white points indicate 3205 unknowns) (b) 3328 selected samples in Case 4 (c) 4096 selected samples in Case 4.



Table 5.1: Comparison of the criterion in four cases

Case 1 16x16	# of arrays criterion	9 0.950431	13 1839970	14 3789951	15 6349934	16 8909999
Case 2 8x8	# of arrays criterion	36 0.892832	52 1229985	56 3789957	60 6349921	64 8909938
Case 3 4x4	# of arrays criterion	144 0.884639	208 1230000	224 3789985	240 6349982	256 8910071
Case 4 8x8	# of arrays criterion	36 0.840235	52 12302.2	56 37901.3	60 63501.1	64 89100.9
	# of samples	2340	3328	3584	3840	4096

Table 5.2: Comparison of the criterion in four cases

Case 1 16x16	# of arrays	9	13	14	15	16
	SFS time (s)	4.25	6.85	7.59	8.34	9.11
	SBS time (s)	N/A	N/A	6.71	3.48	0
Case 2 8x8	# of arrays	36	52	56	60	64
	SFS time (s)	9.19	20.92	25.15	30.0	35.69
	SBS time (s)	N/A	1111.9	766	398	0
Case 3 4x4	# of arrays	144	208	224	240	256
	SFS time (s)	87.34	291.91	367.37	477.89	600.17
Case 4 8x8	# of arrays	36	52	56	60	64
	SFS time (s)	21.94	42.60	49.46	57.07	65.65
	# of samples	2340	3328	3584	3840	4096

$$\approx 891/\varepsilon \tag{5.6.2}$$

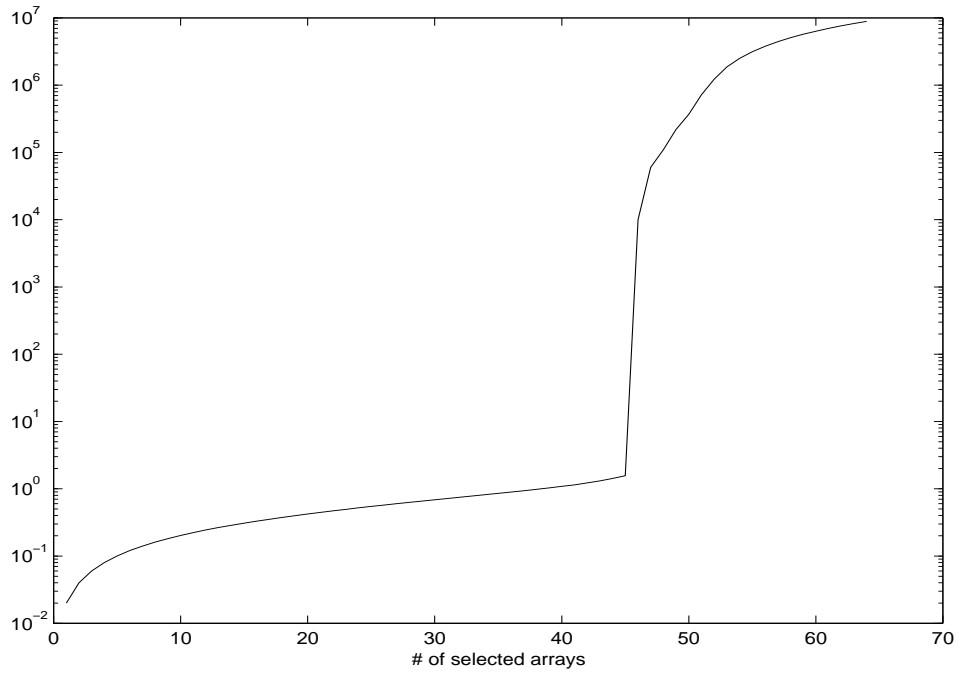
Comparing the criterion values at 3328 samples ( 13 arrays in Case 1, 52 arrays in Case 2 and Case 4 and 208 arrays in Case 3), the values are close for Case 2, 3, and 4 (adjusting Case 4 by a factor of  $10^2$  to compensate for the different choice of  $\varepsilon$ ). However, the criterion value for Case 1 is much higher. Taking into account the time cost, the experimental result in Case 2 is desired. It takes 21 seconds to select 52 arrays

and half a minute to finish the whole selection process in Case 2. For the larger field of view (FOV) in Case 4, it takes 42.60 seconds to select 52 arrays, 65.65 seconds to select 64 arrays (corresponding to 4096 samples), and 1 hour 9 minutes 16 seconds to finish the whole selection. Table 5.2 shows the time cost for the four cases and sequential backward selection for Case 1 and Case 2. In comparison with the sequential backward array selection, sequential forward array selection is of more practical value because it can get the desired selection in a minute.

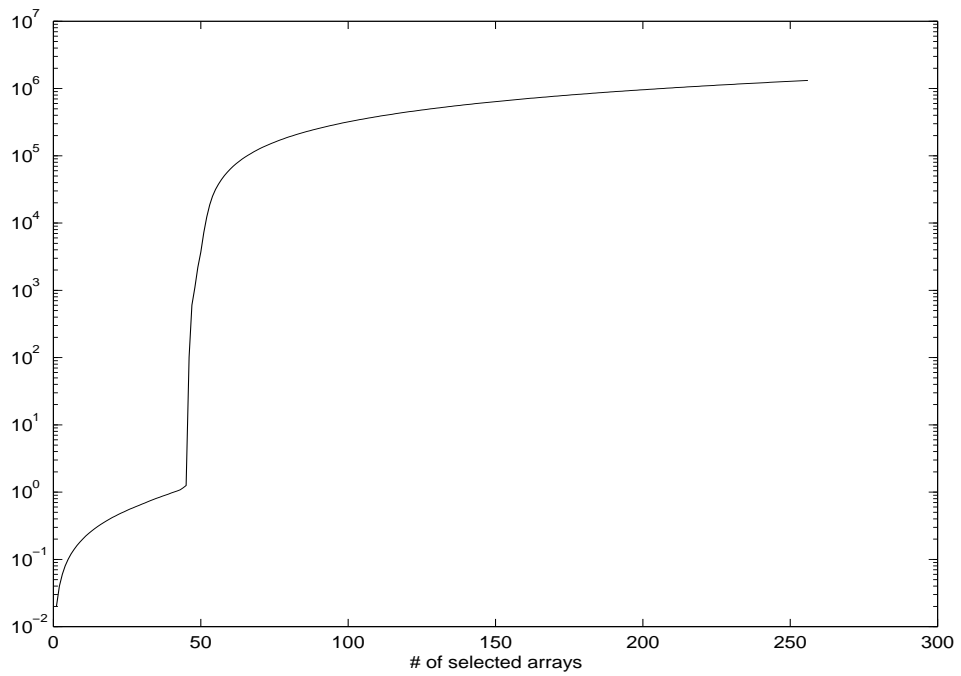
Figure 5.3(a) and (b) show the logarithmic scale of criterion curve in Case 2 and Case 4. We observed that the criterion has a sharp increase because of the singularity of  $AA^H$ . With a few more samples than the unknowns selected, the criterion curve eventually becomes smooth. The criterion curve eventually increases uniformly because adding the value  $\varepsilon$  makes the selection increment nearly uniform for the last phase of the selection process. The increase due to the  $1/\varepsilon$  term dominates the increase.

## 5.7 Conclusion

We developed an efficient sequential forward array selection technique that provides the most useful information for restoring and superresolving bandlimited images in a minute. We developed a modified criterion to unite the whole selection process. We derived an efficient recursive selection algorithm for the update criterion. We derived a recursive algorithm for efficiently computing inverse related terms such that they can be updated based only on the previous selected array. We use Gaussian elimination to find a set of small inverse solutions at each step. The proposed method has important potential in practice because it can select a reduced set of the most useful samples in a



(a)



(b)

Figure 5.3: (a) The semilog criterion curve in Case 2 (b) The semilog criterion curve in Case 4

minute and can reconstruct the image with fewer samples than regular sampling. This may reduce the image acquisition time greatly and is very important in applications to MRSI, PMMW imaging, and multiband digital signal reception.

## CHAPTER 6

### CONCLUSION AND DISCUSSION

Four efficient optimal magnetic resonance observation selection schemes have been proposed to overcome the problems in those existing methods, reduce observation time, and improve the image resolution.

#### **6.1 Efficient sequential forward selection**

In Chapter 2, we proposed an efficient SFS optimization scheme, which has the following advantages: 1) it overcomes the limitation of the SFS algorithm based on the standard MSE criterion in that it can start with an empty initial matrix; 2) it drastically reduces storage space and computational time with the proposed SFS recursive algorithm and the conjugate gradients algorithm; 3) it is more applicable in practice than SBS in that the best sample can be observed as soon as it is selected, making possible real-time selection and acquisition. Simulation with real MR data shows a good-quality image can be reconstructed with only a few more samples than the minimum density by our method.

Further work is clearly necessary to accelerate the algorithm if it is to be useful in a real-time context on an ordinary computer. However, the algorithm described here makes the possibility of real-time implementation into the realm of feasibility appear promising.

## 6.2 Efficient backward selection of hexagonal samples

In Chapter 3, we proposed a new method for efficiently choosing MRSI samples by applying SBS on hexagonal samples. We computed a generalized MDFT with Smith form decomposition and output rectangular image pixels directly from hexagonal samples without interpolation. A rate lower than the Nyquist rate on a hexagonal grid can be achieved with the proposed method. Furthermore, SBS on a hexagonal sampling grid takes less selection time than SBS on a rectangular sampling grid,

## 6.3 Efficient selection of sample block

In Chapter 4, we developed a method for selecting a periodic array of samples. It used an efficient update formula for the criterion based on convolution kernels rather than large, non-sparse matrices, an efficient update formula for the convolution kernels based on the deleted array, and an efficient reconstruction method based on convolution and FFT's. The proposed method dramatically reduces storage and computational complexity. We found that the lowest SSE is obtained when the number of possible dithered positions is largest, given the same total number of samples.

## 6.4 Efficient sequential forward selection of array

In Chapter 5, we developed an efficient sequential forward array selection technique that rapidly selects a reduced set of the most important samples for reconstructing images with a limited ROS. We developed a modified criterion applicable to the whole selection process such that the selection smoothly switches from the case with the number of samples less than the number of unknowns to the case with the number of samples more

than the number of unknowns. We derived an efficient recursive selection algorithm for the update criterion. We derived an efficient recursive algorithm for computing inverse-related terms such that they can be updated based only on the previous selected array. We use Gaussian elimination to solve for a set of small matrix inversions at each step. With this efficient strategy, the proposed method can finish the selection process within half a minute for a practical size of image and can reconstruct the image with fewer samples than regular sampling. This advantage may reduce the image acquisition time greatly and make it very promising in applications such as MRSI, PMMW imaging, and multiband digital signal reception.

## 6.5 Future work

1. A remaining problem is to derive an upper bound on SBS for array selection. The upper bound for SBS for single samples was derived by Reeves and Zhao [100]. Deriving the upper bound for SBS for array selection appears to be a much more challenging problem.
2. Another problem remaining is to develop an algorithm for beginning with a standard ROS and adjusting the selection for a modified ROS. To decrease the selection time for the SFS algorithm, it is possible to assume several standard ROS's, choose the ROS closest to the actual head as the standard ROS, and start selection of samples from the standard ROS selection.

## APPENDIX A

We prove that circular shifts of the selected samples and the ROS yield the same value of the MSE criteria. For ease of notation, we consider the 1-D case. The proof for the 2-D case is exactly the same, although the notation is more involved.

**Theorem 6.5.1** *Let  $\{s_i\}$  and  $\{\widehat{s}_i\}$  be two sets of size  $m$  such that  $\widehat{s}_i = ((s_i + l))_M$  for arbitrary  $l$ , where  $((n))_M = n \bmod M$ . Also, let  $\{r_i\}$  and  $\{\widehat{r}_i\}$  be two sets of size  $n$  such that  $\widehat{r}_i = ((r_i + k))_M$  for arbitrary  $k$ . Let  $A$  and  $A_{l,k}$  have elements defined as  $a(i, j) = e^{-j2\pi \frac{s_i r_j}{M}}$  and  $\widehat{a}(i, j) = e^{-j2\pi \frac{\widehat{s}_i \widehat{r}_j}{M}}$ . Then,*

$$\text{tr}(A^H A)^{-1} = \text{tr}(A_{l,k}^H A_{l,k})^{-1} \text{ if } m \geq n \text{ and } (A^H A)^{-1} \text{ exists,}$$

and

$$\text{tr}(A A^H)^{-1} = \text{tr}(A_{l,k} A_{l,k}^H)^{-1} \text{ if } m \leq n \text{ and } (A A^H)^{-1} \text{ exists.}$$

**Proof:** The individual terms in  $A_{l,k}$  are of the form,

$$e^{-j2\pi \frac{\widehat{s}_i \widehat{r}_j}{M}} = e^{-j2\pi \frac{s_i r_j}{M}} e^{-j2\pi \frac{l r_j}{M}} e^{-j2\pi \frac{k s_i}{M}} e^{-j2\pi \frac{k l}{M}} \quad (6.5.1)$$



Therefore,

$$\begin{aligned}
A_{l,k} &= e^{-j2\pi \frac{kl}{M}} \begin{bmatrix} e^{-j2\pi \frac{ks_1}{M}} & 0 & \cdots & 0 \\ 0 & e^{-j2\pi \frac{ks_2}{M}} & \cdots & 0 \\ \vdots & \vdots & \ddots & \vdots \\ 0 & 0 & \cdots & e^{-j2\pi \frac{ks_m}{M}} \end{bmatrix} A \begin{bmatrix} e^{-j2\pi \frac{lr_1}{M}} & 0 & \cdots & 0 \\ 0 & e^{-j2\pi \frac{lr_2}{M}} & \cdots & 0 \\ \vdots & \vdots & \ddots & \vdots \\ 0 & 0 & \cdots & e^{-j2\pi \frac{lr_n}{M}} \end{bmatrix} \\
&= \alpha H_s A H_r
\end{aligned} \tag{6.5.2}$$

For convenience, we have denoted the left-hand matrix above as  $H_s$  and the right-hand matrix as  $H_r$ , and  $\alpha = e^{-j2\pi \frac{kl}{M}}$ . It is apparent that both matrices are unitary, which will be useful below.

If  $m \geq n$ ,

$$\begin{aligned}
\text{tr}(A_{l,k}^H A_{l,k})^{-1} &= \text{tr}((\alpha H_s A H_r)^H \alpha H_s A H_r)^{-1} \\
&= \alpha \alpha^* \text{tr}(H_r^{-1} (A^H A)^{-1} H_r) \\
&= \text{tr}(H_r H_r^{-1} (A^H A)^{-1}) \\
&= \text{tr}(A^H A)^{-1}
\end{aligned} \tag{6.5.3}$$

If  $m \leq n$ ,

$$\begin{aligned}
\text{tr}(A_{l,k} A_{l,k}^H)^{-1} &= \text{tr}(\alpha H_s A H_r (\alpha H_s A H_r)^H)^{-1} \\
&= \alpha \alpha^* \text{tr}(H_s (A A^H)^{-1} H_s^{-1}) \\
&= \text{tr}(H_s^{-1} H_s (A A^H)^{-1}) \\
&= \text{tr}(A A^H)^{-1}
\end{aligned} \tag{6.5.4}$$

## APPENDIX B

*Proof of Theorem 4.3.1:*

For simplicity, we present a proof for the 1-D case; the 2-D case is conceptually identical but requires more complex notation. Define  $\tilde{S}_j$  as a matrix implementing a k-space shift and  $S_j$  as the corresponding spatial-domain matrix operator made up of linear-phase weights; that is,

$$\tilde{S}_j F = F S_j \quad (6.5.5)$$

We observe that  $\tilde{S}_j^H \tilde{S}_j = I$  and  $S_j^H S_j = I$ . Let  $i = j \bmod N$ , and  $k = N \lfloor j/N \rfloor$ , where  $N$  is the spacing between samples in the sensor array; thus,  $j = i + k$ . Define  $e_j$  as the unit sample vector shifted by  $j - 1$  samples. Then the  $j$ th column of  $F^H (F \tilde{Q}_r^H \tilde{Q}_r F^H)^{-1} F$  is given by

$$F (F^H \tilde{Q}_r^H \tilde{Q}_r F)^{-1} F^H e_j = F (F^H \tilde{Q}_r^H \tilde{Q}_r F)^{-1} F^H \tilde{S}_k e_i \quad (6.5.6)$$

$$= F S_k (S_k^H F^H \tilde{Q}_r^H \tilde{Q}_r S_k F S_k)^{-1} S_k^H F^H \tilde{S}_k e_i \quad (6.5.7)$$

$$= \tilde{S}_k F (F^H \tilde{S}_k^H \tilde{Q}_r^H \tilde{Q}_r \tilde{S}_k F)^{-1} F e_i \quad (6.5.8)$$

Because  $\tilde{S}_k$  shifts the sensor array by an integer number of periods of the sensor array pattern,  $\tilde{Q}_r S_k = \tilde{Q}_r$ . In this case we have from (6.5.8)

$$F^H (F \tilde{Q}_r^H \tilde{Q}_r F^H)^{-1} F e_{i+k} = \tilde{S}_k F^H (F \tilde{Q}_r^H \tilde{Q}_r F^H)^{-1} F e_i \quad (6.5.9)$$

Thus, the response to an impulse at location  $i + k$  is a copy shifted by  $k$  of the response to an impulse at location  $i$ . That is, there is an impulse response associated with each shifted position of the sensor array.

Using the matrix form in (4.3.4) and post-multiplying by  $e_j$ , we have

$$B = [H_1 H_2 \dots H_n] \begin{bmatrix} \tilde{Q}_1^H Q_1 \\ Q_2^H Q_2 \\ \vdots \\ Q_n^H Q_n \end{bmatrix} e_j \quad (6.5.10)$$

$$= H_{i+1} e_j \quad (6.5.11)$$

$$= \tilde{S}_k H_{i+1} e_i \quad (6.5.12)$$

Thus, by defining a Toeplitz matrix  $H_{i+1}$  such that  $F^H (F \tilde{Q}_r^H \tilde{Q}_r F^H)^{-1} F e_i = H_{i+1} e_i$ , we obtain the structure in (4.3.4).

*Proof of Theorem 4.3.2:*

Observe that  $Q_j Q_j^H = I$  and  $Q_i Q_j^H = 0$  for  $i \neq j$ . Then

$$\begin{aligned} Q_j B Q_j^H &= Q_j [H_1 H_2 \dots H_n] \begin{bmatrix} Q_1^H (Q_1 Q_j^H) \\ Q_2^H (Q_2 Q_j^H) \\ \vdots \\ Q_n^H (Q_n Q_j^H) \end{bmatrix} \\ &= Q_j H_j Q_j^H \end{aligned} \quad (6.5.13)$$

Thus,

$$G_j = (I - Q_j H_j Q_j^H)^{-1} \quad (6.5.14)$$

Using the fact that a circulant matrix with downsampled rows and columns is a circulant matrix,  $Q_j H_j Q_j^H$  corresponds to a circulant matrix. Furthermore, the sum of circulant matrices and the inverse of a circulant matrix are still circulant matrices. Therefore,  $G_j$  is a circulant matrix.

## BIBLIOGRAPHY

- [1] Z. H. Cho, J. P. Jones, and M. Singh, *Foundations of Medical Imaging*. Wiley, 1993.
- [2] T. F. Kirn, "Magnetic resonance spectroscopy may hold promise in studying metabolites, tissues," *Journal of the American Medical Association*, vol. 261, p. 1103ff., 1989.
- [3] J. H. Duyn, "Spectroscopic imaging techniques." ISMRM 1998 spectroscopy teaching course, 1998.
- [4] S. J. Nelson, D. B. Vigneron, and W. P. Dillon, "Serial evaluation of patients with brain tumors using volume MRI and 3D 1H MRSI," *NMR in Biomedicine*, vol. 12, pp. 123–138, May 1999.
- [5] C. M. Segebarth, D. F. Baleriaux, P. R. Luyten, and J. A. den Hollander, "Detection of metabolic heterogeneity of human intracranial tumors in vivo by 1H NMR spectroscopic imaging," *Magn Reson Med*, vol. 13, pp. 62–76, Jan 1990.
- [6] M. J. Fulham, A. Bizzi, M. J. Dietz, H. H. Shih, R. Raman, G. S. Sobering, J. A. Frank, A. J. Dwyer, J. R. Alger, and G. D. Chiro, "Mapping of brain tumor metabolites with MR spectroscopic imaging: clinical relevance," *Magn Reson Med*, vol. 13, pp. 62–76, Jan. 1990.
- [7] P. R. Luyten *et al.*, "Metabolic imaging of patients with intracranial tumors: H-1 MR spectroscopic imaging and PET," *Radiology*, vol. 176, pp. 791–799, 1990.
- [8] K. Herholz, W. Heindel, P. R. Luyten, J. A. D. Hollander, U. Pietrzyk, J. Voges, H. Kugel, G. Friedman, and W. D. Heiss, "In-vivo imaging of glucose consumption and lactate concentration in human gliomas," *Ann. Neurol*, vol. 31, p. 319, 1992.
- [9] M. J. Fulham, A. Bizzi, M. J. Dietz, H. L. Shih, R. Raman, G. S. Sobering, J. A. Frank, A. J. Dwyer, J. R. Alger, and G. D. Chiro, "Mapping of brain tumor metabolites with proton MR spectroscopic imaging: clinical relevance," *Radiology*, vol. 185, p. 675, 1992.
- [10] J. H. Duijn, G. B. Matson, A. A. Maudsley, J. W. Hugg, and M. W. Weiner, "Human brain infarction: proton MR spectroscopy," *Radiology*, vol. 183, pp. 711–8, June 1992.

- [11] P. B. Barker, J. H. G. JH, P. C. M. van Zijl, B. J. Soher, D. F. Hanley, A. M. Agildere, S. M. Oppenheimer, and R. N. Bryan, "Acute stroke: evaluation with serial proton MR spectroscopic imaging," *Radiology*, vol. 183, pp. 711–718, 1992.
- [12] R. I. Kuzniecky, J. W. Hugg, H. P. Hetherington, E. Burrerworth, E. Biler, E. Faught, and F. Gilliam, "Relative utility of  $^1\text{H}$  spectroscopic imaging and hippocampal volumetry in the lateralization of mesial temporal lobe epilepsy," *Neurology*, vol. 51, pp. 66–71, July 1998.
- [13] D. L. Arnold *et al.*, "Proton magnetic resonance spectroscopic imaging for metabolic characterization of demyelinating plaques," *Annals of Neurology*, vol. 31, no. 3, pp. 235–241, 1992.
- [14] D. J. Meyerhoff, S. MacKay, L. Bachman, N. P. W. P. Dillon, M. W. Weiner, and G. Fein, "Reduced brain n-acetylaspartate suggests neuronal loss in cognitively impaired human immunodeficiency virus- seropositive individuals: in vivo  $^1\text{H}$  magnetic resonance spectroscopic imaging," *Neurology*, vol. 43, pp. 509–515, 1993.
- [15] P. B. Barker, R. R. Lee, and J. C. McArthur, "AIDS dementia complex: evaluation with proton MR spectroscopic imaging," *Radiology*, vol. 195, pp. 58–64, 1995.
- [16] D. J. Meyerhoff, S. MacKay, J. M. Constant, D. Norman, C. V. Dyke, G. F. C, and M. W. Weiner, "Axonal injury and membrane alterations in Alzheimer's disease suggested by in vivo proton magnetic resonance spectroscopic imaging," *Ann. Neurol*, vol. 36, pp. 40–47, 1994.
- [17] G. Tedeschi, A. Bertolino, N. Lundbom, S. Bonavita, N. J. Patronas, J. H. Duyn, L. V. Metman, T. N. Chase, and G. D. Chiro, "Cortical and subcortical chemical pathology in Alzheimer's disease as assessed by multislice proton magnetic resonance spectroscopic imaging," *Neurology*, vol. 47, pp. 696–704, 1994.
- [18] B. L. Miller, R. Moats, T. Shonk, T. Ernst, S. Woolley, and B. D. Ross, "Alzheimer disease: depiction of increased cerebral myo-inositol with proton MR spectroscopy," *Radiology*, vol. 187, pp. 433–439, May 1993.
- [19] W. J. Chu, H. P. Hetherington, R. I. Kuzniecky, T. Simor, G. F. Mason, and G. A. Elgavish, "Lateralization of human temporal lobe epilepsy by  $^{31}\text{P}$  NMR spectroscopic imaging at 4.1 T," *Neurology*, vol. 51, pp. 472–479, August 1998.
- [20] F. Cendes, Z. Caramanos, F. Andermann, F. Dubeau, and D. L. Arnold, "Proton magnetic resonance spectroscopic imaging and magnetic resonance imaging volumetry in the lateralization of temporal lobe epilepsy: a series of 100 patients," *Ann. Neurol*, vol. 42, pp. 737–746, 1997.

- [21] J. W. Hugg, K. D. Laxer, G. B. Matson, A. A. Maudsley, C. A. Husted, and M. W. Weiner, "Lateralization of human focal epilepsy by  $^{31}\text{P}$  magnetic resonance spectroscopic imaging," *Neurology*, vol. 42, pp. 2011–2018, 1992.
- [22] O. A. Petroff, J. W. Prichard, T. Ogino, and R. G. Shulman, "Proton magnetic resonance spectroscopic studies of axonal carbohydrate metabolism in rabbit brain," *Neurology*, vol. 38, pp. 1569–1574, 1988.
- [23] P. A. Bottomley, C. J. Hardy, and P. B. Roemer, "Phosphate metabolite imaging and concentration measurements in human heart by nuclear magnetic resonance," *Magn. Reson. Med.*, vol. 14, pp. 425–434, 1990.
- [24] H. P. Hetherington, D. J. Luney, J. T. Vaughan, J. W. Pan, S. L. Ponder, O. Tschendel, D. B. Twieg, and G. M. Pohost, " $^{31}\text{P}$  spectroscopic imaging of the human heart at 4.1 T," *Magn. Reson. Med.*, vol. 33, pp. 427–431, 1995.
- [25] A. J. Farrall, R. T. Thompson, G. Wisenberg, C. M. Campbell, and D. J. Drost, "Myocardial infarction in a canine model monitored by two-dimensional  $^{31}\text{P}$  chemical shift spectroscopic imaging," *Magn. Reson. Med.*, vol. 38, pp. 577–584, 1997.
- [26] J. S. Taylor, D. B. Vigneron, J. Murphy-Bosch, S. J. Nelson, H. B. Kessler, I. Coia, W. Curran, and T. R. Brown, "Free magnesium levels in normal brain and brain tumors:  $^{31}\text{P}$  chemical-shift imaging measurements at 1.5 T," *Proc. Natl. Acad. Sci. USA*, vol. 88, pp. 6810–6814, 1991.
- [27] A. A. Maudsley, S. K. Hilal, W. H. Perman, and H. E. Simon, "Spatially resolved high-resolution spectroscopy by four-dimensional NMR," *J. Magn. Reson.*, vol. 51, pp. 147–152, 1983.
- [28] T. R. Brown, B. M. Kincaid, and K. Ugurbil, "NMR chemical shift imaging in three dimensions," *Proceedings of the National Academy of Sciences*, vol. 79, pp. 3523–3526, 1982.
- [29] F. Bloch, "Nuclear induction," *Phys. Rev.*, vol. 70, pp. 460–474, 1946.
- [30] P. C. Lauterber, "Image formation by induced local interactions: Examples employing nuclear magnetic resonance," *Nature*, vol. 242, pp. 190–191, 1973.
- [31] R. Damadian, "Tumor detection by nuclear magnetic resonance," *Science*, vol. 171, pp. 1151–3, 1971.
- [32] E. Andrew, P. Bottomley, W. Hinshaw, G. Holland, and W. Moore, "NMR images by the multiple sensitive point method: application to larger biological systems," *Physics in Medicine and Biology*, vol. 22, pp. 971–974, Sept. 1977.

- [33] W. S. Hinshaw, E. R. Andrew, P. A. Bottomley, G. N. Holland, and W. S. Moore, "Display of cross sectional anatomy by nuclear magnetic resonance imaging," *British journal of Radiology*, vol. 51, pp. 273–80, Apr. 1978.
- [34] W. Moore, G. Holland, and L. Kreef *CT*, vol. 4, p. 1, 1980.
- [35] G. Holland, R. Hawkes, and W. Moore, "Nuclear magnetic resonance NMR tomography of the brain: coronal and sagittal sections," *J. Comput. Assist. Tomogr.*, vol. 4, pp. 429–33, 1980.
- [36] D. D. Stark and W. G. Bradley, "Magnetic resonance imaging," *C. V. Mosby Company, St. Louis*, 1988.
- [37] B. R. Friedman, J. P. Jones, G. C. M. noz, A. P. Salmon, and C. R. B. Merritt, "Principles of MRI," *McGraw-Hill Information Services Company*, 1989.
- [38] E. M. Haacke, R. W. Brown, M. R. Thompson, and R. Venkatesan, "Physical principles and sequence design," *John Wiley and Sons, Inc. , New York*, 1989.
- [39] D. Shaw, "Fourier transform NMR spectroscopy.," *New Yor: Elsevier Scientific*, 1971.
- [40] C. P. Slichter, "Principles of magnetic resonance," *Berlin: Springer-verlag*, vol. 1, 1978.
- [41] A. Abraham, "The principles of nuclear magnetism," *Oxford: Oxford University Press*, 1961.
- [42] E. L. Hahn, "Spin echoes," *Phys. Rev.*, vol. 80, pp. 580–594, 1950.
- [43] H. Y. Carr and E. M. Purcell, "Effects of diffusion on free precession in nuclear magnetic resonance experiments," *Phys. Rev.*, vol. 94, pp. 630–638, 1954.
- [44] S. Meiboom and D. Gill, "Modified spin-echo method for measuring nuclear relaxation times," *Rev. Sci. Instrum.*, vol. 29, pp. 668–691, 1958.
- [45] D. E. Woessner, "Effects of diffusion in nuclear magnetic resonance spin-echo experiments," *J. Chem. Phys.*, vol. 34, pp. 2057–2061, 1961.
- [46] Z. H. Cho, H. S. Kim, H. B. Song, and J. Cumming, "Fourier transform nuclear magnetic resonance tomographic imaging," *IEEE Proceedings*, no. 70, pp. 1152–1173, 1982.
- [47] W. S. Hinshaw and A. Lent., "An introduction to NMR imaging: from the Bloch equation to the imaging equation," *IEEE proceedings*, vol. 71, pp. 338–350, 1983.
- [48] A. Kumar, D. Welte, and R. Ernst., "NMR Fourier zeugmatography," *J. Magn. Reson.*, vol. 18, p. 69, 1975.



- [49] P. R. Luyten, A. J. H. Marien, B. Sijtsma, and J. A. D. Hollander., “Solvent-suppressed spatially resolved spectroscopy. an approach to high-resolution NMR on a whole body system,” *J. Magn. Reson.*, vol. 67, p. 148, 1986.
- [50] J. Frahm, H. Bruhn, M. L. Gyngell, K. D. Merboldt, W. Hänicke, and R. Sauter., “Localized proton NMR spectroscopy in different regions of the human brain in vivo. Relaxation times and concentrations of cerebral metabolites,” *Magn. Reson. Med.*, vol. 11, pp. 47–67, July 1989.
- [51] W. P. Aue, S. Mueller, T. A. Cross, and J. Seelig., “Volume-selective excitation. A novel approach to topical NMR,” *J. Magn. Reson.*, vol. 56, no. 2, pp. 350–354, 1984.
- [52] S. Mueller, W. P. Aue, and J. Seelig., “NMR imaging and volume-selective spectroscopy with a single surface coil,” *J. Magn. Reson.*, vol. 63, no. 3, pp. 530–543, 1985.
- [53] P. R. Luyten and J. A. D. Hollander. *Proc. SMRM*, vol. 2, p. 1021, 1985.
- [54] P. J. Hore., “Solvent suppression in Fourier transform nuclear magnetic resonance,” *J. Magn. Reson.*, vol. 55, no. 2, pp. 283–300, 1983.
- [55] J. Frahm, K. D. Merboldt, and W. Hänicke., “Localized proton spectroscopy using stimulated echoes,” *J. Magn. Reson.*, vol. 72, no. 3, pp. 502–507, 1987.
- [56] C. Y. Rim, J. B. Ra, and Z. H. Cho., “Radial scanning technique for volume selective  $^{31}\text{P}$  spectroscopy,” *Magn. Reson. Med.*, vol. 24, pp. 100–8, Mar. 1992.
- [57] K. D. Merboldt, D. Chien, W. Hänicke, M. L. Gyngell, and H. Bruhn., “Localized  $^{31}\text{p}$  NMR spectroscopy of the adult human brain in vivo using stimulated-echo (STEAM) sequences,” *J. Magn. Reson.*, vol. 89, no. 2, pp. 343–361, 1990.
- [58] P. Styles, C. A. Scott, and G. K. Radda, “A method for localizing high-resolution NMR spectra from human subjects,” *Magn. Reson. Med.*, vol. 2, p. 402, 1985.
- [59] M. Garwood, T. Schliech, G. B. Matson, and G. Acosta, “Spatial localization of tissue metabolites by phosphorus-31 NMR rotating frame zeugmatography,” *J. Magn. Reson.*, vol. 60, no. 2, pp. 268–279, 1984.
- [60] P. A. Bottomley, T. H. Foster, and R. D. Darrow., “Depth-resolved surface-coil spectroscopy (DRESS) for in vivo  $^1\text{H}$ ,  $^{31}\text{P}$ , and  $^{13}\text{C}$  NMR,” *J. Magn. Reson.*, vol. 59, no. 2, pp. 338–342, 1984.
- [61] P. R. Luyten and J. A. D. Hollander, “ $^1\text{H}$  MR spatially resolved spectroscopy of human tissues in situ,” *Magnetic. Resonance Imaging*, vol. 4, no. 3, pp. 237–239, 1986.

- [62] P. R. Luyten, C. M. Anderson, and J. A. D. Hollander, "1H NMR relaxation measurements of human tissues in situ by spatially resolved spectroscopy," *Magnetic Resonance in Medicine*, vol. 4, pp. 431–40, May 1987.
- [63] J. Frahm, H. Bruhn, M. L. Gyngell, K. D. Merboldt, W. Hänicke, and R. Sauter, "Localized high-resolution proton NMR spectroscopy using stimulated echoes: initial applications to human brain in vivo," *Magn. Reson. Med.*, vol. 9(1), pp. 79–93, 1989.
- [64] S. Lee and Z. Cho, "Localized volume selection technique using an additional radial gradient coil," *Magnetic Resonance in Medicine*, vol. 12, pp. 56–63, October 1989.
- [65] C. J. Hardy and H. E. Cline, "Spatial localization in two dimensions using NMR designer pulses," *J. Magn. Reson.*, vol. 82, p. 647, 1989.
- [66] P. A. Bottomley and C. J. Hardy, "Two dimensional spatially selective spin inversion and spin-echo refocusing with a single nuclear magnetic resonance pulse," *J. Appl. Phys.*, vol. 62, pp. 4284–90, 1987.
- [67] P. A. Bottomley and C. J. Hardy, "Progress in efficient three-dimensional spatially localized in vivo 31p NMR spectroscopy using multidimensional spatially selective ( $\rho$ ) pulses," *J. Magn. Reson.*, vol. 74, no. 3, pp. 550–556, 1987.
- [68] C. J. Hardy, P. A. Bottomley, and P. B. Roemer, "Off-axis spatial localization with frequency modulated nuclear magnetic resonance rotating ( $\rho$ ) pulses," *J. Appl. Phys.*, vol. 63, p. 4741, 1988.
- [69] C. J. Hardy, P. A. Bottomley, , M. O'Donnell, and P. B. Roemer, "Optimization of two-dimensional spatially selective NMR pulses by stimulated annealing by stimulated," *J. Magn. Reson.*, vol. 77, no. 2, pp. 233–250, 1988.
- [70] S. Kirkpatrick, C. D. Gelatt, and M. P. Vecchi, "Optimization by stimulated annealing," *Science*, vol. 220, pp. 671–680, 1983.
- [71] N. Metropolis, A. W. Rosenbluth, A. H. Teller, and E. Teller, "Equation of state calculations by fast computing machines," *J. Chem. Phys.*, vol. 21, p. 1087, 1953.
- [72] J. Pauly, D. Nishimura, and A. Macovski, "A k-space analysis of small-tip-angle excitation," *J. Magn. Reson.*, vol. 81, pp. 43–56, 1989.
- [73] J. Pauly, D. Nishimura, and A. Macovski *Proc. SMRM*, vol. 7, p. 654, 1988.
- [74] J. B. Ra, C. Y. Rim, and Z. H. Cho, "Application of single-shot spiral scanning for volume localization," *Magn. Reson. Med.*, vol. 17, pp. 423–433, Feb. 1991.
- [75] C. B. Ahn, J. H. Kim, and Z. H. Cho, "High speed spiral-scan echo planar NMR imaging," *IEEE Tran. Med. Imag.*, vol. 5, no. 1, pp. 2–7, 1986.

- [76] C. Y. Rim, J. B. Ra, and Z. H. Cho *Proc. SMRM*, vol. 8, p. 30, 1989.
- [77] C. J. Hardy and H. E. Cline *Proc. SMRM*, vol. 8, p. 26, 1989.
- [78] D. L. Arnold, P. M. Matthews, G. S. Francis, J. O'Connor, and J. P. Antel, "Proton magnetic resonance spectroscopic imaging for metabolic characterization of demyelinating plaques," *Ann. Neurol.*, vol. 31, pp. 235–241, 1992.
- [79] X. Hu, D. N. Levin, P. C. Lauterbur, and T. A. Spraggins, "SLIM: Spectral localization by imaging," *Magnetic Resonance in Medicine*, vol. 8, pp. 314–322, 1988.
- [80] Z. Liang and P. C. Lauterbur, "A generalized series approach to MR spectroscopic imaging," *IEEE Transactions on Medical Imaging*, vol. 10, pp. 132–137, June 1991.
- [81] E. M. Stokely and D. B. Twieg, "Functional image reconstruction enhancement (FIRE) for MR spectroscopic and nuclear medicine images," in *SPIE Medical Imaging VI*, 1992.
- [82] P. Mansfield, "Multi-planar image formation using NMR spin echoes," *J. Phys. C: Solid State Phys.*, vol. 10, pp. 155–158, 1977.
- [83] S. Ljunggren, "A simple graphical representation of Fourier-based imaging methods," *J. Magn. Reson.*, vol. 54, no. 2, pp. 338–343, 1983.
- [84] J. H. Duyn and C. T. Moonen, "Fast proton spectroscopic imaging of human brain using multiple spin-echoes," *Magn Reson Med*, vol. 30, pp. 409–422, Oct. 1993.
- [85] J. H. Duyn, J. A. Frank, and C. T. Moonen, "Incorporation of lactate measurement in multi-spin-echo proton spectroscopic imaging," *Magn Reson Med*, vol. 33, pp. 101–107, Jan. 1995.
- [86] E. Adalsteinsson, P. Irarrazabal, D. M. Spielman, and A. Macovski, "Three-dimensional spectroscopic imaging with time-varying gradients," *Magn. Reson. Med*, vol. 33, pp. 461–466, 1995.
- [87] D. G. Norris and W. Dreher, "Fast proton spectroscopic imaging using the sliced k-space method," *Magn. Reson. Med.* 30, 641-645, vol. 30, pp. 641–645, 1993.
- [88] S. Posse, G. Tedeschi, R. Risinger, and D. L. R. Ogg, "High speed 1H spectroscopic imaging in human brain by echo planar spatial-spectral encoding," *Magn. Reson. Med*, vol. 33, pp. 34–40, 1995.
- [89] J. C. Ehrhardt, "MR data acquisition and reconstruction using efficient sampling schemes," *IEEE Transactions on Medical Imaging*, vol. 9, pp. 305–309, September 1990.

- [90] R. M. Mersereau, "The processing of hexagonally sampled two-dimensional signals," *Proceeding of IEEE*, vol. 67, pp. 930–949, 1979.
- [91] D. P. Petersen and D. Middleton, "Sampling and reconstruction of wave-number limited functions in n-dimensional euclidean spaces," *Information and Control*, vol. 5, pp. 279–323, 1962.
- [92] M. von Kienlin, T. Ceckler, R. Mejia, and R. S. Balaban, "Numerical optimization of the SLIM experiment for localized spectroscopy," in *Proceedings of the Society of Magnetic Resonance*, (New York, NY), 1990.
- [93] Y. Cao and D. N. Levin, "Using an image database to constrain the acquisition and reconstruction of MR images of the human head," *IEEE Transactions on Medical Imaging*, vol. 14, pp. 350–361, June 1995.
- [94] S. K. Plevritis and A. Macovski, "Alternative k-space sampling distributions for MR spectroscopic imaging," in *Proceedings of the 1994 IEEE International Conference on Image Processing*, vol. III, pp. 11–14.
- [95] R. Venkataramani and Y. Bresler, "Further results on spectrum blind sampling of 2D signals," in *Proceedings of the 1998 IEEE International Conference on Image Processing*, vol. II, pp. 752–756, 1998.
- [96] S. K. Nagle and D. N. Levin, "A new class of sampling theorems for Fourier imaging of multiple regions," in *Proceedings of the 1998 IEEE International Conference on Image Processing*, vol. II, 1998.
- [97] S. K. Nagle and D. N. Levin, "Multiple region MRI," *Magnetic Resonance in Medicine*, vol. 41, pp. 774–786, 1999.
- [98] S. J. Reeves and L. P. Heck, "Selection of observations in signal reconstruction," *IEEE Transactions on Signal Processing*, vol. 43, pp. 788–791, March 1995.
- [99] S. J. Reeves, "Selection of k-space samples in localized spectroscopy of arbitrary volumes of interest," *Journal of Magnetic Resonance Imaging*, vol. 5, pp. 245–247, March/April 1995.
- [100] S. J. Reeves and Z. Zhao, "Sequential algorithms for observation selection," *IEEE Transactions on Signal Processing*, vol. 47, pp. 123–132, January 1999.
- [101] K. F. Cheung, *Advanced Topics in Shannon Sampling and Interpolation Theory*, ch. A Multidimensional Extension of Papoulis' Generalized Sampling Expansion with the Application in Minimum Density Sampling, pp. 85–119. New York: Springer-Verlag, 1993.

- [102] Y. Gao and S. J. Reeves, "An efficient computation for sequential forward observation selection in image reconstruction," in *Proceedings of the 1998 IEEE International Conference on Image Processing*, vol. 3, pp. 380–384, 1998.
- [103] Y. Gao and S. J. Reeves, "Optimal k-space sampling in MRSI for images with a limited region of support," submitted to *IEEE Transactions on Medical Imaging*.
- [104] Y. Gao and S. J. Reeves, "Efficient forward selection of k-space samples for images with a limited region of support," in *BMES-EMBS Conference*, 1999.
- [105] Y. Gao and S. J. Reeves, "Efficient backward selection of k-space samples in MRI on a hexagonal grid," *Circuits, Systems, and Signal Processing*, to appear Aug 2000.
- [106] Y. Gao and S. J. Reeves, "Optimal dithering of focal plane arrays in passive millimeter-wave imaging," *Optical Engineering*, vol. 40, pp. 2179–2187, October 2001.
- [107] Y. Gao and S. J. Reeves, "Efficient algorithm for optimizing dithering pattern in passive millimeter-wave imaging," *the SPIE's 14th Annual International Symposium on Aerospace/Defense*, Apr. 2000.
- [108] Y. Gao and S. J. Reeves, "Optimal sampling in array-based image formation," *accepted by 2000 IEEE International Conference on Image Processing*.
- [109] S. J. Reeves and L. P. Heck, "Selection of observations in signal reconstruction," in *Proceedings of the 1993 IEEE International Conference on Acoustics, Speech, and Signal Processing*, vol. III, pp. 444–447.
- [110] G. H. Golub and C. Van Loan, *Matrix Computations*. Baltimore, MD: Johns Hopkins University Press, 2nd ed., 1989.
- [111] *Standard Mathematical Tables*. CRC Press, Inc., 30th ed., 1995.
- [112] R. L. Lagendijk, R. M. Mersereau, and J. Biemond, "On increasing the convergence rate of regularized iterative image restoration algorithms," in *Proceedings of the 1987 IEEE International Conference on Acoustics, Speech, and Signal Processing*, pp. 1183–1186.
- [113] S. J. Reeves and Z. Zhao, "New results on observation selection in signal reconstruction," in *Proceedings of the 1996 IEEE International Conference on Acoustics, Speech, and Signal Processing*, vol. III, pp. 1676–1679, 1996.
- [114] W. H. Press *et al.*, *Numerical Recipes in C*. Cambridge, 1988.
- [115] D. E. Dudgeon and R. M. Mersereau, *Multidimensional Digital Signal Processing*. New Jersey: Prentice-Hall, 1984.

- [116] J. C. Ehrhardt, "MR data acquisition and reconstruction using efficient sampling schemes," *IEEE Transactions on Medical Imaging*, vol. 9, pp. 305–309, September 1990.
- [117] A. Kaufmann and A. Henry-Labordère, *Integer and Mixed Programming: Theory and Applications*. New York: Academic, 1977.
- [118] A. Guessoum, *Fast Algorithms for the Multidimensional Discrete Fourier Transform*. PhD thesis, Georgia Institute of Technology, Mar. 1984.
- [119] B. L. Evans, T. R. Gardos, and J. H. McClellan, "Imposing Structure on Smith-Form Decompositions of Rational Resampling Matrices," *IEEE Transactions on Signal Processing*, vol. 42, pp. 970–973, April 1994.
- [120] A. K. Jain, *Fundamentals of Digital Image Processing*. Englewood Cliffs, NJ: Prentice-Hall, 1989.
- [121] A. V. Oppenheim and R. W. Schaffer, *Discrete-Time Signal Processing*. New Jersey: Prentice-Hall, 1989.